Advancements of the second harmonic generation techniques for the investigation of ultrafast photoinduced processes at liquid interfaces

Fedoseeva, Marina

UNIVERSITÉ DE GENÈVE FACULTÉ DES SCIENCES
Section de chimie et biochimie
Départment de chimie physique Professeur Eric Vauthey

Advancements of the Second Harmonic Generation Techniques for the Investigation of Ultrafast Photoinduced Processes at Liquid Interfaces

THÈSE

présentée à la Faculté des sciences de l'Université de Genève pour obtenir le grade de Docteur ès sciences, mention interdisciplinaire

par
Marina Fedoseeva
de
Moscou (Russie)

Thèse № 4619

GENÈVE
Atelier ReproMail
2013

UNIVERSITÉ
DE GENÈVE

FACULTÉ DES SCIENCES

Doctorat ès sciences
Mention interdisciplinaire

Thèse de *Madame Marina FEDOSEEVA*

intitulée :

" Advancements of the Second Harmonic Generation Techniques for the Investigation of Ultrafast Photoinduced Processes at Liquid Interfaces "

La Faculté des sciences, sur le préavis de Messieurs E. VAUTHEY, professeur ordinaire et directeur de thèse (Département de chimie physique), J.-P. WOLF, professeur ordinaire (Groupe de physique appliquée) et P.-F. BREVET, professeur (Laboratoire de Spectrométrie Ionique et Moléculaire, Université Claude Bernard Lyon 1, France), autorise l'impression de la présente thèse, sans exprimer d'opinion sur les propositions qui y sont énoncées.

Genève, le 2 décembre 2013

Thèse - 4619 -

Le Doyen, Jean-Marc TRISCONE

N.B. - La thèse doit porter la déclaration précédente et remplir les conditions énumérées dans les "Informations relatives aux thèses de doctorat à l'Université de Genève".

God made the bulk; the surface was invented by the devil

Wolfgang Pauli, Nobel Prize in Physics 1945

Remerciements

Cette thèse a été réalisée à l'Université de Genève, au département de Chimie Physique, sous la supervision du Prof. Eric Vauthey. Je le remercie de m'avoir donné la chance de travailler au sein de son groupe, pour sa supervision et son mentorat, ainsi que pour son temps et sa patience.

Je tiens à remercier les Prof. Jean-Pierre Wolf (Université de Genève) et Prof. Pierre-François Brevet (Université Claude Bernard Lyon 1) pour avoir accepté de s'engager comme experts lors de ma soutenance.

Je souhaiterais également remercier tous les doctorants et post-doctorants du groupe pour leur aide et leur attitude amicale durant le temps que j'ai passé à Genève. Je tiens particulièrement à remercier la secrétaire du Département de Chimie Physique, Sophie Jacquemet, ainsi que Didier Frauchiger, le technicien, pour leur aide constante et leur patience lors de nos discussions en français.

Un merci tout particulier aux anciens membres du groupe, Angela Punzi et Piotr Fita, qui m'ont grandement aidé lorsque j'ai débuté mon travail au sein du groupe.

Enfin et surtout, je voudrais remercier ma famille et mes amis, à Moscou et Genève, qui ont été d'un grand soutien durant ces années.

TABLE OF CONTENTS

1. INTRODUCTION

1.1. What are liquid interfaces, why and how to study them?

The interface between two immiscible liquids has attracted the interest of scientists for a long time. This region plays an important role in many phenomena that are crucial in areas as diverse as life sciences, environmental sciences, and technology.[1-3] Although a liquid interface can be viewed as a region segregating two bulk liquids, it does not prevent the transfer of mass and energy between them. Therefore, understanding the properties of interfaces and the dynamics of interfacial processes is of utmost importance not only for our fundamental knowledge but also for many applications such as the design of new drugs or developments toward renewable energies.[4]

One peculiarity of interfaces is that the molecules located in this region experience an anisotropy of forces. As a consequence, their orientation is not random as in bulk solution, and the dynamics of molecular processes that depends on environmental properties (e.g., friction or local electric field) can be expected to be different at interfaces and in bulk solutions. In bulk materials, these properties can be directly deduced from macroscopic quantities such as the viscosity and the dielectric constant. However, the interfacial region between two immiscible liquids is very thin, typically 1 nm;[5] therefore, the viscosity and the dielectric constant cannot be really defined. Consequently, friction and the local electric field at the interface have to be measured in situ using local probes.[6-9] One approach for gaining insight into interfacial properties is the so-called dynamic probe concept, where the dynamic probe is a molecule whose photophysics, for example, its excited-state lifetime depends on a property of the environment. This approach first requires a good understanding of the excited-state dynamics of the probe in bulk solution and the dependence of this dynamics on the solvent. Once this knowledge is available, the dynamics of the probe can be investigated at interfaces and compared to that in the bulk.

Liquid interfaces offer more degrees of freedom for fine-tuning a given environmental parameter than bulk solutions because the properties of both phases can be varied independently. This can be advantageously used to obtain specific information on a probe molecule, e.g. its photophysics, adsorbed at the interface.

Once the properties of liquid interfaces are well understood, this region can be used as a specific environment for performing chemical reactions that would not be possible in bulk media such as bimolecular reactions between reactants located in different phases. Photoinduced electron transfer through liquid interfaces is one example that has a key value for a number of chemical and biological phenomena.[4, 10]

1.2. State-of-the-art experimental methodology

Even though interfaces are of clear fundamental scientific importance, they are a challenge to study on the molecular level. Most of the powerful and common spectroscopic techniques used for investigating molecules in bulk media cannot be readily applied to interfaces because the signal from the sample is almost entirely due to the molecules located in the bulk phases, whose number surpasses that of the interfacial molecules by many orders of magnitude. The interfacial response is thus totally buried in that from the bulk.

While many established techniques exist for characterizing solid surfaces with atomic resolution, the situation is different for liquid interfaces. Primarily due to surface disorder, capillary waves, and volatility of liquid water, the knowledge about the detailed molecular structure of these interfaces has been primitive until recently.[11-14]

The progress in the experimental aspects of investigation of liquid interfaces emerged with the development of modern spectroscopic techniques employed in geometry that grants, to different extend, their surface selectivity. Up to date and to the best of our knowledge, studying liquid interfaces involve experimental solutions based on three conceptual approaches: (1) beam confinement; (2) energy confinement; (3) probing an interface-specific property.

In the first approach, the optical *beams are confined* close to the interface in order to reduce the relative contribution from the bulk phases to the signal.

One of the experiments based on this principle was realized by Deckert and co-workers,[15, 16] who used the light from a scanning near-field optical microscopy tip to perform Raman spectroscopy. By progressively moving the tip toward the interface, Raman spectra at different penetration depths relative to the interface could be measured. This technique was applied to study the water/carbon tetrachloride interface with a spatial resolution of 200 nm.[16] The OH stretching vibrational frequency of water was found to shift to higher frequencies when approaching the

interface. This was interpreted in terms of weaker hydrogen bonding in the vicinity of the nonpolar phase. However, no dynamic studies have been performed with this method.

Time-resolved total internal reflection fluorescence (TR-TIRF) is another method based on the beam-confining concept. It was first demonstrated at a sapphire/polymer interface by Masuhara et al.[17] and was later applied to liquid/liquid interfaces.[18-20] In TR-TIRF, the probe molecules are located in the phase with the lower refractive index, whereas the phase with the higher refractive index is transparent. The probe molecules are excited by the evanescent field generated upon total internal reflection of a laser pulse striking the interface from the high-refractive-index side. Because the evanescent field has a penetration depth of typically 100 nm, fluorescence arises only from molecules located close to the interface. Using time correlated single photon counting electronics for detection allows fluorescence dynamics measurements with a time resolution of 20−50 ps. This technique has been used successfully to investigate various excited-state processes (e.g., photoisomerization or excitation energy transfer)[19, 21] close to a liquid/liquid interface. The study of the reorientational dynamics of fluorophores near an interface is also easily accessible by measuring the decay of the fluorescence anisotropy.[18]

Although this method benefits from its simplicity, it is limited to the study of emissive probes. Thus, no information on the dynamics of dark species or on the mechanism of possible quenching processes can be gained from TR-TIRF measurements. Time-resolved attenuated TIR (TR-ATIR), which was demonstrated several years ago, is not impaired by this limitation.[22] However, this technique suffers from poor sensitivity because of the usually very weak photoinduced changes in absorbance experienced by the evanescent field.

Our group tried to combine the sensitivity of fluorescence and the polyvalence of transient absorption spectroscopy by applying the transient evanescent grating (TG) technique[23] first demonstrated at solid/solid and solid/liquid interfaces.[24, 25] The conventional TG method is based on a four-wave mixing process where two pump pulses crossed on the sample generate a spatial modulation of intensity that, upon absorption by the sample, results in spatial modulations of refractive index and absorbance (i.e., in phase and amplitude gratings).[26] Probing is achieved with a third, time-delayed pulse that strikes the gratings at the Bragg angle and undergoes partial diffraction. The intensity of the diffracted pulse, I_d, the signal, is given by

$$I_d = a\Delta n^2 + b\Delta A^2$$

where Δn and ΔA are the modulation amplitudes of the refractive index and absorbance, respectively, and a and b are constants. Therefore, the temporal changes in refractive index and absorbance at the probe wavelength can be monitored by measuring the signal intensity as a function of the time delay.[27] Broadband detection, allowing diffracted spectra over the whole visible range to be recorded, has also been demonstrated.[28] In the transient evanescent grating technique, some of the waves are evanescent fields generated upon TIR at the liquid/liquid interface. In the simplest configuration (**Figure 1.1 left**), the gratings are generated in the absorbing phase by two pump pulses and interfacial selectivity is achieved by probing in TIR geometry. Only the evanescent probe field interacts with the gratings and is diffracted. In this case, the interfacial selectivity, which depends on the penetration depth of the probe field, is the same as in TR-TIRF.

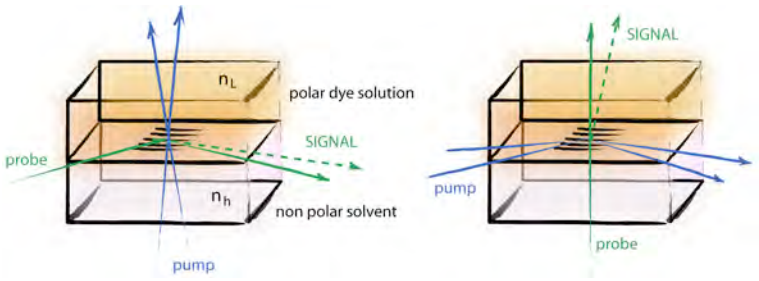

Figure 1.1. Two possible beam arrangements for the transient evanescent grating technique (n_L and n_h refer to low and high refractive indices, respectively).

A better selectivity can be achieved by generating true evanescent gratings, i.e. by using two pump pulses in TIR geometry (**Figure 1.1 right**). As the diffracted signal intensity is proportional to the square of the photoinduced changes, a gain in interfacial selectivity by a factor of 2 is realized. By measuring the time evolution of the refractive index changes, this technique has been used to investigate the thermo-acoustic properties (i.e., the speed of sound, the acoustic attenuation, and the thermal conductivity) of the region close to the interface.[29] Moreover, measurements of the changes in absorbance provide access to population dynamics:[23] for example, such experiment was done for a solution of rhodamine 6G (R6G) in methanol close to the interface with decalin and the obtained time profile of diffracted intensity was assigned to the recovery of the R6G ground-state population.

Another sensitive technique, based on the *energy confinement* approach and only recently employed for investigations of liquid surfaces, is X-ray photoelectron spectroscopy (PES). Being a well-developed tool for studying solid samples under ultrahigh vacuum, PES has remained rather challenging for aqueous solutions. A great advance in liquid PES has emerged with the development of the vacuum liquid microjet technique.[30-33]

In the simplest description, a PES experiment consists in the detection of the kinetic energy of primary (and secondary) electrons emitted from the sample upon irradiation by monochromatic photons and provides element-specific, local atomic/molecular environment information (**Figure 1.2**). From the energy distributions of the photoelectrons (chemical shift), details about the local electronic structure, and hence of the geometric structure of a given atomic/molecular species, within its distinct chemical environment can be inferred. Performing PES measurements with a tunable incident photon source, e.g. a synchrotron light source, provides additional benefits. By varying the incoming photon energy, the kinetic energy of the emitted photoelectrons can be varied, which in turn controls the surface sensitivity of the experiment according to the energy dependent inelastic mean free path (IMFP) of the electrons.

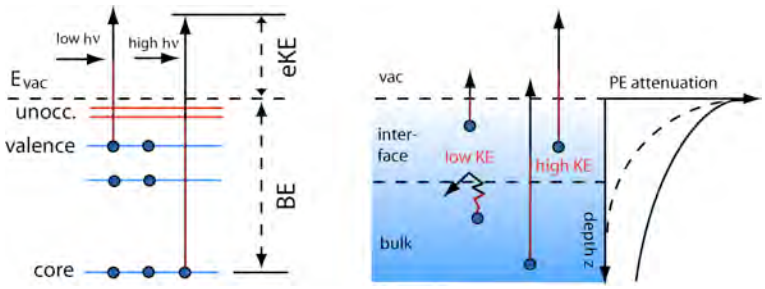

Figure 1.2. Left: Schematic energy level diagram for the electronic excitation and de-excitation processes, depicting unoccupied valence, and occupied valence and core-level states. **Right**: Depiction of electron escape from the solution at both low and high kinetic energy illustrating the effect of elastic and inelastic scattering. Qualitative representation of PE emission and exponentially decaying attenuation function vs. probing depths for short and large IMFP. For details see ref.[34]

Thanks to the fact that the IMFP of photoelectrons in water is less than 20 Å for electron energies near 80-100 eV (the best up-to-date estimates), this method can achieve high surface selectivity. These are the typical ranges in studies of the

composition and density distributions across the solution interface. In his recent perspective article,[34] Winter predicts a huge potential for liquid-jet PES not only for accessing the ground- and excited-state electronic structure of water systems, but also for studying ultrafast dynamics in aqueous solution (time-resolved multicolor PES with tunable sub-femtosecond soft X-ray pulses of free-electron laser source).

Despite of obvious advantages, both beam and energy confinement approaches are nevertheless not intrinsically interface-selective and cannot thus provide dynamical and structural information exclusively from the interfacial region. Indeed, in the case of beam confinement techniques the probed region is typically 50 to 100 nm thick, whereas the interfacial region has a thickness of the order of 1 nm. Although the confinement of the optical beam realized by TIR seems to be sufficient to enable the observation of molecules near an interface, it is still too large to achieve true interfacial selectivity. Therefore, discriminating the response from the molecules at the interface from that of molecules located further away can be highly problematic. In the case of the energy confinement approach, although PES has clearly matured to a standard technique for studying liquids near the water-vapor pressure, yet it suffers from probing interfacial depths with sufficient precision, even with fine-tuning of the incoming photon energy, making its surface selectivity uncertain.[35]

The solution to circumvent the drawbacks of presented above approaches is to *probe a property that is intrinsic to interfaces*, namely, one that vanishes in the bulk phases. This is the case for second and higher even orders of the optical nonlinear susceptibility, $\chi^{(2n)}$,[36] whereas $\chi^{(2n)}$-dependent second-order nonlinear processes such as second harmonic (SHG) and sum frequency generation (SFG) are electric-dipole-forbidden in centrosymmetric media. However, the interface between two isotropic media such as two liquids is not centrosymmetric and thus possesses a nonzero $\chi^{(2n)}$. This is the principle behind the surface SHG (SSHG) technique,[37, 38] where an optical field, $\vec{E}$, at frequency ω_1 strikes the interface and creates a second-order nonlinear polarization oscillating at $\omega_2 = 2\omega_1$:

$$\vec{P}^{(2)}(\omega_2) = \varepsilon_0 \vec{\chi}^{(2)}(\omega_2, \omega_1, \omega_1)\vec{E}(\omega_1)\vec{E}(\omega_1) \qquad (1.1)$$

where $\vec{\chi}^{(2)}$ is the second-order nonlinear optical susceptibility tensor. Neglecting local field effects, this macroscopic quantity can be related to the second-order polarizability tensor, $\vec{\alpha}^{(2)}$, of the molecules that constitute the interface:

$$\varepsilon_0 \vec{\chi}^{(2)} = N < \alpha^{(2)} > \qquad (1.2)$$

where N is the interfacial adsorbate density (number per unit area), with the brackets indicating an average over the molecular orientations.

The detailed theoretical aspects of SSHG will be given in the next chapter. Here it will be only noted that an important feature of $\chi^{(2)}$ lies in its wavelength dependence, so that it increases significantly when the incoming and/or signal fields are in resonance with a transition of the material (**Figure 1.3**).[39]

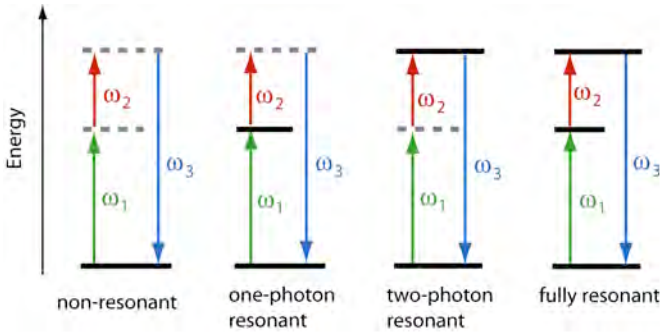

Figure 1.3. Energy level scheme illustrating the possible resonances in SSH(F)G. Solid horizontal lines represent stationary states and dotted lines represent virtual states.

Consequently, the SH intensity spectrum reflects one- and two-photon resonances of molecules located at the interfaces.[37] By taking advantage of the electronic resonance enhancement, the SH signal from relatively dilute (~10^{-5} M) probe molecules can surpass the nonresonant contribution from the solvent molecules by several orders of magnitude. The same principles underlie surface SFG (SSFG), where one of the incident fields is at fixed frequency and the other is tunable or has a broad spectrum.[40] In most SSFG applications to liquid interfaces, the second incident field is in the IR region and the signal intensity reflects vibrational resonances.[41] To be detectable, a vibrational mode has to be both IR- and Raman-active, precluding the investigation of centrosymmetric molecules, in agreement with their lack of second-order nonlinear susceptibility. It should nevertheless be noted that SSH(F)G from apparently centrosymmetric molecules cannot be excluded if these molecules are distorted at the interface.[42] As vibrational transitions generally have much smaller oscillator strengths

than electronic transitions, the corresponding resonance enhancement of the signal is smaller. As a consequence, vibrational SSFG is less sensitive than electronic SSFG and SSHG and needs much more concentrated samples. For example, vibrational SSFG has been intensively used to record the vibrational spectrum of water at liquid/water and air/water interfaces.[43-47] However, electronic SSFG has recently been demonstrated to be a very powerful method of recording the electronic spectrum of probe molecules at the air/water interface using a white light continuum as one of the incoming fields and broadband detection.[40, 48]

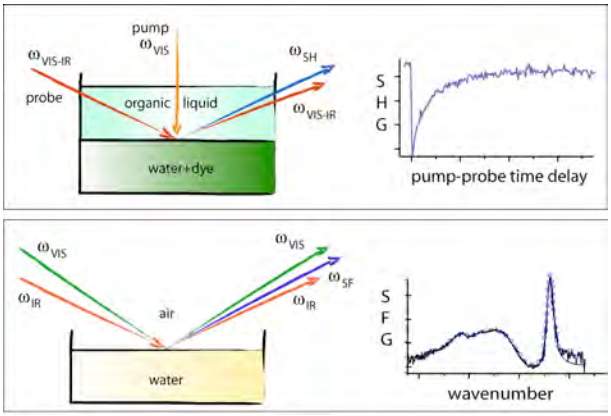

Figure 1.4. Experimental geometries of TR-SSHG (top) and steady state SSFG (bottom), and their typical detected signals. Usually SHG is employed in the VIS-IR range to probe the surface UV-VIS spectrum or the excited-state dynamics upon VIS-IR excitation, while SFG with a visible and IR photon probes the surface vibrational spectrum.

As a consequence of its higher sensitivity, electronic SSH(F)G can be relatively easily time resolved.[49-51] In this case, the molecules located in one of the phases are excited by a pump pulse and the variation of the SH(F) signal is recorded as a function of the time after excitation (**Figure 1.4**). Such experimental geometry ensures the interfacial selectivity of time-resolved (TR)-SSH(F)G.

This thesis is focused on demonstrating advancements and potentials of the TR-SSHG applied to the characterization of ultrafast photoinduced processes at liquid interfaces. In particular, it presents the work up to date, which has been conducted along three different strands: (1) Excited-state dynamics and spectroscopic signatures of interfacial molecular probes; (2) Characterization of environmental properties in interfacial systems; (3) Photoinduced electron transfer at liquid/liquid interface.

2. THEORY

2.1. General introduction to SHG processes

The discovery of the SHG in a quartz crystal by Franken et al.,[52] shortly after the demonstration of the first working laser by Maiman in 1960, signified the beginning of the field of nonlinear optics. In general, nonlinear optics studies phenomena that occur as a consequence of the modification of the optical properties of a medium by the presence of laser light that is sufficiently intense to provoke such modification. Nonlinear optical phenomena are called *nonlinear* because the response of a medium to an applied optical field *nonlinearly* depends on the strength of this optical field. For instance, SHG occurs as a result of the part of the atomic response that scales quadratically with the strength of the applied optical field: in this case, the interaction between the laser field at frequency ω and a nonlinear medium results in generation of a photon at frequency 2ω, and the intensity of the generated SH light increases as the square of the intensity of the applied field.

Shorty after the first SHG experiment in a quartz crystal, SHG was also observed from the centrosymmetric crystal of calcite.[53] Other bulk media, such as metals and liquids, were also used in SHG experiments.[54, 55] In parallel to the experimental investigations, several theoretical models were developed for a thin slab of nonlinear media[56] and for a boundary between two centrosymmetric media.[57] Those models assumed that a quadrupole term in the nonlinear polarization resulting from the discontinuity in the electric fields at the interface was the actual source of SHG radiation. However, the SHG experiments on silver surfaces revealed an additional surface dipole term contributing to the nonlinear polarization.[58] Finally, the surface sensitivity of SHG was primarily assigned to the symmetry-breaking nature of the surface rather than to the quadrupole effects.[59] As the basic groundwork on SHG had been laid out in the early 1980s,[60-63] it became a powerful technique for interfacial studies, mainly due to its exceptional sensitivity and selectivity to an interface. In the works up to date, SHG has been successfully applied to all kinds of interfaces: many general overviews[64-67] and comprehensive reviews of applications[68-76] can be found in the literature.

The basic interpretation of SHG lies in the dependence of the dipole moment per unit volume, or polarization $\vec{P}$, of a medium on the strength $\vec{E}_\omega$ of an applied laser field.

In the case of conventional optics, the induced polarization depends linearly on the electric field strength, whereas in nonlinear optics higher order polarization terms are also induced. Among these higher order terms, the second-order polarization $\vec{P}^{(2)}$ becomes the radiating source of light at frequency *2ω* and can be expressed as[60-63]

$$\vec{P}^{(2)} = \varepsilon_0 \chi^{(2)} : \vec{E}_\omega \vec{E}_\omega \tag{2.1a}$$

where $\chi^{(2)}$ is the second order nonlinear susceptibility of the medium. When the description of $\chi^{(2)}$ is generalized for application to three-dimensional systems, it becomes a third-rank tensor, so that

$$\vec{P}_i^{(2)} = \varepsilon_0 \sum_{j,k} \chi_{ijk}^{(2)} : \vec{E}_\omega^j \vec{E}_\omega^k \tag{2.1b}$$

where *i, j, k* are the normal coordinates of laboratory system, respectively.

SHG is a surface specific technique as the second-order nonlinear susceptibility of centrosymmetric media is zero. It could be shown as follows: for a medium possessing inversion symmetry, the reversion of the propagation direction of the electromagnetic wave will not change the sign or magnitude of $\chi^{(2)}$ (because the medium itself remains unchanged) whereas both the electric field $\vec{E}_\omega$ and the second-order polarization $\vec{P}^{(2)}$ will change sign. Therefore the Eq. 2.1 becomes

$$-\vec{P}^{(2)} = \varepsilon_0 \chi^{(2)} : (-\vec{E}_\omega)(-\vec{E}_\omega) \tag{2.2}$$

Combining Eq. 2.2 with Eq. 2.1, we get $\vec{P}^{(2)} = -\vec{P}^{(2)}$, therefore, $\vec{P}^{(2)} = 0$. Thus, $\chi^{(2)}$ must be zero implying that no SHG is allowed in a centrosymmetric medium. This is, however, not the case at an interface, where inversion symmetry is no longer conserved: upon applying an inversion operation, $\vec{P}^{(2)}$ is not necessarily equal to $-\vec{P}^{(2)}$ and $\chi^{(2)}$ at interface is not necessarily zero and, thus, SHG from interfaces is allowed.

Heinz et al. have shown that in the isotropic and centrosymmetric medium the nonlinear susceptibility tensor $\chi^{(2)}$ is an odd function of a wave vector $\vec{k}$:[77]

$$\chi^{(2)}(k) = -\chi^{(2)}(-k) \tag{2.3}$$

It means that, in terms of a multipole expansion, the electric-dipole contributions, which are independent of *k*, are zero under inversion symmetry, as well as the alternate higher-order terms. Since SHG is electric-dipole forbidden in centrosymmetric media, the surface dipole appears to be the dominating contribution into the SH signal, which makes the SHG technique possess an intrinsic surface selectivity.

The second-order nonlinear susceptibility $\chi^{(2)}$ represents the macroscopic response of the medium to the applied field and can be related to the molecular energy levels: it displays a resonant enhancement when either the fundamental or the SH frequency coincides with that of a transition from the ground state of the molecule to an excited state.[36,37] For a classical anharmonic oscillator, one can express $\chi^{(2)}$ in the following form[76]

$$\chi^{(2)}(2\omega,\omega,\omega) \propto \frac{1}{(\omega_{ba}^2 - 4\omega^2 - 4i\Gamma_{ba}\omega)(\omega_{ba}^2 - \omega^2 - 2i\Gamma_{ba}\omega)^2} \tag{2.4}$$

where ω_{ba} is the resonance frequency of the $|a\rangle$ to $|b\rangle$ transition and Γ_{ba} is the line width associated with the transition. As can be seen from Eq. 2.4, the magnitude of $\chi^{(2)}$ is greatly enhanced by resonance effects when the fundamental, ω, or the SH frequency, 2ω, coincides with that of a molecular transition, ω_{ba}. Therefore, by selecting a proper fundamental frequency, one can probe a spectroscopic signature associated with a particular surface species.

Due to its surface and spectroscopic selectivity, SHG appears to be an exceptionally powerful technique for studying interfaces. In the presence of intense laser fields, e.g. ultrashort laser pulses, it can be applied to any interface: for instance, it can be employed for investigating interfacial molecular reactions and relaxation dynamics with ultrafast time resolution.[64-76, 78]

2.2. Theoretical aspects of SHG in reflective geometry

As has been mentioned, $\chi^{(2)}$ is a macroscopic nonlinear property, which is determined by the chemical composition of the interface. In order to relate the macroscopic quantity $\chi^{(2)}$ to the molecules that make up the interface, one has to relate $\chi^{(2)}$ to the nonlinear polarization $\vec{P}^{(2)}$ and the microscopic hyperpolarizability $\alpha^{(2)}$ of the molecules at interface, which is a sum over a product of transition matrix elements between the electronic and vibrational states of the molecule. The sections below cover the basic theoretical aspects of the relation between the radiation of a nonlinear polarization sheet and SSHG, the symmetric property of $\chi^{(2)}$ at an interface, the local field corrections, the transformation from $\alpha^{(2)}$ in the molecular coordinates system into $\chi^{(2)}$ with the experimental laboratory coordinates and, finally, presents the potential of the SSHG experiment for applications.

2.2.1 Radiation from a sheet of nonlinear polarization

A typical experimental geometry of SSHG at an interface is displayed in **Figure 2.1**. The incoming electric field $\vec{E}_{\omega}$ at frequency ω from the centrosymmetric bulk medium 1, characterized by the dielectric constant ε_1, induces a nonlinear polarization $\vec{P}^{(2)}$ at frequency 2ω at the interface. This nonlinear source of polarization $\vec{P}^{(2)}$ generates a reflected SH field at frequency 2ω, $\vec{E}_{2\omega}$, and a transmitted electric field into the centrosymmetric bulk medium 2, characterized by the dielectric constant ε_2. The transmitted electric field will not be discussed here.

In the original framework of the SHG experiment, Bloembergen et al.[56] proposed the solution for the problem of a slab of nonlinear medium embedded in linear dielectric medium. However, in most of interfacial systems, the passage from one centrosymmetric bulk medium to another across the boundary (the interface) takes place within a distance of a few molecular layers, which is negligibly small compare to the wavelength of laser light. Therefore, instead of the slab of definite thickness, the interface could be described as a sheet of nonlinear polarization with a dielectric constant ε' embedded as a boundary between two dielectric media as shown in **Figure 2.1**. Mathematically, a Dirac delta-function $\delta(z)$ could be used to assign the polarization sheet to a definite plane position.

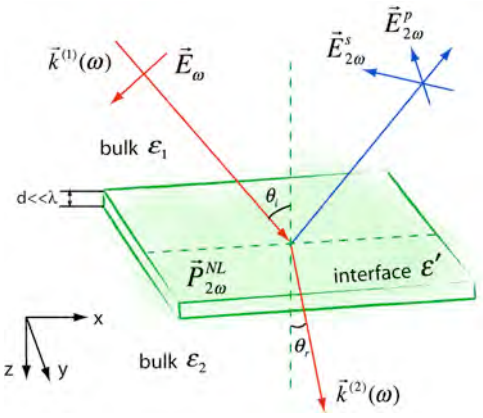

Figure 2.1. Typical experimental geometry for SHG at an interface. The incident electric field $\vec{E}_{\omega}$ induces a nonlinear polarization $\vec{P}^{(2)}$ at *2ω*, which in turn generates radiation $\vec{E}_{\omega}$ at *2ω* with s- and p- component, in both reflected and transmitted directions.

A thorough description of the problem of generation of waves in a nonlinear medium by a sheet of polarization can be found, for instance, in the book of Brevet.[38] In a very generalized form, the first nonlinear polarization in a multipole series expansion is presented as:[38]

$$\vec{\Pi}^{(2)}(\vec{r},t) = \vec{P}^{(2)}(\vec{r},t) - \vec{\nabla}\cdot\vec{Q}^{(2)}(\vec{r},t) + \frac{\mu_0}{i\omega}\vec{\nabla}\times\vec{M}^{(2)}(\vec{r},t) + \ldots \qquad (2.5)$$

where the second and third terms are responsible for the quadrupole and magnetic field contributions, respectively. In the electric dipole approximation and in the absence of magnetic field effect (i.e. assuming that the electrons and nuclei are in fixed positions), these terms vanish, so that $\vec{\Pi}^{(2)}(\vec{r},t) = \vec{P}^{(2)}(\vec{r},t)$. This simplified case will be further treated here.

The sheet of nonlinear polarization could be represented as:

$$\vec{P}^{(2)}(\vec{r},t) = P^{(2)}(\vec{r},t)\delta(z)\exp(i\vec{k}_s\cdot\vec{r} - i\omega_s t) \qquad (2.6)$$

where $\vec{k}_s$ is the wave vector defined as $\left|\vec{k}\right| = n'\omega_s / c$ and $n' \sim \sqrt{\varepsilon'}$. The subscript *s* is used to assign the surface specificity to the parameters.

The Maxwell's equations describing the radiation field generated by the surface nonlinear polarization of the sheet are given by[36, 61]

$$\nabla \times (\nabla \times \vec{E}) + \frac{\varepsilon}{c^2}\frac{\partial^2 \vec{E}}{\partial^2 t} = -\frac{4\pi}{c^2}\frac{\partial^2 \vec{P}^{(2)}}{\partial^2 t} \tag{2.7}$$

$$\vec{\nabla} \cdot \vec{D} = \vec{\nabla} \cdot (\varepsilon \vec{E} + \vec{P}^{(2)}) = 0 \Rightarrow \quad \vec{\nabla} \cdot (\varepsilon \vec{E}) = -4\pi \vec{\nabla} \cdot \vec{P}^{(2)} \tag{2.8}$$

Here $\vec{D}$ is the electric displacement field that appears in Maxwell's equations.
For the radiated fields within the surface region the following boundary conditions must be applied:[61]

$$\int_{0^-}^{0^+} \vec{E}(x,y)\,dz = 0 \Rightarrow \begin{cases} \Delta E_x = -\dfrac{4\pi}{\varepsilon'}\dfrac{\partial P_z}{\partial x} \\ \Delta E_y = -\dfrac{4\pi}{\varepsilon'}\dfrac{\partial P_z}{\partial y} \\ \Delta E_z = 0 \Rightarrow \Delta D_z = -4\pi\left(\dfrac{\partial P_x}{\partial x} + \dfrac{\partial P_y}{\partial y}\right) \end{cases} \tag{2.9}$$

$$\int_{0^-}^{0^+} \vec{B}(x,y)\,dz = 0 \Rightarrow \begin{cases} \Delta B_x = -4\pi i \dfrac{\omega_s}{c} P_y \\ \Delta B_y = +4\pi i \dfrac{\omega_s}{c} P_x \\ \Delta B_z = 0 \end{cases} \tag{2.10}$$

This implies that $\vec{E}$ and $\vec{B}$ must remain finite when the layer is compressed ($\vec{B}$ is the magnetic field that also appears in Maxwell's equations). Here ΔB_x represents the difference of B_x across the interface, which is:

$$\Delta B_x = B_x(z = 0^+) - B_x(z = 0^-) \tag{2.11}$$

and similarly for the other boundary conditions in Eq. 2.9 – 2.10.
Solutions for Maxwell's equations (Eq. 2.7 – 2.8) with the boundary conditions (Eq. 2.9 – 2.10) give the p- (in-plane) and s-polarized (out-of-plane) components of the SH

electric field radiated back into centrosymmetric bulk medium 1, $E_{2\omega}^{p}$ and $E_{2\omega}^{s}$ (**Figure 2.2**) respectively,[61]

$$E_{2\omega}^{p} = i4\pi k^{(1)} \frac{k_z^{(2)} \vec{P}_x^{(2)} + (\varepsilon_2 / \varepsilon') k_x \vec{P}_z^{(2)}}{\varepsilon_2 k_z^{(1)} + \varepsilon_1 k_z^{(2)}} \tag{2.12}$$

$$E_{2\omega}^{s} = i4\pi k^{(1)} \frac{(1/\varepsilon_1) k^{(1)} \vec{P}_y^{(2)}}{k_z^{(1)} + k_z^{(2)}} \tag{2.13}$$

where $k^{(1)}$ and $k^{(2)}$ are the wave vectors of the radiation at 2ω in centrosymmetric bulk media 1 and 2; the subscripts *x*, *y*, *z* stand for x-, y-, and z-components in the laboratory coordinate system, with $k_z^{(1)} = k^{(1)} \cos\theta_i$, $k_z^{(2)} = k^{(2)} \cos\theta_r$ and $k_x^{(2)} = k^{(2)} \sin\theta_r$; θ_i is the incident angle and θ_r – the refractive angle that could be deduced from the Snell's law; $\vec{P}_x^{(2)}$, $\vec{P}_y^{(2)}$ and $\vec{P}_z^{(2)}$ are the components of $\vec{P}^{(2)}$.

Eq. 2.12 – 2.13 imply that the complete knowledge of SH electric field radiated back into centrosymmetric bulk medium 1, i.e. $E_{2\omega}^{p}$ and $E_{2\omega}^{s}$, depends on the complete knowledge of the $\vec{P}_x^{(2)}$, $\vec{P}_y^{(2)}$ and $\vec{P}_z^{(2)}$.

The nonlinear polarization, $\vec{P}^{(2)}$, can be expressed in terms of the electric field amplitudes $\vec{E}'_{\omega}$ in the interfacial layer, which is related to the incoming electric field $\vec{E}_{\omega}$ via Fresnel coefficients,[38] as follows:

$$\vec{P}^{(2)} = \varepsilon_0 \chi^{(2)} : \vec{E}'_{\omega} \vec{E}'_{\omega} \tag{2.14}$$

Since $\chi^{(2)}$, is a third-rank tensor with 3 x 3 x 3 = 27 elements, the components of $\vec{P}^{(2)}$, i.e., $\vec{P}_x^{(2)}$, $\vec{P}_y^{(2)}$ and $\vec{P}_z^{(2)}$, could be described through the tensor elements, $\chi_{ijk}^{(2)}$, as:

$$\vec{P}_i^{(2)} = \varepsilon_0 \sum_{j,k} \chi_{ijk}^{(2)} \vec{E}'_j(\omega) \vec{E}'_k(\omega) \tag{2.15}$$

Therefore, in order to obtain the nonlinear polarization components $\vec{P}_x^{(2)}$, $\vec{P}_y^{(2)}$ and $\vec{P}_z^{(2)}$, one has to relate the tensor elements $\chi_{ijk}^{(2)}$ and the components of the electric field amplitudes in the interfacial layer $\vec{E}'_\omega$ to the incoming electric fields.

2.2.2. Second-order nonlinear susceptibility tensor elements

When symmetry operations are applied to $\chi^{(2)}$, most of the 27 symmetry elements of $\chi^{(2)}$ will vanish.[79, 80] For an isotropic interface, as shown above, even if the inversion symmetry is broken along *z*-axis, other symmetries are still preserved. For the SHG, there are only 7 non-vanishing tensor elements:

$$\chi_{zzz}^{(2)} \tag{2.16a}$$

$$\chi_{zxx}^{(2)} = \chi_{zyy}^{(2)} \tag{2.16b}$$

$$\chi_{xzx}^{(2)} = \chi_{yzy}^{(2)} \tag{2.16c}$$

$$\chi_{xxz}^{(2)} = \chi_{yyz}^{(2)} \tag{2.16d}$$

As the incoming electric fields in Eq. 2.14 are identical, it can be assumed that $\chi_{ijk}^{(2)} = \chi_{ikj}^{(2)}$. Additionally, *x* and *y* are identical at an isotropic surface, so that one obtains:

$$\chi_{xzx}^{(2)} = \chi_{yzy}^{(2)} = \chi_{xxz}^{(2)} = \chi_{yyz}^{(2)} \tag{2.16e}$$

i.e. only 3 tensor elements are actually independent.

Consequently, the expressions for $\vec{P}_x^{(2)}$, $\vec{P}_y^{(2)}$ and $\vec{P}_z^{(2)}$ could be reduced to:

$$P_x^{(2)} = 2\chi_{xzx}^{(2)} E'_z(\omega) E'_x(\omega) \tag{2.17a}$$

$$P_y^{(2)} = 2\chi_{yzy}^{(2)} E'_z(\omega) E'_y(\omega) \tag{2.17b}$$

$$P_z^{(2)} = \chi_{zzz}^{(2)} E'_z(\omega)^2 + \chi_{zxx}^{(2)} (E'_x(\omega)^2 + E'_y(\omega)^2) \tag{2.17c}$$

Before obtaining an expression, which bridges the macroscopic nonlinear susceptibility $\chi^{(2)}$ with the microscopic nonlinear polarizability $\alpha^{(2)}$, the relations between the electric field amplitudes in the interfacial layer $\vec{E}'_{\omega}$ and the incoming optical fields $\vec{E}_{\omega}$ have to be established.

2.2.3. Electric field amplitudes in the interfacial layer

As has been mentioned, the electric field amplitudes in the interfacial layer, $E'_x(\omega)$, $E'_y(\omega)$ and $E'_z(\omega)$ are different from the incoming optical fields $\vec{E}_{\omega}$ and can be related to each other through the Fresnel transmission coefficients, T_s and T_p, and the proper continuity conditions.[79]

As shown in **Figure 2.1**, the incoming electric field $\vec{E}_{\omega}$ from medium 1 arrives at the interface at an angle of θ_i and gets refracted at an angle of θ_r. The incoming light field has s- and p-polarized electric field components denoted E^s_{ω} and E^p_{ω}, respectively.

The Fresnel transmission coefficients, T_s and T_p, are given by[81]

$$T_s = \frac{2\cos\theta_i \sin\theta_r}{\sin(\theta_i + \theta_r)} \tag{2.18a}$$

$$T_p = \frac{2\cos\theta_i \sin\theta_r}{\sin(\theta_i + \theta_r)\cos(\theta_i - \theta_r)} \tag{2.18b}$$

The electric field components between the interface and medium 2 that are parallel ($E_{x,y}$) and perpendicular (E_z) to the interface give the electric field components in the interfacial layer with the following boundary conditions:

$$E_{2x}(\omega) = E'_x(\omega) \tag{2.19a}$$

$$E_{2y}(\omega) = E'_y(\omega) \tag{2.19b}$$

$$E_{2z}(\omega) = -\frac{\varepsilon'}{\varepsilon_2} E'_z(\omega) \tag{2.19c}$$

Finally, one obtains the relationship between the electric field amplitudes in the interfacial layer and the incoming optical fields:

$$E'_x(\omega) = T_p E^p_\omega \cos\theta_r \quad (2.20a)$$

$$E'_y(\omega) = T_s E^s_\omega \quad (2.20b)$$

$$E'_z(\omega) = -\frac{\varepsilon_2}{\varepsilon'} T_p E^p_\omega \sin\theta_r \quad (2.20c)$$

Substituting the Eq. 2.20 in Eq. 2.17 and then in Eq. 2.12 – Eq. 2.13, one obtains the final relation between the SH field components ($E^p_{2\omega}$ and $E^s_{2\omega}$) and the input field components (E^p_ω and E^s_ω).

Experimentally, by selecting the incoming field components and the s- and p-SH components, one could yield the macroscopic nonlinear susceptibility $\chi^{(2)}$ of the interfacial system. In order to obtain the information on the interfacial species, one has to relate the elements of $\chi^{(2)}$ to the elements of the microscopic nonlinear polarizability $\alpha^{(2)}$.

2.2.4. Transformation of macroscopic susceptibilities into microscopic polarizabilities

In the absence of local field effect caused by the dipole-dipole interaction (discussed in the next section), the macroscopic susceptibility elements $\chi^{(2)}_{ijk}$ can be presented as the sum of the individual molecular polarizabilities $\alpha^{(2)}_{i'j'k'}$ via statistical averaging over molecular orientations:

$$\varepsilon_0 \chi^{(2)} = N_s < \alpha^{(2)} > \quad (2.21)$$

where N_s is the number of molecules adsorbed at the interface and the brackets indicate the orientational averaging. Such averaging can be in general employed for coherent radiation processes (e.g. SHG at an interface), wherein individual coherently oscillating dipoles act as a collective oscillating dipole.

The individual components of $\chi^{(2)}$ tensor could be deduced from the transformation between the laboratory coordinates (x, y, z) and the coordinates associated with a molecule (x', y', z'). Such transformation involves Euler angles, θ, ϕ and ψ, where $\theta \in (0, \pi)$ is the angle between z and z', $\phi \in (0, 2\pi)$ is the azimuthal angle about z axis of the laboratory coordinate system, and $\psi \in (0, 2\pi)$ is the azimuthal angle about z' axis of the molecular coordinate system (**Figure 2.2**).[68]

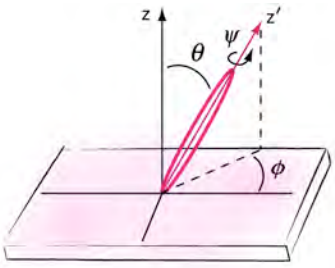

Figure 2.2. Definition of angles θ, ϕ and ψ between the laboratory coordinate system and the molecular coordinate system. Pink oval represents a molecule with the dipole moment aligned along z'.

A relationship between $\chi^{(2)}_{ijk}$ and $\alpha^{(2)}_{i'j'k'}$ could be written as:

$$\varepsilon_0 \chi^{(2)}_{ijk} = N_s \sum_{i'j'k'} < T_{ii'} T_{jj'} T_{kk'} > \alpha^{(2)}_{i'j'k'} \qquad (2.22)$$

where $T_{ii'} T_{jj'} T_{kk'}$ is the product of the possible combinations of the elements of the transformation matrix T, which relates the laboratory coordinates to the molecular coordinates with Euler angles, θ, ϕ and ψ, and < > denotes the orientational averaging. Papers by Corn[68] and Mazely[82] offer a complete description of the coordinate transformation from the molecular coordinate system to that of the surface. Here only the final result for a uniaxial molecule, i.e. with a well-defined molecular axis z', with its nonlinear polarizability tensor $\alpha^{(2)}$, respectively dominated by $\alpha^{(2)}_{z'z'z'}$ component, will be presented.

The 3 independent non-zero elements of $\chi^{(2)}$ ($\chi^{(2)}_{zzz}$, $\chi^{(2)}_{zxx} = \chi^{(2)}_{zyy}$, $\chi^{(2)}_{xzx} = \chi^{(2)}_{yzy} = \chi^{(2)}_{xxz} = \chi^{(2)}_{yyz}$) are expressed as follows:

$$\varepsilon_0 \chi^{(2)}_{zxx} = \frac{1}{2} N_s \alpha^{(2)}_{z'z'z'} (< \cos\theta > - < \cos^3\theta >) \qquad (2.23a)$$

$$\varepsilon_0 \chi^{(2)}_{xzx} = \frac{1}{2} N_s \alpha^{(2)}_{z'z'z'} (<\cos\theta> - <\cos^3\theta>) \quad (2.23b)$$

$$\varepsilon_0 \chi^{(2)}_{zzz} = N_s \alpha^{(2)}_{z'z'z'} <\cos^3\theta> \quad (2.23c)$$

In general, if the energetic transition of a molecule at the interface is in resonance with the incoming fundamental or outgoing SH light, one can assume that this molecule uniaxial along the transition axis.

For molecules, that are not uniaxial, the expressions for $\chi^{(2)}$ tensor elements can be deduced in a similar manner taking into account other possible non-zero elements of the molecular nonlinear polarizability $\alpha^{(2)}$ from the molecular symmetry.[79]

2.2.5. Local field correction for the nonlinear susceptibility

The expressions for the $\chi^{(2)}$ tensor presented so far are strictly correct only for dilute media: it has been assumed that $\varepsilon_0 \chi^{(2)} = N_s <\alpha^{(2)}>$, where N is the number of atoms or molecules per unit volume, and the atoms or molecules are far enough from each other not to experience any dipole-dipole interaction.

However, in the condensed matter, where the dipole-dipole interaction is no longer negligible, $\chi^{(2)}$ is actually not proportional to $\alpha^{(2)}$. Hence, the macroscopic electric field and the effective electric field that each atom or molecule experiences can be different. The complete derivation of local field corrections could be found, for instance, in the books of Shen[83] and Boyd.[36] The final relationship between the macroscopic nonlinear susceptibility and the molecular polarizability can be presented as follows:[36]

$$\varepsilon_0 \chi^{(2)} = L^{(2)}_{(2\omega;\omega;\omega)} N_s <\alpha^{(2)}> \quad (2.24)$$

Here $L^{(2)}_{(2\omega;\omega;\omega)}$ is the local field correction factor for the second-order susceptibility derived within the Lorentz model, which assumes the proportionality of the field induced by the neighboring dipoles and the polarization:[83]

$$L^{(2)}_{(2\omega;\omega;\omega)} = [\frac{\varepsilon^{(1)}_{2\omega} + 2}{3}][\frac{\varepsilon^{(1)}_{\omega} + 2}{3}][\frac{\varepsilon^{(1)}_{\omega} + 2}{3}] \quad (2.25)$$

where $\varepsilon_{\omega}^{(1)}$ is the linear dielectric constant: $\varepsilon_{\omega}^{(1)} = 1 + 4\pi\chi^{(1)}$. It was shown that local field effects are negligible up to the monolayer concentration for benzene derivatives, such as phenol and cresol molecules adsorbed at the air/water interface.[84] Therefore, it is safe to extend this conclusion onto similar molecules and long-chain molecules and neglect the local field effects hereafter.

2.2.6 Applications of the SHG experiment

As has been shown above, at the core of the SHG experiment lies an opportunity to measure the nonlinear response of an interfacial system, i.e. its macroscopic nonlinear second-order susceptibility $\chi^{(2)}$. Eq. 2.21 shows that $\chi^{(2)}$ is directly proportional to the number of surface molecules N_s and the microscopic nonlinear second-order polarizability $<\alpha^{(2)}>$ (averaged over molecular orientations).

The proportionality to N_s yields information on the adsorption and chemical reaction equilibrium at the interface. By monitoring the time dependence of the population of interfacial species, the information on the interfacial excited-state dynamics can also be obtained.[68, 74, 76]

The proportionality to $<\alpha^{(2)}>$ directly relates the measured SH field to the orientation of the radiating dipoles of the interfacial molecules. For instance, Eq. 2.12 – 2.13 show that $E_{2\omega}^{p}$ is related to $\vec{P}_x^{(2)}$ and $\vec{P}_z^{(2)}$, and $E_{2\omega}^{s}$ is related to $\vec{P}_y^{(2)}$. By substituting the expressions for $\vec{P}_x^{(2)}$, $\vec{P}_y^{(2)}$ and $\vec{P}_z^{(2)}$, one obtains:

$$\frac{E_{2\omega}^{p}}{E_{2\omega}^{s}} = a\xi + b \qquad \text{where} \quad \xi = \frac{<\cos^3\theta>}{<\cos\theta\sin^2\theta>} \qquad (2.26)$$

where a and b are constants including the calculations for the electric fields in the interfacial layer (Eq. 2.20), the geometrical parameters θ_i and θ_r, the dielectric constants ε_1, ε_2 and ε', and the polarization of the incoming light. One could calculate a and b for a given experimental geometry. Detecting SH signal in different polarization configurations, one obtains $\frac{E_{2\omega}^{p}}{E_{2\omega}^{s}}$, from which the value of ξ

can be deduced. Assuming that the molecular orientation is distributed within a certain angle with a δ-function distribution, one can obtain the average molecular orientation angle θ with respect to the normal of an interfacial plane.[68]

One important advantage of SHG is that the phase measurement of the SH signal (so-called heterodyne detection) gives the absolute orientation of molecules at the interface: dipoles pointing up or down.[85, 86] Most of the SHG measurements provide data representing not $\chi^{(2)}$ itself but actually $\left|\chi^{(2)}\right|^2$ due to the homodyne nature of signal detection. However, as could be understood from Eq. 2.23, the orientation average part of all the $\chi^{(2)}$ elements is an odd function of $\cos\theta$, which means that $\chi^{(2)}$ changes sign depending on whether $\langle\cos\theta\rangle > 0$ or $\langle\cos\theta\rangle < 0$. Therefore, by measuring the phase of $\chi^{(2)}$ experimentally, the absolute orientation of a molecule, i.e. pointing up or pointing down, can be obtained. Importantly, this information cannot be obtained from linear spectroscopy or third-order nonlinear techniques, because the orientation average part of linear and third order susceptibilities is an even function of $\cos\theta$.

Finally, the SHG spectroscopy can achieve high spatial, spectral, and temporal resolution. As the SHG process is a result of an instantaneous response of an interfacial system to the incoming electric field, the application of ultrashort pulses makes it an exceptional tool to probe molecular reaction and relaxation dynamics at interfaces with pico- and femtosecond time resolution.[38, 72-76, 78]

3. EXPERIMENTAL

Over the last decades, both steady state and time-resolved SHG spectroscopies have been widely used for the study of liquid/liquid, gas/liquid and solid/liquid interfaces. In particular, they were applied to studying such physical and chemical phenomena at interfaces as molecular orientational motion,[87] isomerization,[51] solvation dynamics,[87-89] surface protonation,[90] ion adsorption,[91-93] energy and charge transfer.[94-96] Despite these numerous investigations, the straightforward access to the interfacial information on the molecular level remains rather scarce. There are several reasons for this. One of them is that the experimental tools used up to now are still relatively primitive compared to the level of sophistication of the spectroscopic techniques applied for studying photoinduced processes in bulk solution. Indeed, all of the experimental studies presented so far on air/liquid and liquid/liquid interfaces make use of very similar setups.[97] Although some setups allow tuning the probe wavelength, giving more flexibility in the choice of molecules, probing is in most cases only done at a single observation wavelength. This makes the interpretation of the experimental data very difficult, especially when working on a time scale where processes like solvent and vibrational relaxation induce spectral dynamics. Additionally, the bulk behavior of a molecule has to be precisely known in order to be able to draw any conclusion from such data.

From the experimental point of view, one of the main experimental goals of the Ph.D. work presented in this thesis was to extent the assortment of tools available for studying ultrafast photoinduced processes at liquid interfaces. As a result, the current experimental set for investigating liquid interfaces includes: steady state SSHG with tunable probe excitation, TR-SSHG with single probe and tunable pump, TR-SSHG with tunable probe and tunable pump. This experimental section covers the detailed description of all these setups.

It has been mentioned that, in order to access such interfacial features as the molecular composition and the excited-state dynamics of adsorbates, the systematic comparison between interfacial and bulk data on the investigated molecular systems is of a crucial importance. The information on the excited-state dynamics of bulk systems was obtained using femtosecond transient absorption (TA) spectroscopy and time-resolved fluorescence techniques. The description of these setups is also given in this experimental section.

3.1. Bulk investigations

3.1.1. Steady state UV-VIS absorption and fluorescence

Absorption spectra were recorded on a Cary 50 spectrophotometer, whereas stationary fluorescence was measured on a Cary Eclipse fluorimeter. The fluorescence quantum yields were determined using rhodamine 6G in ethanol as a standard (Φ_{fl} = 0.95).[98]

3.1.2. Femtosecond transient absorption

The femtosecond electronic transient absorption (TA) is the spectroscopic pump-probe technique, which was used for studying photodynamics in bulk systems. The complete setup is presented in **Figure 3.1.**

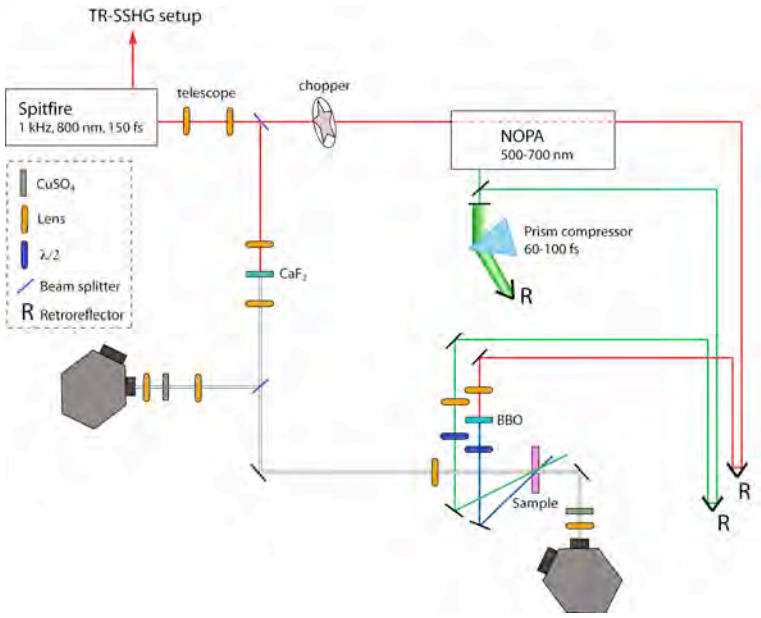

Figure 3.1. Scheme of the femtosecond TA setup.

A pump laser pulse excites the sample populating the excited state and triggering subsequent photochemical reactions. A second probe pulse measures the sample absorption at a given time delay after photoexcitation. The photoinduced changes are represented as absorption difference signal, ΔA, calculated from the unperturbed sample absorbance and the aforementioned time dependent transient signal (**Figure 3.2**). Femtosecond time resolution can be obtained when the pump-probe time delay

is determined by the relative path length of the two beams: it can be varied in an automated manner with a retroreflector mounted on a controlled translational stage.

Using a white light generation (a spectral broadening of ultrashort laser pulses in condensed media), the TA spectrum between ca. 350 and 800 nm (these values may vary as they depend on the laser central wavelength, the material used to broaden the laser pulse, the optics and detection system) can be collected at once, which allows observing the spectral changes with time.

An exceptional advantage of TA is to identify intermediate states that are non- or hardly emissive, thus invisible to time-resolved fluorescence techniques.

A TA spectrum contains several contributions as indicated in **Figure 3.2**: (1) ground-state bleach (GSB), which is a depletion of the electronic ground state by the pump pulse; (2) stimulated emission (SE) $S_n \rightarrow S_0$; (3) excited-state absorption (ESA) stemming from transitions of the $S_m \leftarrow S_n (m > n \neq 0)$ type (absorption of an excited state to a higher excited state) or from absorption of other transients (triplet state, ions formed in charge separation reactions, etc.).

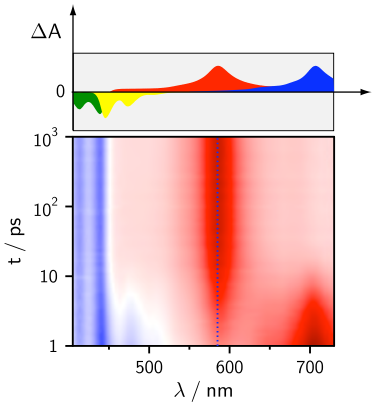

Figure 3.2. Origin of contributions to a TA spectrum: GSB is shown in green; SE in yellow; ESA in blue; absorption of other transients such as triplet state, or ions formed in charge separation reactions, is shown in red. The 3D map below represents the dynamics of each contribution.

The time evolution of these contributions, which are assigned to certain states, is not necessarily identical as, for instance, in the case of a triplet state involved in the excited-state dynamics: while the SE will vanish with a rate constant $k_{S_1} = k_{rad} + k_{IC} + k_{ISC}$, the characteristics time for the GSB decay will be the one of the triplet state lifetime (provided significant population of this state). A global analysis of the data is advantageous as it yields decay associated difference spectra (DADS) or species associated spectra (SADS), depending on the model.[99]

Setup. The TA setup used in this thesis was based on an amplified Ti:Sapphire laser system (*Millenia*, *Tsunami*, *Empower* seeding a *Spitfire* regenerative amplifier, all by *Spectra Physics*). The output consists of 150 fs laser pulses centered at 800 nm at 1 kHz repetition rate (**Figure 3.1**). Ca. 250 μJ were separated from the *Spitfire* for the pump laser beam. The pump beam was either frequency doubled in a 1 mm BBO crystal or sent to a home-built noncollinear optical parametric amplifier (NOPA), which provided laser pulses between 490 and 700 nm. The polarization of the pump pulses was controlled with respect to the white light probe pulses with a $\lambda/2$ waveplate. The intensity of the pump pulse was ~1 μJ at the sample and the beam was focused on the sample to diameters of ca. 300 μm.

The two-stage NOPA is based on the design by Riedle and co-workers.[100] The outcoming laser pulses are re-compressed in a SF10 prism compressor[101] to 60-100 fs FWHM.

Ca. 1 μJ were spectrally broadened in a 3 mm CaF_2 window to generate a white light (WL) that was used as a probe pulse. The CaF_2 window was constantly rotated in Lissajous-type manner to avoid its damage. The WL was collimated by a quartz lens and focused on the sample by a CaF_2 lens to a diameter of ca. 60 μm that is well below the diameter of the pump beam to avoid a walk-off when scanning the pump-probe delay stage.

The remaining 800 nm fundamental was extracted from the WL by an 800 nm mirror with 400-720 nm antireflection coating placed after the quartz lens and the spectrum was further flattened by an aqueous solution of $CuSO_4$ placed after the sample cell. The use of lenses usually leads to chromatic aberrations.[102] This, together with the WL fluctuations, leads to spectral distortions above ca. 720 nm.

The ~1nJ WL generated in the CaF_2 window was split into two parts: the signal beam, which was overlapped with the pump beam at the sample, and the reference beam. Both beams were spectrally dispersed in ANDOR Technology SR163 spectrographs and imaged onto back-thinned CCD detectors (*Hamamatsu* S07030-09); the detection system was assembled by *Entwicklungsburo Stresing*, Germany.

The pump beam was chopped at 0.5 kHz, and TA spectra were calculated from two consecutive probe pulses only. The reference probe beam served to correct for fluctuations of the amplifier on a shot-by-shot basis in order to improve signal-to-noise ratio.[103] A satisfactory signal-to-noise ratio was obtained by averaging typically 1500 difference spectra.

Liquid samples were contained in a 1 mm quartz cell (having two 1.3 mm thick windows) and were stirred by nitrogen bubbling to avoid photodegradation. The sample absorbance was adjusted to 0.1-0.3 at the excitation wavelength. The photostability of each sample was ensured by the absence of significant changes in the steady-state absorption spectrum after the TA measurement.

For the measurements of samples at different concentrations (**Section 4.1.2**), the sample absorbance was 0.8-0.9 for highly concentrated samples. The quartz cells with thicknesses of 1 mm, 10 μm and 1 μm were used for such measurements. In this case, instead of the nitrogen bubbling, a translational stage similar to the one used for the WL generation was constructed which allowed Lissajous-type movements of the sample during the TA scan. Due to high scattering, 3000 spectra were collected at each pump-probe time delay.

Data treatment. The chirp of the WL (meaning that time zero is different for every color in the WL) was determined by measuring the Optical Kerr Effect (OKE) signal in the pure solvent and the TA spectra were corrected by interpolation along the time axis (MatLab, *The Mathworks Inc.*).

There are several unwanted contributions to the TA signal during temporal overlap of the pump and probe pulses, e.g. the coherent signal, cross phase modulation and stimulated Raman from the solvent, which were not subtracted as the imperfection in the positioning of the translational stage (ca. 3 fs) does not allow for such procedure. Furthermore, singular value decomposition (SVD) used by several groups for data analysis or smoothing, was not employed.[104] Instead, a tail fit to the dynamics cut at ca. time zero plus the IRF (200 fs width determined as the FWHM of the OKE) was done using the IGOR Pro *Wavemetrics* software. At this time delay, the mentioned unwanted contributions to the TA signal are negligible.

The global analysis was done using multi-exponential functions with linked lifetimes at 5 nm intervals and DADS were obtained for each lifetime. Their interpretation is not always straightforward due to the overlap of SE, GSB and an unknown number of ESA bands that arise from different transients. Additional complications emerge from spectral shifts due to vibrational and solvent relaxation. Moreover, ESA bands, unlike fluorescence bands, can shift not only bathochromically (red shift) but also hypsochromically (blue shift).

The number of exponents needed to satisfactory describe the dynamics of the TA data was determined by visual inspection of traces and residuals. Due to the fact that many ultrafast processes do not follow exponential kinetics and due to sample inhomogeneity, several lifetimes might be associated with the same process.[99, 105] For instance, ultrafast electron or energy transfer can take place on the same time scale as vibrational relaxation (within a few picoseconds). Thus, it is experimentally challenging to distinguish them.

3.1.3. Time-resolved fluorescence measurements

Time-resolved fluorescence measurements on different time scales were carried out for the purpose of facilitating the data interpretation and they were not the main focus in this thesis, so the setups used to perform such measurements will be presented only briefly. A detailed description of these techniques could be found in literature.[106, 107]

Time-Correlated Single Photon Counting. Fluorescence lifetime measurements were performed using the time-correlated single photon technique (TCSPC) with a setup similar to the one described in detail in Ref.[107] The excitation was carried out with a laser diode (*Picoquant,* LHD-D-C-470) at 470 nm with a 10 MHz repetition rate. The pulse duration was 60 ps and the full width at half maximum (FWHM) of the IRF was ca. 200 ps. The fluorescence was collected at magic angle after passing through a longpass filter (*Schott* OG530).

Fluorescence up-conversion. The fluorescence dynamics on a femtosecond timescale was measured with a fluorescence up-conversion setup.[106] Briefly, the frequency doubled output of a Ti:Sapphire laser (*Mai Tai, Spectra Physics*) was used to excite the sample at 480 nm with an energy of about 7 μJ cm^{-2}. The polarization of the pump pulses was at magic angle relative to that of the gate pulses. The samples were placed in a rotating cell, whose thickness was 0.4 mm, to avoid photodegradation. The IRF of the instrument was about 230 fs.

3.2. Interface investigations

All three SSHG setups presented in this section were successively built in our laboratories so that all of them were involved in the experimental work at the different stages of this Ph.D. work. All the setups are based on a similar experimental concept, e.g. they have a similar beam geometry and SSHG signal collection. For this reason, the detailed scheme will be presented only for the latest version of the setup (**Section 3.2.3**). The excitation and detection modules as well as the optical layout are unique for each setup, and thus will be described separately.

3.2.1. Steady state SSHG with tunable probe pulses

By analogy with the UV-visible one-photon absorption spectrum, which is measured to characterize the energetic transitions of a molecule and its chemical composition in a bulk solution, measuring the SSHG intensity upon the tunable probe excitation results in the interfacial spectrum, which points out to the energetic transitions of the interfacial molecules via both one- and two-photon resonances. Accordingly, such SSHG spectrum provides the access to the chemical composition of molecular adsorbates at the interface.

Setup. Measurements of the stationary SSHG intensity between 385 and 520 nm were performed with a setup based on a Ti:Sapphire oscillator (*MaiTai*, *Spectra Physics*) generating ~100 fs pulses at 82 MHz, tunable between 770 and 1040 nm. About 300 mW of the laser output beam was focused with a 500 mm lens onto the interface with an angle of incidence of about 70º where it underwent total internal reflection (TIR). To eliminate unwanted SSHG signal originating from the surfaces of the optical components, a long-pass filter was located just in front of the sample cell. The SSHG signal was collected by a 100 mm lens, cleaned out from the fundamental probe light with a short-pass filter and focused onto the entrance slit of a 0.25 m monochromator (*Cornerstone* 260, *Oriel*) with a 60 mm lens, before being detected with a photomultiplier tube operating in photon counting mode (R6353P, *Hamamatsu*). The digitized output of the counting electronics was read by a computer that also controlled the tuning of the laser wavelength. The SSHG intensity was corrected for the wavelength dependence of the output power and the spectral response of the

optics and detection. The wavelength dependence of the pulse duration was not taken into account.

3.2.2. TR-SSHG with single-wavelength probe pulses and tunable pump pulses

To access the information on the dynamics of photoinduced processes at liquid interfaces, the electronic SSHG has to be time resolved. In this case, a pump pulse excites the molecules located in one of the phases, so that the change of the SSHG signal is recorded as a function of the time after excitation. The first version of TR-SSHG setup was built using the single-wavelength probe and tunable pump scheme.

Setup. The TR-SSHG setup with single-wavelength probe pulses and tunable pump pulses is based on an amplified Ti:Sapphire system producing ~100 fs pulses around 800 nm at 1 kHz. A fraction of this output was used to feed a noncollinear optical parametric amplifier (*NOPA Clark-MXR*) generating ~50 fs pulses, tunable between 480 and 700 nm. These pulses were directed toward the interface from above through the transparent organic phase and focused with a combination of spherical and cylindrical lenses to ensure an optimal overlap with the probe pulses. The pump pulses (typically 1 to 2 μJ) excited the dye molecules dissolved in the aqueous phase with no interfacial selectivity. Circular polarization was used to prevent a photoselection of the molecules according to the orientation of their transition dipole moment in the interfacial plane. For SSHG probing, a small fraction of the 800 nm amplifier output (10−100 nJ) struck the interface from the transparent and high-refractive-index phase and underwent TIR. These probe pulses and the SH signal were reflected at the interface at different angles because of the dispersion in the transparent phase. The signal was collected with a lens, filtered out from the accompanying scattered fundamental light with a blue filter, and focused onto a monochromator equipped with a multipixel photon counter avalanche photodiode detector. The output signal was further processed with a boxcar gated integrator and averager module before being digitized and stored on a computer.

The probe pulses were linearly polarized, and in order to measure specific elements of the $\chi^{(2)}$ tensor, a half-wave plate and a polarizer were located before the sample and the detector, respectively. In particular, the SSHG time profiles were recorded in F-s, SH-p polarization configurations, meaning s-polarization of the fundamental

excitation with the selected p-component of the SSHG, and F-m, SH-s, meaning the polarization at 45° with the respect to the plane of incidence of the fundamental excitation with the selected s-component of the SSHG, as shown in **Figure 3.3**. Each of these polarization configurations ensures probing a specific element of the second order nonlinear optical susceptibility tensor $\vec{\chi}^{(2)}$: $\chi^{(2)}_{zxx}$ in the case of F-s, SH-p configuration, and $\chi^{(2)}_{xxz}$ in the case of F-m, SH-s configuration.[108]

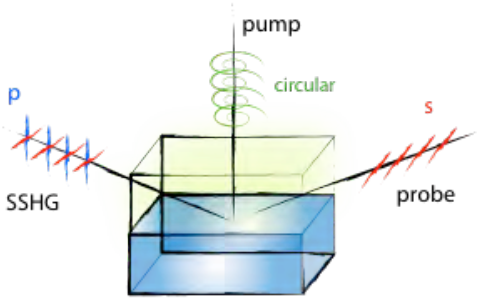

Figure 3.3. Polarization configurations in the TR-SSHG experiment: probe (fundamental) excitation is either s- or m- linearly polarized, and the p- or s- SH component is detected, respectively. The pump is circularly polarized to prevent a photoselection of the molecules.

The SH intensity depends not only on the square modulus of the nonlinear susceptibility but also on geometrical factors such as the linear and nonlinear Fresnel factors for reflection. The latter is particularly large near the critical angle for TIR. For this reason, TIR geometry is usually used in TR-SSHG at liquid interfaces. This is, of course, not possible for air/liquid interfaces, and for this reason, the SH intensity is usually much weaker than at liquid/liquid interfaces.

3.2.3. TR-SSHG with tunable probe pulses and tunable pump pulses

The TR-SSHG setup with tunable probe pulses and tunable pump pulses is a recently built and the most advanced instrument for investigation of liquid interfaces in our group. The full tunability of the probe pulses allows monitoring the dynamics of different excited states via resonance enhancement, which helps identifying different species at the interface and thus greatly facilitates data interpretation. Moreover, such effort is a crucial step toward bringing the interface-selective techniques at a level close to that of the methods available for the investigation of bulk solutions.

Setup. The pump pulses (3-4 µJ at the interface, ~80 fs) were generated with a two-stage non-collinear OPA (*TOPAS White, Light Conversion*), whereas the probe pulses (50-200 nJ at the interface, ~100 fs) were produced with a collinear OPA (*TOPAS C, Light Conversion*) allowing full tunability in the UV, VIS and mid-IR ranges. Both

TOPAS were pumped by 1 mJ and 100 fs pulses at 800 m produced by a 1 kHz Ti:Sapphire amplified system (*Solstice*, *Spectra Physics*). The key elements of the setup, polarization configurations, and the beam geometry are similar to the setup described in section **3.2.2.** The scheme of the setup is shown in **Figure 3.4**.

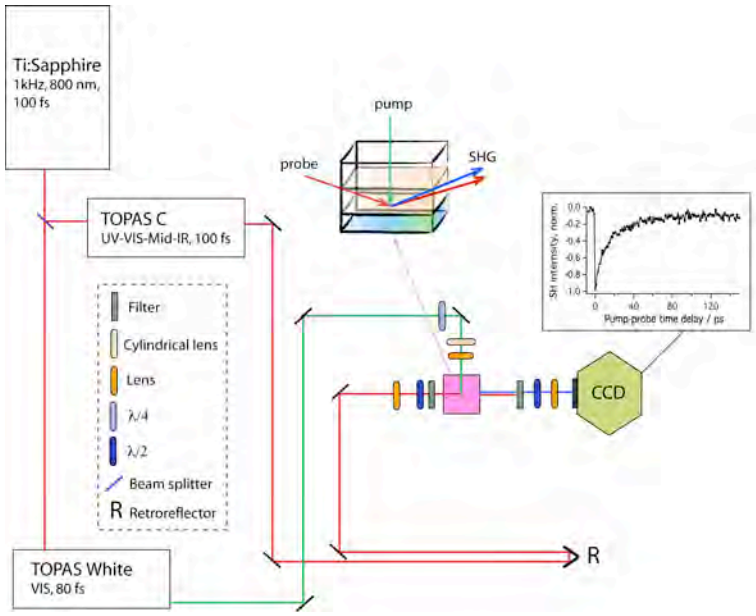

Figure 3.4. Scheme of the TR-SSHG setup with tunable probe pulses and tunable pump pulses.

The signal was focused onto the entrance slit of a Czerny-Turner spectrograph (*Shamrock 163*, *Andor*) equipped with a multipixel cooled CCD camera (*Newton 920*, *Andor*). The illuminated pixels were vertically binned, summed over the wavelength range of interest, and the resulting value transferred to a computer.

3.2.4. Data treatment

The non-resonant contribution to the SSHG signal measured without a chromophore in the aqueous phase was found to be vanishingly small. Therefore, with dye present in the aqueous phase, the SSHG signal has a purely resonant character and its intensity depends on the square modulus of the relevant elements of the second-order nonlinear optical susceptibility tensor, $\vec{\chi}^{(2)}$, hence on the square of the number of dye molecules contributing to the signal. Analysis of the TR-SSHG profiles was performed on a processed signal, $S(t)$, obtained by first taking the square root of the measured SSHG intensity and, second, normalizing the resulting values so that $S(t)$ is

equal to zero at negative pump-probe delays, and is equal to either 1 or -1 at its maximum photoinduced change, depending on whether the SSHG signal increases or decreases upon excitation, respectively. The so-obtained signal intensity, $S(t)$, is proportional to the photoinduced population changes.[76]

3.2.5. Sample preparation and experimental specifics

Sample preparation, experimental specifics and all supporting information are presented in **Appendices** (**Section 6**).

4. RESULTS AND DISCUSSION

This section focuses on the application of the TR-SSHG technique to the investigation of photoinduced processes at liquid/liquid interface by the example of several molecular probes. It will be shown that the measurements by TR-SSHG can yield information on the molecular probe itself adsorbed at the interface as well as on the environmental properties that this molecular probe experiences. Therefore, this section is composed of three main parts: *in the first part*, the interfacial photophysics of the investigated molecules will be discussed; *in the second part*, a few examples will show how the photophysics of a molecule can be used as a tool of getting information on the environment at the interface; *in the third part*, the potential of TR-SSHG for investigating photoinduced ET at and through liquid interfaces will be demonstrated.

4.1. Photophysics of molecular probes adsorbed at liquid interfaces

4.1.1. Photophysics of Malachite Green

Because of the different local properties of interfaces, solute molecules adsorbed at an interface could exhibit a reactivity that differs from that of the same molecules dissolved in the bulk. For example, the friction exerted by the environment, which in bulk solutions can be predicted from the viscosity, influences the dynamics of many chemical reactions. Because viscosity cannot be defined at a liquid interface, the friction has to be determined directly, using, for example, the dynamic probe approach. Triphenylmethane dyes such as Malachite Green (MG) and Brilliant Green (BG) are well-suited probes because the lifetime of their lowest singlet excited state depends on the viscosity (**Figure 4.1**).[51, 74, 109, 110]

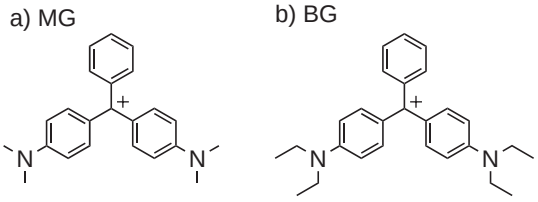

Figure 4.1. Malachite Green (a) and Brilliant Green (b) cations.

Figure 4.2 shows the electronic absorption spectrum of MG in water, together with the SSHG spectrum measured with MG at the dodecane/water interface.[111] The band culminating at 618 nm corresponds to the $S_1 \leftarrow S_0$ transition, whereas that at 425 nm is due to the $S_2 \leftarrow S_0$ transition. The square root of the SSHG signal intensity measured upon probing between 760 and 1000 nm matches the linear absorption spectrum between 380 and 500 nm, pointing to a signal enhancement via a two-photon resonance. A similar result has recently been obtained at the air/water interface by Tahara and co-workers using broadband electronic SSFG.[112]

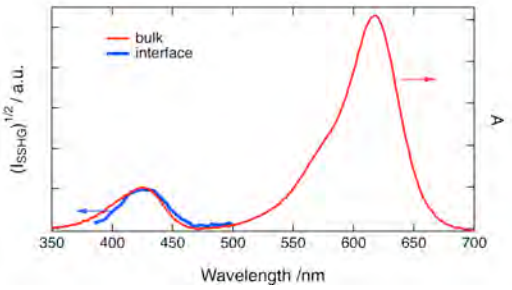

Figure 4.2. Stationary SSHG spectrum of MG at the dodecane/water interface and electronic absorption spectrum of MG in water.

MG has been the subject of numerous time-resolved spectroscopic experiments to understand the origin of the ultrafast nonradiative relaxation of its S_1 state in solution.[113, 114] Moreover, MG has already been shown to be a very good interfacial probe for TR-SSHG studies.[110, 112] It is generally agreed that the process is intrinsically barrierless and involves the motion of the aniline and/or phenyl substituents around the single bond to the central carbon atom. The friction exerted by the environment on the rotating rings leads to the viscosity dependence of the excited-state lifetime. However, a few questions regarding the deactivation pathway of MG remained unanswered. For example, the nature of the state populated directly upon internal conversion from the S_1 state has been questioned. To clarify this issue and to calibrate the viscosity dependence of the S_1 lifetime of MG and BG precisely, their excited-state dynamics was investigated by transient absorption spectroscopy in water-glycerol solutions of various compositions.[115] The dynamics could be well reproduced by assuming an A → B → C → D scheme, where the A → B step occurs on the subpicosecond time scale, independently of viscosity, and the time constants of the B → C and C → D steps exhibit a $\tau \propto \eta^{\alpha}$ viscosity dependence with $\alpha \approx 0.6$ and 0.75 for MG and BG, respectively. From this analysis, the intermediates could be

identified with the Franck−Condon (A) and the vibrationally relaxed S_1 states (B) and the twisted (C) and the relaxed S_0 states (D).

After MG was properly calibrated as a dynamic probe for friction, its excited-state dynamics was measured at the air/water interface by TR-SSHG.[116] For these measurements, MG was excited to the S_1 state at 615 nm and probing was done at 800 nm, with the SH signal at 400 nm being in resonance with the $S_2 \leftarrow S_0$ transition. The resulting time profile is shown in **Figure 4.3**, and the processed intensity, *S(t)*, could be well reproduced using a biexponential function with 1-2 and ~10-20 ps time constants, in good agreement with measurements by other groups.[110, 112] While the shorter time constant could be ascribed to the decay of the excited state (i.e., to the B → C step), the assignment of the 20 ps component was more ambiguous and will be discussed in more detail below.

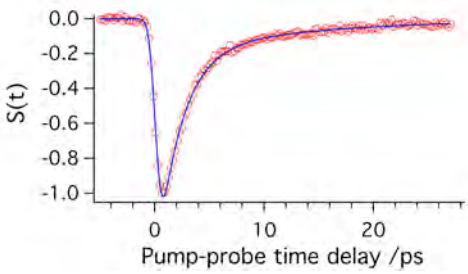

Figure 4.3. TR-SSHG profile of MG measured at 400 nm, upon excitation at 618 nm, at air/water interface and its best fit with the biexponential function.

The 1-2 ps S_1 lifetime of MG at the air/water interface should be compared to the 570 fs found in bulk water. The friction exerted by interfacial water is clearly larger than that exerted by bulk water, pointing to an arrangement of water molecules at the interface that results in a more rigid structure. According to polarization-dependent SSHG measurements, the polar aniline groups of MG are located in the aqueous phase whereas the phenyl group points toward the nonpolar phase.[110] The motion of the aniline groups is thus unambiguously involved in the nonradiative relaxation of the S_1 state of MG. To find out whether the S_1-state lifetime of MG also follows an η^{α} dependence at the interface and to be able to vary the viscosity of both phases, the measurements were performed at liquid/liquid interfaces.[115] First, the bulk viscosity of the nonpolar phase was kept constant, whereas that of the aqueous phase was changed by adding various amounts of glycerol. The interfacial ground-state recovery (GSR) dynamics of MG and BG was found to follow an η^{α} dependence as well (**Figure 4.4 right**). However, α was around 0.4 for both MG and BG, substantially

smaller than the bulk values of 0.6 and 0.75. This implies that although the excited-state lifetime is always longer at the interface than in the bulk, this difference decreases with increasing glycerol concentration. There might be several reasons for this effect. The most evident one is that the addition of glycerol affects interfacial friction less than bulk friction. It could result from a structural modification of water several molecular layers below the interface: this layer could encompass entirely the aniline groups of either dye, including the alkyl substituents. The MD simulations by Clark et al. suggest that there is a layer of increased viscosity due to an enrichment of glycerol near the interface, and that this special layer covers the aniline substituents of the dyes.[117]

Another question concerning the excited-state dynamics of MG and BG was whether a large-amplitude motion of the phenyl group is also involved in the nonradiative deactivation of the S_1 state. Previous TR-SSHG measurements of MG at octane/water and pentane/water interfaces pointed to the same excited-state decay time, indicating a negligible role of the phenyl group.[110] Measurements from our group confirmed this result with seven alkanes up to tetradecane with an S_1 lifetime of around 2 ps.[115]

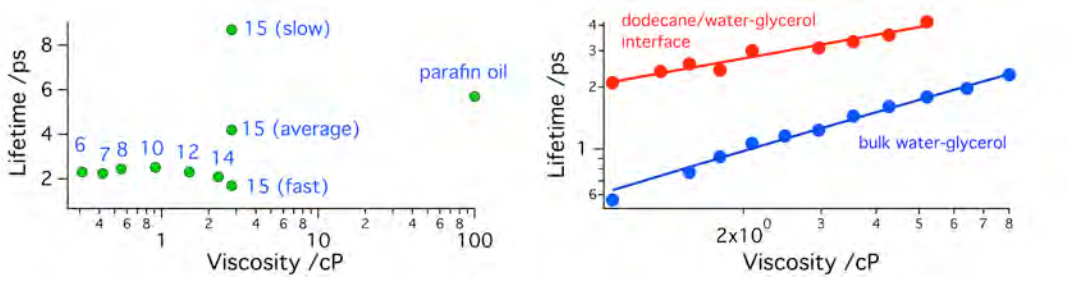

Figure 4.4. Viscosity dependence of the excited-state lifetime of MG at alkane/water-glycerol interfaces. **Left**: variation of the viscosity of the alkane phase (the numbers indicate the number of carbon atoms of the alkane; the decay in pentadecane is biphasic and both time constants and the average are given). **Right**: variation of the viscosity of the aqueous phase and a comparison with the lifetime in bulk solutions.

However, a 5.7 ps lifetime was measured when going to the much more viscous paraffin, showing that the hindrance of the phenyl group twist also slows down the excited-state decay of MG (**Figure 4.4 left**). Higher friction is required to slow down the reorientation of the smaller, nonpolar phenyl group relative to the larger, polar aniline groups. It is probable that the interfacial friction of alkane with a bulk

viscosity of < 2.1 cP is too weak to slow down the motion of the phenyl group below that of the anilines in water.

When studying the concentration dependence of the TR-SSHG profiles of MG at alkane/water interfaces, it was found that the dynamics was only biphasic above ~$5 \cdot 10^{-6}$ M and that the relative amplitude of the slow component increased up to about 0.2 at $5 \cdot 10^{-5}$ M and then remained mostly constant.[115] This slow component was ascribed to interfacial MG aggregates, for which large-amplitude motion is hindered and nonradiative transition to the ground state is slower. Aggregation of MG in bulk solution occurs only at very high concentrations.

So far, TR-SSHG investigations of MG have been carried out using single wavelength probing at either 800 or 625 nm, i.e. either in two-photon resonance with the $S_2 \leftarrow S_0$ transition or in one-photon resonance with the $S_1 \leftarrow S_0$ transition,[110, 115, 116, 118] with the excitation of the $S_1 \leftarrow S_0$ band.

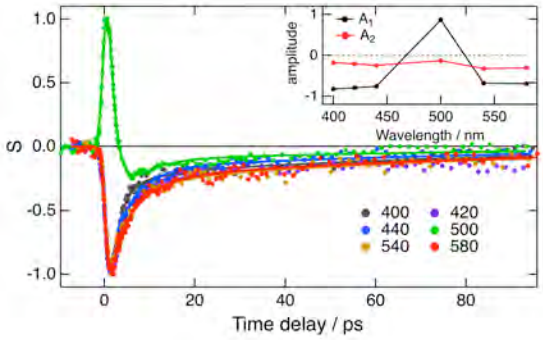

Figure 4.5. TR-SSHG profiles measured at different wavelengths with MG ($1.5 \cdot 10^{-4}$ M) at the dodecane/water interface. Inset: amplitudes of the fast (A_1, 1.3 ps) and slow components (A_2, 25 ps) obtained from global biexponential analysis.

Figure 4.5 shows TR-SSHG profiles, *S(t)*, obtained by probing the interface between 800 and 1160 nm upon 618 nm excitation.[111] Except for that measured at 500 nm, i.e. upon probing at 1000 nm, these profiles are almost identical, and exhibit a prompt decrease at time zero followed by a biphasic recovery of the intensity, as previously observed upon 625 and 800 nm probing. This result is also in agreement with the TR-SSFG signal measured between 360 and 470 nm with MG at the air/water interface by Tahara and co-workers.[112]

By contrast, the TR-SSHG profile at 500 nm exhibits first a prompt rise at time zero, indicative of an increase of the SSHG intensity upon excitation, followed by a fast decay to a negative value and by a subsequent rise to zero. All these profiles could be well reproduced by the convolution of a Gaussian function accounting for the instrument response with the sum of two exponential functions with time constants of

1.3±0.2 and 25±3 ps, and the relative amplitudes shown in the inset of **Figure 4.5**. **Figure 4.2** indicates that the stationary SSHG intensity at 500 nm is very weak because of the absence of a resonance enhancement. On the other hand, previous transient absorption measurements in bulk solutions revealed the presence of an $S_n \leftarrow S_1$ absorption band between 450 and 550 nm.[115, 116] As a consequence, the positive component of the TR-SSHG signal at 500 nm is ascribed to a two-photon resonance with the $S_n \leftarrow S_1$ transition and its temporal evolution reflects that of the S_1 state population of MG. At the other wavelengths, the resonant enhancement is dominated by the two-photon $S_1 \leftarrow S_0$ and $S_2 \leftarrow S_0$ transitions and the fast component of the TR-SSHG signal reflects the ground-state recovery of MG.

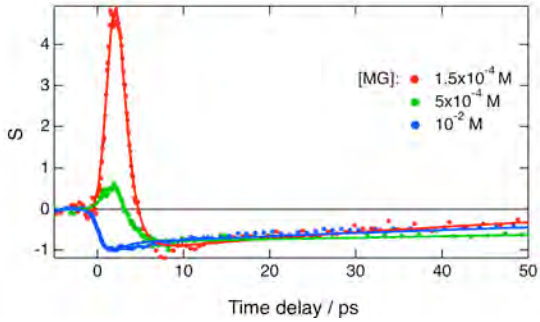

Figure 4.6. TR-SSHG profiles measured at 500 nm with different bulk concentrations of MG at the dodecane/water interface (for better comparison, the profile at low concentration was normalized at -1).

Figure 4.6 shows that the relative amplitude of the positive signal component at 500 nm strongly decreases upon increasing MG concentration, and totally vanishes at 10^{-2} M. This effect fully supports the assignment of this short-lived positive feature to the MG excited state. It further confirms that the slow component is due to MG aggregates.

Summary. This investigation showed that TR-SSHG measurements could yield information not only on the interfacial properties (friction in this case) but also on the probe itself (i.e., the involvement of the phenyl group). The MG excited-state dynamics is affected by the presence of aggregates: as the relative amplitude of the slow component increased with increasing MG concentration, the fast and slow components were assigned to the ground-state recovery of monomers and aggregates, respectively. Finally, it was demonstrated that the access to the TR-SSHG profiles recorded at several wavelengths greatly facilitates data interpretation.

4.1.2. Photophysics of Rhodamine 6G

Although rhodamine 6G (R6G, **Figure 4.7**), besides having excellent lasing properties, is one of the most extensively used dyes in photophysics, photochemistry and biotechnology, there still is no conclusive study, to our knowledge, on its ultrafast excited-state dynamics, neither in bulk nor at liquid interfaces.

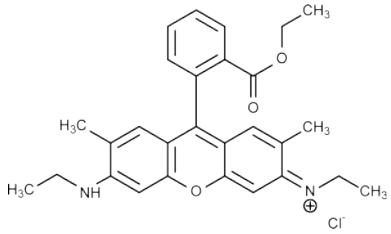

Figure 4.7. Rhodamine 6G

R6G is known to undergo self-association at high concentrations, forming dimers, trimers, and higher order aggregates. Such aggregation formation dramatically modifies the absorption characteristics of the dye, manifesting itself in e.g. spectral shifts and band splitting.[119]

Penzkofer et al. presented the fluorescence spectra and fluorescence quantum efficiencies of R6G in methanol and in water measured for various concentrations up to the solubility limits (0.66 M for methanol and 0.027 M for water), with distinguished monomer and dimer contributions.[120, 121] In both solvents, quenching of the fluorescence by the Förster-type energy transfer to weakly fluorescing dimers (closely spaced pairs in methanol and ground-state dimers in water) was demonstrated.

Arbeloa et al. reported on the dimerization and trimerization of R6G in aqueous solution pointing out that at higher concentration the monomers get efficiently quenched by the aggregates, due to the long-range (Förster type) energy transfer.[122]

Li et al. used total internal reflection synchronous fluorescence spectroscopy for investigating adsorption of R6G at the silica/water interface. It was found that the interface fluorescence spectrum of R6G, compare to the bulk one, exhibits a small red shift explained by the limitation of freedom of rotational movement of R6G molecules at the interface. A self-quenching of adsorbate at the interface at higher R6G concentration was also demonstrated.[123]

Eisenthal and co-workers reported on the rotational relaxation of R6G at the air/water interface by TR-SSHG to take place within 1 ns,[124] which appears to be slower than the 200 ps rotational relaxation time in bulk water.[125]

This section reports on the ultrafast excited-state dynamics of R6G in bulk water and at the dodecane/water interface using a combination of TA and TR-SSHG techniques, respectively. The study was performed at different concentrations of R6G and different polarization configurations, which helped distinguishing contributions of R6G monomers and aggregates into the excited-state dynamics in both TA and TR-SSHG experiments and elucidating the R6G deactivation mechanism in bulk and at the interface.

Figure 4.8 shows the electronic absorption spectrum of R6G in water at different concentrations. Clearly, upon increasing the concentration, the relative intensity of the bands at 530 nm ($S_1 \leftarrow S_0$ transition) and at 500 nm changes in the favour of the latter. This phenomenon has been already observed before and assigned to the self-aggregation of the dye by H-type contacts.[119]

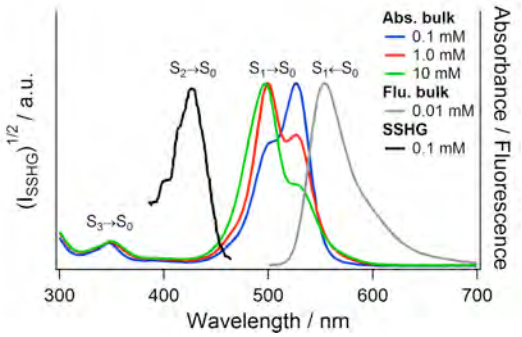

Figure 4.8. Stationary SSHG spectrum of R6G at the dodecane/water interface (black solid line) and electronic absorption spectrum of R6G in bulk water (color solid lines).

Figure 4.8 also shows the interfacial spectrum that is the square root of the SSHG signal intensity measured upon probing between 770 and 930 nm. The interfacial spectrum of R6G matches its two-photon excitation spectrum revealing a two-photon resonance with the $S_2 \leftarrow S_0$ transition at 425 nm,[126] so that probing this transition enhances the SSHG signal of R6G at dodecane/water.

The excited-state dynamics of R6G at different concentrations in bulk water on a sub-ns timescale was investigated using the TCSPC technique (**Figure 4.9**). Monoexponential decay of the time profiles was assigned to the fluorescence of the R6G monomers, since dimers and higher order structures of R6G based on H-type contacts are not fluorescent.[119] The lifetime obtained from the TCSPC experiment

shortens with the concentration, going from 4.6 ns at 0.1 mM, to 3.7 ns at 1 mM and 380 ps at 10 mM. This trend is in agreement with the experiment of Penzkofer et al. who measured the fluorescence lifetimes of highly concentrated solutions of R6G in methanol and attributed the fluorescence quenching of R6G to the energy transfer from monomers to aggregates.[120]

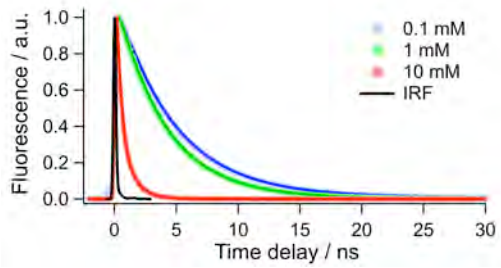

Figure 4.9. Time-resolved fluorescence of R6G in bulk water at 0.1 mM, 1 mM, and 10 mM measured with TCSCP.

The excited-state dynamics on a shorter timescale was studied using the TA technique. The TA spectra were, in most cases, contaminated by strong scattering of the pump beam at 530 nm or 500 nm, resulting in distortions of the ground-state bleach that is situated in this spectral region. As the bleach contains useful information about the species, it is important to recover its real shape and intensity over the whole experimental spectral window. With that goal, the data for each concentration and excitation wavelength were analyzed globally using a routine based on matrix reconstruction algorithm[127] written in MATLAB (*The MathWorks Inc.*). The experimental TA spectra could, in all cases, be well reproduced with a biexponential function. To illustrate the robustness of the procedure, **Figure 4.10** shows a comparison of the original experimental data and the corresponding simulated data, along with the associated residuals map. Careful inspection of the latter reveals only high frequency noise caused by scattering in the pump region. The fact that the residuals maps do not exhibit any structured features in the time or in the spectral

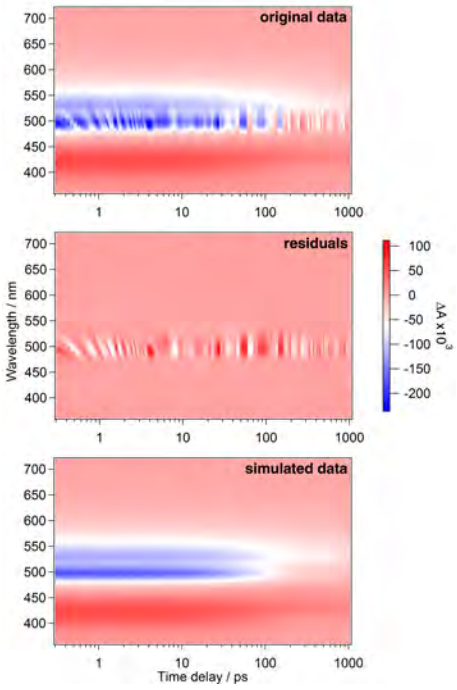

Figure 4.10. Original TA data, residuals, and simulated TA data for 1 mM of R6G upon 500 nm excitation.

domain ensures a good recovery of the spectro-temporal dynamics over the whole data set. Qualitatively similar residuals maps as shown in **Figure 4.10** were obtained for all TA spectra; therefore, here the simulated spectra obtained with the aforementioned method are presented (**Figure 4.11**), whereas the experimental spectra are shown in **Section 6.2**.

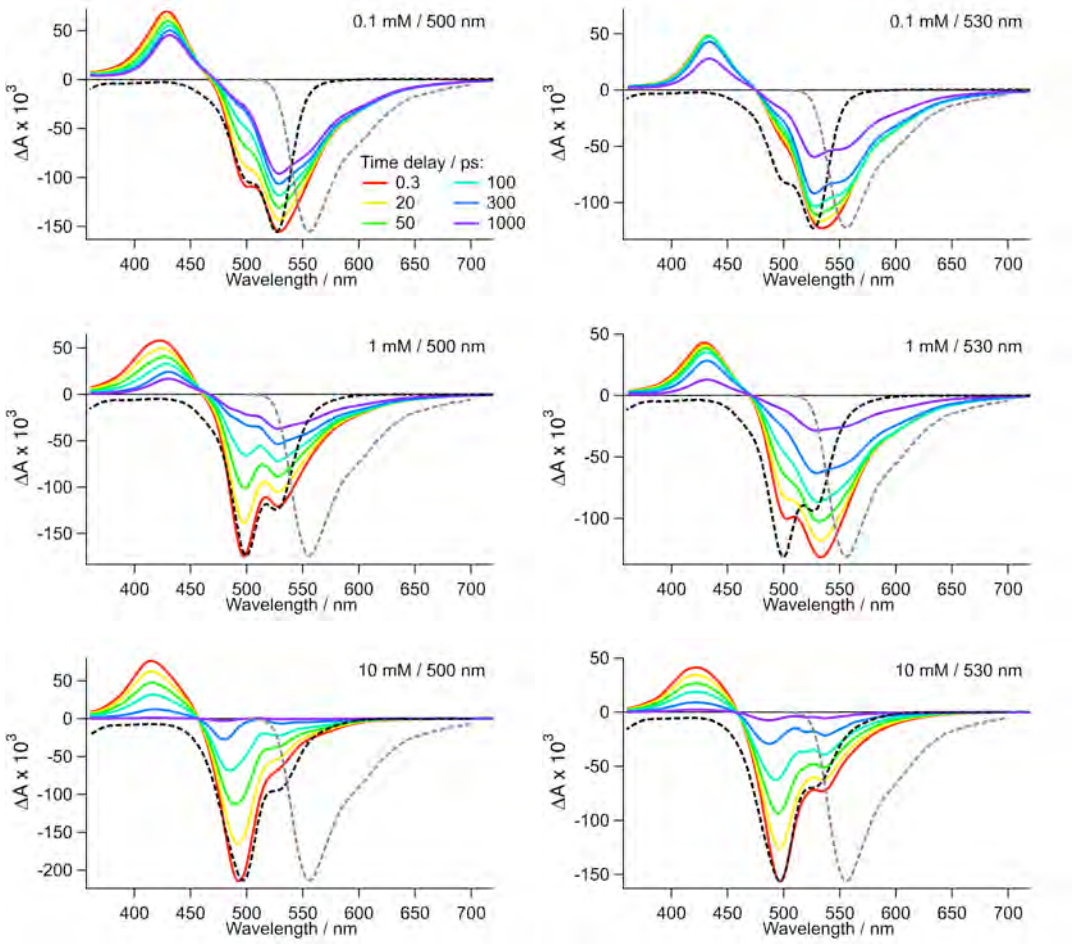

Figure 4.11. Global analysis of the TA spectra of R6G in bulk water recorded upon excitation at 530 nm and 500 nm, at concentrations 0.1 mM, 1 mM and 10 mM. For better visualization, each data set shows 6 spectra at different time delays. The spectra are color-coded according to their time delay, from red (300 fs) to purple (1.0 ns). The dashed black and grey lines represent the scaled absorption and the stimulated emission spectra (calculated by multiplying the stationary fluorescence intensity by λ^4), respectively.

These spectra are dominated by an intense and structured negative band in the 470-550 nm region, which can be ascribed to the bleach of the $S_1 \leftarrow S_0$ absorption. A second band whose intensity varies with concentration is also apparent, extending

from 550 to 700 nm, and is associated with stimulated emission (SE) from R6G monomers as this spectral region corresponds to that of the fluorescence emission. A positive band can also be observed at shorter wavelengths, below 470 nm, and is assigned to excited-state absorption (ESA).

The shape of the ground-state bleach (GSB) is consistent with the stationary absorption spectrum for all concentrations and exhibits the same concentration dependence. The discrepancies observed between GSB and stationary absorption after 530 nm excitation for 0.1 mM and 1 mM are caused by the overlapping SE signal. Furthermore, the shape of the GSB changes with the excitation wavelength: the intensity ratio of the 500 nm and 530 nm bands changes in favour of the latter when the sample is excited at longer wavelengths as a result of increased depletion of the monomer form. The SE is also clearly dependent on both the concentration and the excitation wavelength. Its intensity decreases with the concentration, in agreement with the fluorescence quenching due to energy transfer from monomers to aggregates. The loss of intensity of the SE band when going from 530 nm to 500 nm excitation can be explained by the fact that at 500 nm, mostly non-fluorescent aggregates are excited, whereas at 530 nm highly fluorescent monomers are being pumped. Finally, the ESA shifts to lower wavelengths and broadens with increasing concentration, possibly originating from a wider distribution of aggregates conformations at high concentration.

The spectra for each concentration and each pump wavelength were analysed globally with a biexponential function, yielding pairs of time constants and decays associated difference spectra (DADS) that are listed in **Table 4.1** and shown in **Figure 4.12**, respectively. The slow component (τ_2) is of the order of a few ns for 0.1 mM and 1 mM, and a few hundreds ps for 10 mM, in good agreement with the excited-state lifetime of the monomer obtained by time-resolved fluorescence measurements. A second shorter component (τ_1) of ~70 ps was present in all data sets, independently of the concentration. These two components are respectively attributed to the excited-state deactivation of the monomers and the aggregates. The shortening of the slow component, associated with the monomer dynamics, with the concentration can be explained by the very efficient quenching through energy transfer to the aggregates. The component that was attributed to the aggregates is of the same order of magnitude as the one reported for the similar dye, rhodamine B, by Smirl et al. who

determined the excited-state lifetimes of the dimer to be 100 ps in aqueous solutions of concentration ranging from 10^{-5} to 10^{-3} M.[128] This assignment is also supported by the spectral features of the DADS of the fast and slow components in the GSB region: the DADS of the fast component clearly exhibit an intense feature at 500 nm, where the aggregate band is located, whereas the one associated with the slow component shows a more pronounced feature at 530 nm, where the monomer band is located.

Concentration	τ_1 (500 and 530 nm)	τ_2 (500 nm)*	τ_2 (530 nm)*
0.1 mM	66 ps	> 3.0 ns	1.6 ns
1 mM	69 ps	2.1 ns	920 ps
10 mM	69 ps	320 ps	520 ps

Table 4.1. The time constants obtained from the biexponential global fit of the TA data measured upon excitation at 530 nm and 500 nm, for R6G concentrations of 0.1 mM, 1 mM, 10 mM in bulk water. *The error on τ_2 is up 50% as the time window (1.0 ns) of the experiment is too short compared to the lifetime.

Moreover, the DADS of the slow component contain the contribution from SE, originating from monomers, while that of the fast component does not. It is particularly visible at the lowest concentration, in which case the SE is the strongest. For a given concentration, the short/long component amplitude ratio is systematically higher after 500 nm than after 530 nm excitation, reflecting the photoexcitation of mostly aggregates or monomers, respectively.

All of the above undoubtedly confirms the formation of aggregates at high concentration, as already observed by stationary spectroscopy, and reveals their much faster excited-state dynamics compared to that of the monomers.

At low concentrations of R6G, upon excitation at 500 nm, the ESA additionally “shifts” to longer wavelengths at longer time delays. This “shift” could be explained by the fact that the ratio of monomer and aggregate contributions to the excite-state dynamics of R6G changes on the time scale of the experiment: at shorter time delays both monomers and aggregates of R6G contribute to the dynamics whereas at longer time delays the monomers have the dominating contribution as they are longer-lived compare to the aggregates. This effect, however, vanishes when the contribution of either monomers or aggregates entirely dominates, e.g. either at high concentrations

of R6G as in this case the aggregates are being almost exclusively probed, or upon excitation at 530 nm where the long-lived monomers are mostly probed.

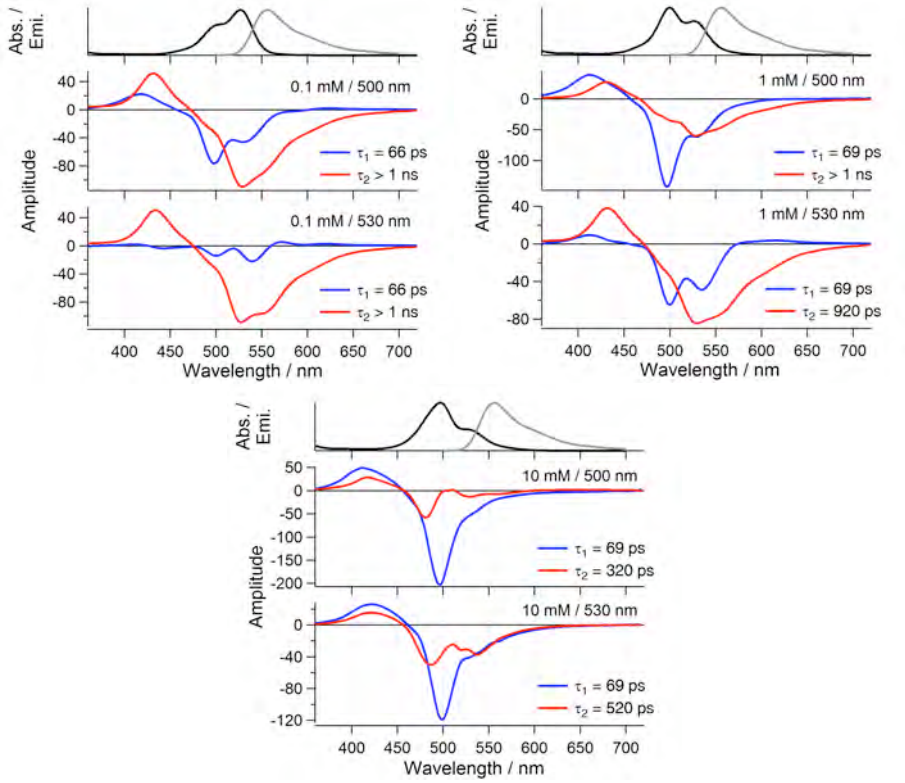

Figure 4.12. DADS obtained from the global analysis of the TA spectra of R6G in water recorded upon excitation at 530 nm and 500 nm, at concentrations of 0.1 mM, 1 mM and 10 mM. The black and grey lines in the upper panels respectively represent the stationary absorption spectrum and the stimulated emission spectrum (calculated by multiplying the stationary fluorescence intensity by λ^4).

TR-SSHG profiles of R6G were measured at the dodecane/water interface, under different resonance enhancement conditions, probing either the $\chi^{(2)}_{zxx}$ or $\chi^{(2)}_{xxz}$ tensor elements, and pumping at 530 nm for three concentrations of R6G. The results are displayed in **Figure 4.13**.

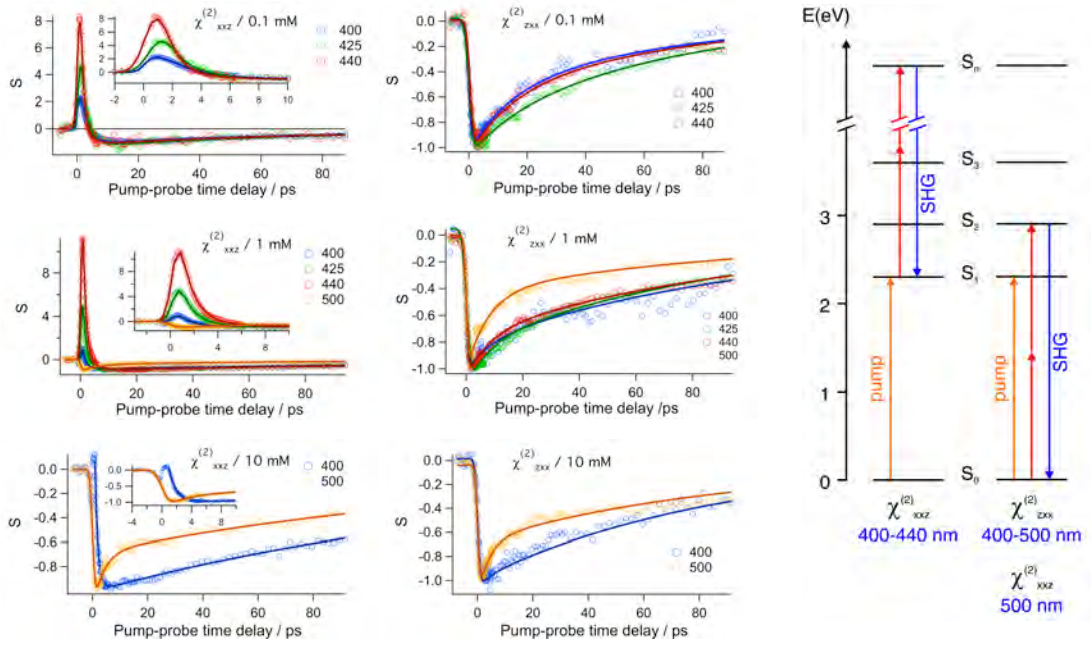

Figure 4.13. TR-SSHG profiles of R6G measured with either $\chi^{(2)}_{zxx}$ or $\chi^{(2)}_{xxz}$ tensor elements, upon excitation at 530 nm, for R6G concentrations of 0.1 mM, 1 mM, 10 mM at the dodecane/water interface. Insets in the left graphs show the corresponding graphs on the 10 ps time scale. The dynamics are normalized to their minimum. Solid lines in each graph represent the fit. The energy level scheme of R6G on the right shows the corresponding resonance enhancement for $\chi^{(2)}_{xxz}$ and $\chi^{(2)}_{zxx}$ tensor elements.

In the case when $\chi^{(2)}_{xxz}$ tensor element is probed at 400-440 nm, the TR-SSHG profiles of R6G for 0.1 mM and 1 mM show first a prompt rise at time zero, indicating an increase of the SSHG intensity upon excitation followed by a fast decay to a negative value and by a subsequent recovery to zero. On the other hand, the profiles at 500 nm show only a rapid depletion and subsequent recovery. Since our TA data reveal the presence of an ESA band below 470 nm, the positive component of the TR-SSHG signal must originate from resonance with a transition to a higher electronic state ($S_n \leftarrow S_1$). The intensity of the excited-state contribution in TR-SSHG profiles follows the intensity distribution in the ESA band in the TA data, being the highest for 440 nm and decreasing towards 400 nm. As this positive feature almost disappears at the highest concentration, it could be associated with the dynamics of monomers. The dynamics measured at each concentration and at probe wavelengths < 500 nm were analysed globally using the convolution of a Gaussian function representing the IRF

and the sum of three exponential functions, whereas the dynamics measured at 500 nm were analysed individually and required only two exponentials (**Table 4.2** and **Figure 4.14**).

		Concentration		
Tensor element	λ_{probe} / nm	0.1 mM	1 mM	10 mM
$\chi^{(2)}_{xxz}$	< 500	τ_1 = 1.0 ps τ_2 = 3.5 ps τ_3 =160 ps	τ_1 = 0.9 ps τ_2 = 2.5 ps τ_3 = 150 ps	τ_1 = 1.0 ps τ_3 = 160 ps
$\chi^{(2)}_{xxz}$	500		τ_1 = 5.1 ps τ_2 = 95 ps	τ_1 = 3.8 ps τ_2 = 140 ps
$\chi^{(2)}_{zxx}$	400 - 500	τ_1 = 14 ps τ_2 = 65 ps	τ_1 = 8 ps τ_2 = 100 ps	τ_1 = 4 ps τ_2 = 90 ps

Table 4.2. The time constants obtained from the global analysis of TR-SSHG profiles measured for $\chi^{(2)}_{xxz}$ and $\chi^{(2)}_{zxx}$ at different probe wavelengths, upon excitation at 530 nm, for R6G concentrations of 0.1 mM, 1 mM, and 10 mM at the dodecane/water interface. The corresponding amplitudes are shown in **Figure 4.14.**

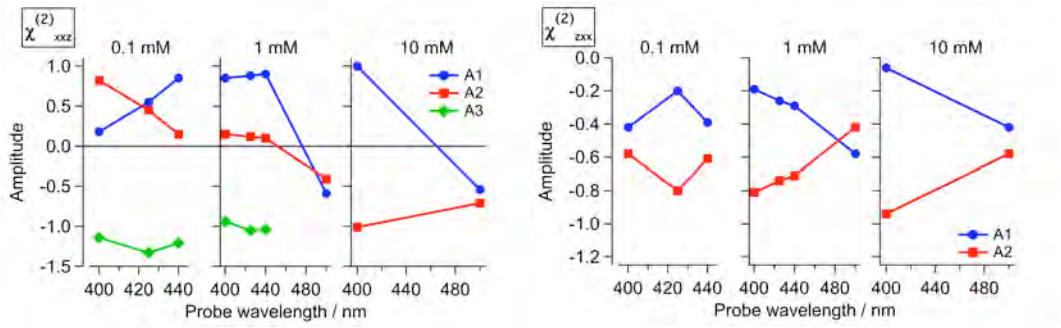

Figure 4.14. Amplitudes obtained from the global analysis of TR-SSHG profiles measured for $\chi^{(2)}_{xxz}$ and $\chi^{(2)}_{zxx}$ at different probe wavelengths, upon excitation at 530 nm, for R6G concentrations of 0.1 mM, 1 mM, and 10 mM at the dodecane/water interface.

At 500 nm, where the dynamics contain only the ground-state contribution, the long component (τ_2 = 95-140 ps) is similar to the TA component assigned to aggregates dynamics, and therefore interpreted alike. The short component (τ_1 = 4-5 ps) is

associated with the monomers dynamics and decreases with concentration. Such short lifetime of the monomers, compared to a few nanoseconds in bulk water at low R6G concentrations and few hundreds of picoseconds at high concentrations, probably originates from the fact that at the interface the R6G molecules adsorb so efficiently that the surface concentration is much higher than that in bulk water. Taking into account an increasing efficiency of the energy transfer from the monomers to the aggregates, the deactivation of the monomer at extremely high concentrations, such as the concentration of the R6G interfacial adsorbents, can take place in just a few picoseconds. For example, Penzkofer et al. found out that the fluorescence lifetime of R6G in methanol, concentrated up to 600 mM, is as short as ~1.5 ps.[120]

Two similar time constants were obtained with the dynamics recorded at shorter wavelengths, i.e. < 500 nm, as well as an additional ultrafast one (~1 ps). As this latter component is clearly associated with the decay of the positive excited-state feature, it may be due to vibrational relaxation that takes place on this timescale. Femtosecond time-resolved fluorescence also revealed a rising component of 0.9 ps at an emission wavelength of 550 nm (**Figure 4.15**), which would further support this hypothesis.[129] The dynamics at 10 mM/400 nm could not be reproduced using the convolution of a Gaussian function and exponentials and was therefore only partially fitted with a sum of exponentials, which might cause the absence of τ_2 component in that case.

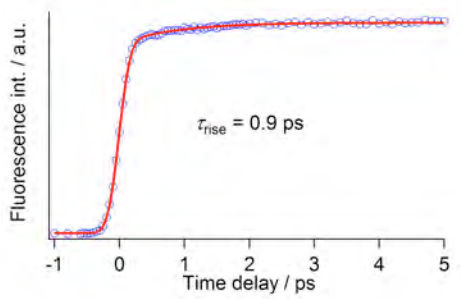

Figure 4.15. Early fluorescence time profile of R6G 0.1 mM in bulk water.

In the case when $\chi^{(2)}_{zxx}$ tensor element is probed, the TR-SSHG profiles of R6G show a prompt depletion at time zero followed by a recovery of their intensity, which we attributed to the ground-state recovery (GSR) of R6G while the resonant enhancement is dominated by the two-photon $S_2 \leftarrow S_0$ transition or one-photon $S_1 \leftarrow S_0$ transition. Interestingly, changing the probe wavelength does not dramatically influence the observed time profiles of R6G at the interface for this polarization configuration. The

absence of the excited-state monomer contribution implies that the excited-state dynamics is governed by the contribution of R6G aggregates. The dynamics for each concentration were analysed globally and could be well reproduced with two exponentials (τ_1 = 4-14 ps and τ_2 = 65-100 ps, **Table 4.2** and **Figure 4.14**). The short component was ascribed to the GSR of monomers and the long one – to the GSR of aggregates. Similarly to the case of $\chi^{(2)}_{xxz}$, τ_1 shortens with the concentration, going from 14 ps at 0.1 mM to 4 ps at 10 mM. However, no ultrafast component was observed in the excited-state dynamics measured with $\chi^{(2)}_{zxx}$.

TR-SSHG profiles recorded at 400 nm for R6G in a wide range of concentrations at the dodecane/water interface, with the $\chi^{(2)}_{zxx}$ and $\chi^{(2)}_{xxz}$ tensor elements, upon excitation at 530 nm and 500 nm, are shown in **Figure 4.16.**

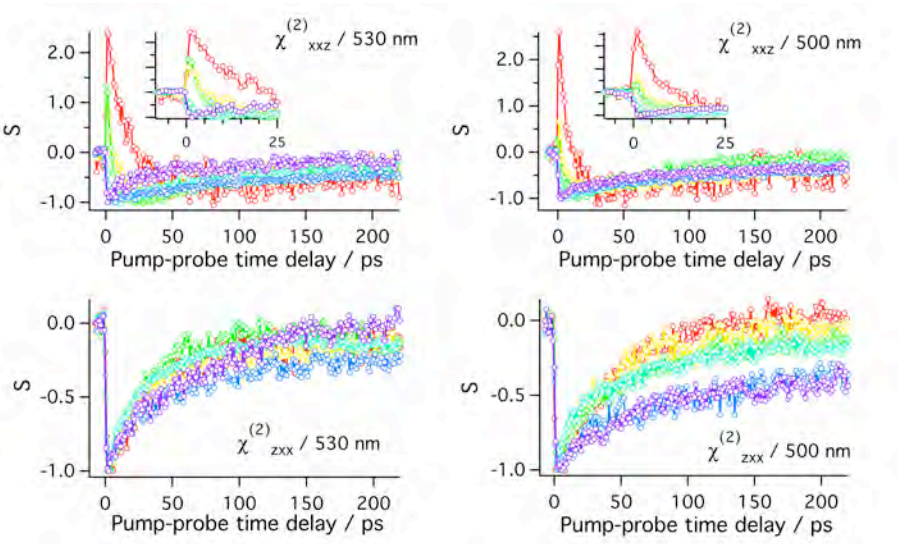

Figure 4.16. TR-SSHG profiles of R6G measured at 400 nm, with either the $\chi^{(2)}_{zxx}$ or $\chi^{(2)}_{xxz}$ tensor elements, upon excitation at 530 nm and 500 nm, for the different bulk concentrations of R6G (o 0.05 mM, o 0.1 mM, o 0.5 mM, o 1 mM, o 5 mM, o 10 mM) at the dodecane/water interface. Insets in the top graphs show the corresponding graphs on the 25 ps time scale. For better comparison the positive signal components of $\chi^{(2)}_{xxz}$ were not normalized to 1 at their maximum photoinduced change.

As has been described in the previous section, the TR-SSHG profiles of R6G measured with $\chi^{(2)}_{xxz}$ exhibit a contribution of the excited-state monomer at the beginning of the dynamics, which corresponds to the resonance with the $S_n \leftarrow S_1$

transition. This feature clearly vanishes upon increasing the R6G concentrations, which means that the ground-state contribution of aggregates starts to prevail over the contribution of the excited-state monomers: at high concentrations the observed dynamics at the interface is governed by the GSR of aggregates as monomers are quenched and no longer contribute to the molecular relaxation. This effect is more pronounced upon excitation at 500 nm compared to 530 nm, resulting in the faster vanishing of the excited-state monomer feature as aggregates are predominantly excited at 500 nm.

TR-SSHG profiles of R6G measured with $\chi^{(2)}_{zxx}$, show the GSR of R6G, as has been discussed in the previous section, and additionally exhibit a trend in the excited-state dynamics upon increasing the concentration of the molecules at the interface. This trend is especially pronounced upon excitation at 500 nm: the excited-state dynamics dominated by the relaxation of R6G aggregates significantly slows down at higher concentrations.

Summary. It was demonstrated that in bulk water the excited-state dynamics of R6G consisted of the contributions from the monomers and aggregates with lifetimes from a few nanoseconds to a few hundred picoseconds upon increasing the bulk concentration and ~70 ps, respectively. The decrease of R6G monomer lifetime upon increasing its concentration was ascribed to self-quenching through Förster-type energy transfer from monomers to aggregates.

At the dodecane/water interface, by probing different second-order nonlinear susceptibility tensor elements, $\chi^{(2)}_{xxz}$ and $\chi^{(2)}_{zxx}$, different contributions into the excited-state dynamics of R6G could be distinguished. When probing $\chi^{(2)}_{xxz}$, the contribution of the short-lived excited-state monomer, which was more or less pronounced depending on the resonance conditions, was observed. The very short lifetime of R6G monomers (a few ps), compared to the ones in bulk at the same bulk concentrations (a few ns to a few hundreds of ps upon increasing the concentration), was explained by the fact that the local interfacial concentration is higher than the bulk one due to the extremely high adsorption of the R6G molecules at the interface favoring, thus, a very efficient quenching of the R6G monomers.

Probing $\chi^{(2)}_{zxx}$ did not reveal the contribution from the excited-state monomer. In this case, the interfacial excited-state dynamics was dominated by the ground-state recovery of R6G aggregates, with the deactivation lifetime similar to that in bulk water.

4.2. Access to the environmental properties at liquid interfaces

4.2.1. Hydrogen bonding

Over the past several years, eosin B (EB, **Figure 4.17**), a dye from the xanthene family, has been successfully used in SSHG studies of acid-base equilibrium,[130] and orientational relaxation[108] at air/water interfaces. EB appears to be a convenient probe molecule for studying aqueous interfaces because it is water-soluble and its absorption spectrum allows its use in typical TR-SSHG setups based on femtosecond Ti:Sapphire amplifiers. Despite this, very little is known about its photophysics in bulk solutions and the available data are contradictory. For instance, various sources report a S_1-state lifetime in alcohols going from 90 ps in methanol,[131] up to 4.5 and 5.3 ns in ethanol.[132-134] However, the lifetimes of the closely related eosin Y (EY, **Figure 4.17**) reported in literature are more consistent and vary from 1.1 ns in water to 3-4.5 ns in organic solvents.[132, 135-137]

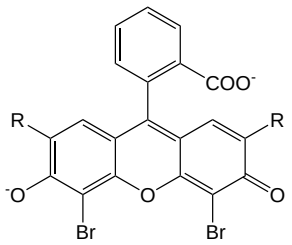

Eosin B (EB): R = NO_2
Eosin Y (RY): R = Br

Figure 4.17. Eosin B and eosin Y in their double anion form.

In order to clarify the excited-state dynamics of EB and understand its photophysics, which would greatly facilitate its application in TR-SSHG studies of interfaces, a series of femtosecond transient absorption measurements of both EB and EY in solution was carried out. It will be shown that EB is practically nonfluorescent in water and alcohols, in agreement with the work of Reindl and Penzkofer,[131] whereas EY is strongly fluorescent in all solvents investigated. The two dyes differ only by the presence of two nitro groups in EB that replace two of the four bromine atoms of EY. Therefore, the efficient radiationless deactivation of EB must be a direct consequence of this substitution. The present work reveals that the very short excited-state lifetime of EB in water and alcohols is

due to the occurrence of hydrogen-bond assisted nonradiative deactivation.[138] As a consequence, EB appears to be a valuable dynamic probe of the hydrogen-bonding properties in bulk environments and at liquid interfaces.

The study of the optical properties of the eosins is complicated by the existence of various forms in solutions: doubly charged anion (**Figure 4.17**), single anion (with the carboxyl group protonated), neutral and lactonic.[130] In aqueous solutions, the pKa of the first and second dissociation steps are equal to, respectively, 2.2 and 3.7 for EB,[130] and 3.25 and 3.80 for EY.[139] Therefore, the pH of the aqueous solutions was kept above 8 to ensure that only the double-anion is present. This is confirmed by the absorption spectra measured in water at various pH, which do not change any more above a pH of 6 (**Figure 4.18**).

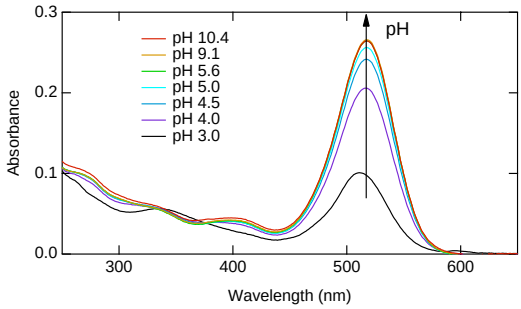

Figure 4.18. Steady-state absorption spectra of EB ($7x10^{-6}$ M) at various pH.

The absorption and fluorescence spectra of EB and EY in aqueous (at pH > 8) and MeOH solutions are shown in **Figure 4.19**, whereas the fluorescence quantum yields determined for EB in various solvents are listed in **Table 4.3**. The absorption spectra of both compounds are very similar and do not change significantly when going from water to MeOH. In longer alcohols, they are slightly red-shifted but otherwise do not differ from those in MeOH. This confirms that the dominating form of the molecules in alcoholic solutions is the double anion, the same as in basic aqueous solution.

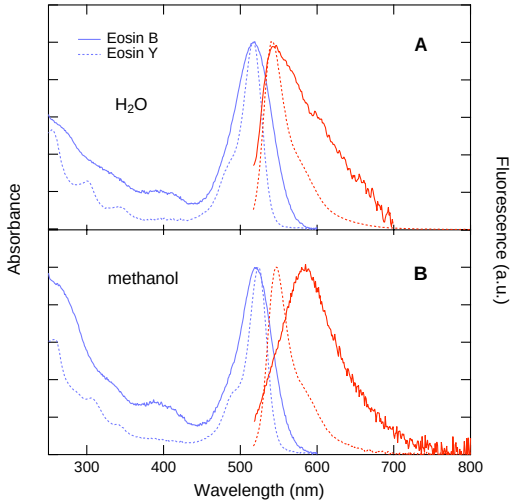

Figure 4.19. Steady-state absorption and fluorescence spectra of EB (solid line) and EY (dashed line) in (A) water and (B) MeOH.

The emission spectrum of EY is mirror image of its absorption spectrum and the Stokes shift is relatively small, about 900 cm^{-1}. This is not the case with EB, whose emission spectrum is significantly broader and exhibits a bigger Stokes shift in MeOH (~2200 cm^{-1}). Surprisingly, the Stokes shift of EB in water is smaller than in MeOH. This stems from the extremely short fluorescence lifetime of EB in water which, as it will be shown below, amounts to a few picoseconds and accounts for the very small fluorescence quantum yield (**Table 4.3**). This lifetime is comparable to the time scale of solvent relaxation, meaning that fluorescence is due to partially nonequilibrated, not fully solvated molecules. As a consequence, the average emission is shifted to higher energies compared to MeOH, where the fluorescence lifetime is much longer.

Solvent	Φ_{fl}
water	$4.5 \cdot 10^{-4}$
methanol	$7.5 \cdot 10^{-3}$
butanol	$4.5 \cdot 10^{-2}$
decanol	$6.6 \cdot 10^{-2}$
acetonitrile	$3.6 \cdot 10^{-2}$

Table 4.3. Fluorescence Quantum Yield of EB Measured in Various Solvents

The spectral differences between the dyes indicate that, contrary to EY, the emitting state of EB somewhat differs from the initially populated state. This can be attributed to the presence of the nitro groups in EB, which are known to have strong electron-withdrawing property. Therefore, the S_1 state of EB can be expected to have a substantial charge-transfer character. Because of this, the optical population of the Franck-Condon excited state must be followed by some ultrafast structural relaxation of high frequency modes. TD-DFT calculations performed on the dianionic form of EB (see **Section 6.3** for details) confirm the charge-transfer character of the first electronic transition. They predict this transition to be at 2.5 eV and to be associated with a one electron HOMO-LUMO transition which, as illustrated in **Figure 4.20**, involves a substantial increase of the electronic density on the nitro groups.

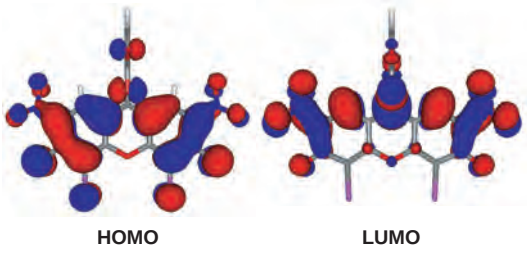

Figure 4.20. Frontier molecular orbitals of EB drawn at the 0.02 a.u. level.

Additionally, the nitro groups can act as hydrogen-bond acceptors,[140-142] and, because of the higher electronic density in the S_1 state, H-bonds with surrounding solvent molecules should be stronger in the excited than in the ground state. The presence of hydrogen bonds between EB and solvent molecules could account for the broader emission spectrum in protic than in aprotic solvents as shown by the comparison of the fluorescence spectra recorded in MeOH and ACN (**Figure 4.21A**).

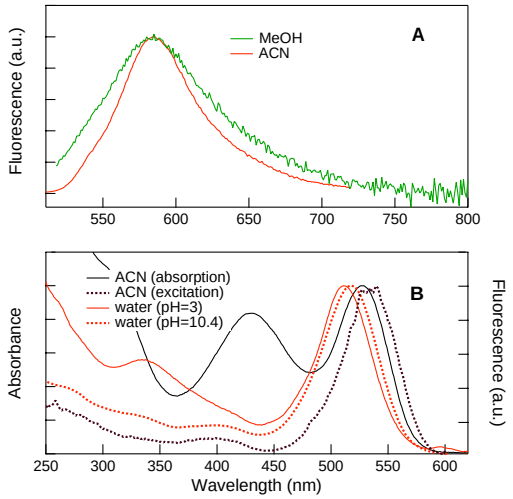

Figure 4.21. (A) Fluorescence spectra of EB in MeOH and ACN and (B) absorption spectra of EB in ACN, water at pH = 3 and 10, and fluorescence excitation spectrum of EB in ACN.

The absorption spectrum of EB in ACN differs significantly from that in protic solvents such as water and alcohols (**Figure 4.21B**). In particular, it exhibits an intense band around 425 nm that has to be attributed to a second, nonemissive, form of the dye, because it is not present in the fluorescence excitation spectrum recorded at 600 nm (**Figure 4.21B**). The latter closely resembles the absorption spectrum in water at high pH, whereas it differs from the absorption spectrum recorded in water at low pH. This indicates that in ACN, the doubly charged anion form of EB coexists with another one, most likely the neutral one, for the absorption spectra of lactones are typically located below 400 nm. Despite this coexistence, the properties of the doubly charged anion form of EB in ACN can be studied by time-resolved techniques because the absorption spectra of charged and neutral forms are well separated and, consequently, a given form can be selectively excited. Still, the presence of singly charged anions in addition to the doubly charged form cannot be entirely excluded, but their concentration must be low, because the band around 350 nm, intense in aqueous solution at pH=3, where this form predominates, cannot be seen in ACN.

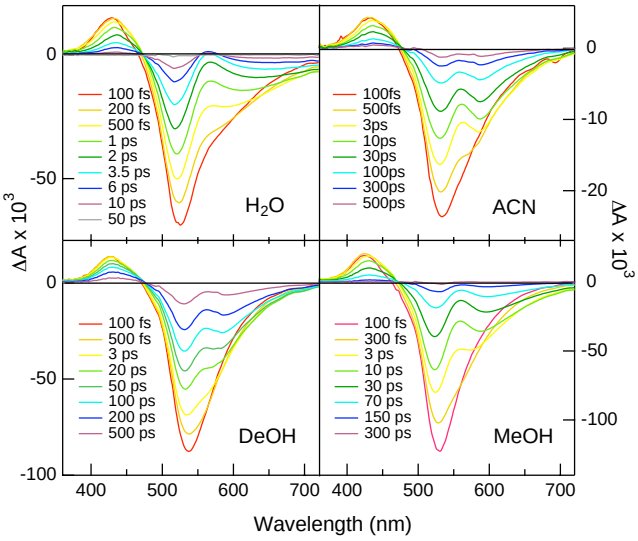

Figure 4.22. TA spectra recorded at different time delays after 520 nm excitation of EB in various solvents.

TA spectra were recorded upon 520 nm excitation of EB in water, MeOH, BuOH, DeOH and ACN (**Figure 4.22**, the data in BuOH are not shown as they are very similar to those in DeOH). The measurements have been carried out at $9 \cdot 10^{-5}$ M of EB concentration, but, as the spectral dynamics in water is the same at 10^{-5} M, one can conclude that aggregation does not play a significant role at these concentrations. The TA spectra consist of three main bands: one extending from 360 to 470 nm due to excited-state absorption (ESA), a bleaching band coinciding with the $S_1 \leftarrow S_0$ absorption and a stimulated emission (SE) band, red-shifted with respect to the bleaching. In water and MeOH, the transient signals decay entirely within the temporal window of the experiment (500 ps), whereas the temporal evolution of the spectra in BuOH, DeOH, and ACN, although qualitatively very similar to that in MeOH, is slower and the transient signals do not vanish at the maximum time delay.

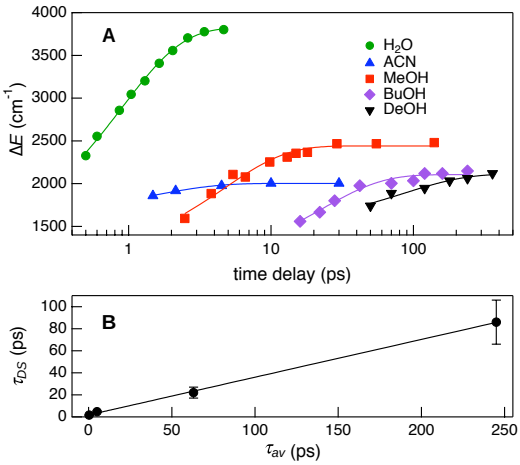

Figure 4.23. (A) Energy difference between the maxima of the SE and $S_1 \leftarrow S_0$ absorption bands of EB as a function of the time delay in various solvents. (B) Characteristic time τ_{DS} of the dynamic Stokes shift of EB vs. the average correlation time of the solvents, τ_{av}.

Still, one can safely assume that in all solvents, the whole optically excited population relaxes directly to the ground state. Therefore, the fraction of molecules populating the triplet state is negligibly small.

The magnitude of the temporal shift of the SE band depends on solvent polarity: the more polar the solvent, the more red-shifted the emission at longer delays. The time dependence of the position of the SE band maximum can be well reproduced with a monoexponential function (**Figure 4.23A**).

Solvent	τ_1 (ps)	τ_2 (ps)	τ_3 (ps)	τ_{DS} (ps)	τ_{AV} (ps)
H_2O (3 exp.)	0.09[a]	1.0	4.3	0.89	
H_2O (2 exp.)	-	1.1	4.4		
D_2O (2 exp.)	-	1.6	7.6	-	
methanol	0.64	8.5	54	4.7	5
butanol	1.2	34	210	22	63
decanol	2.1	49	310	86	245
acetonitrile	2.6	23	280	1.6	0.26

Table 4.4. Time Constants Obtained from a Multi-Exponential Analysis of the Transient Absorption Data Recorded with EB in Various Solvents ($\tau_1 - \tau_3$), Characteristic Time of the Dynamic Stokes Shift (τ_{DS}), and Average Correlation Time of the Solvent (τ_{av}).[143]

[a] Shorter than the width of the response function of the TA setup.

The time constant of this shift is directly proportional to the average relaxation time of the solvent[143] (**Figure 4.23B** and **Table 4.4**), therefore this effect can be almost entirely attributed to the dynamic Stokes shift of the SE resulting from solvent relaxation. In contrast, the SE band of EY in water and alcohols that can be seen as a shoulder between 560 and 620 nm, lies much closer to the bleaching band and does not shift in time **(Figure 4.24**).

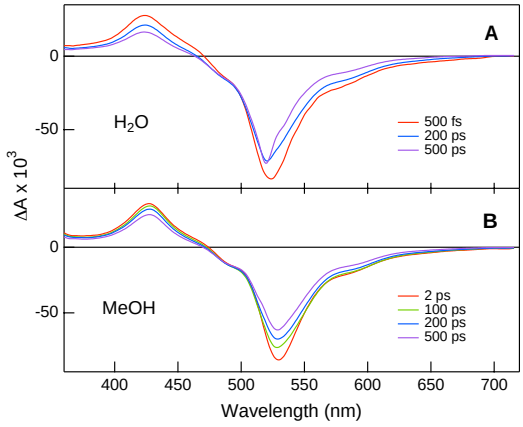

Figure 4.24. Transient absorption spectra recorded at various time delays after excitation at 520 nm of EY in water (A) and MeOH (B).

This indicates that the emitting state of EB is much more polar than that of EY and supports the hypothesis of its charge-transfer character introduced by the nitro substituents. The TA spectra recorded with EY in both water and MeOH exhibit very little spectral evolution within the temporal window of experiment, in agreement with a nanosecond excited-state lifetime.[135, 137, 144]

For EB, no other spectral evolution but the decay of the TA bands and the shift of the SE can be seen. In particular, there is no rise of any signals that could be attributed to build-up of the product of an excited-state reaction.

The excited-state lifetime of EB dramatically depends on the solvent: this dye is practically nonfluorescent in water, whereas its fluorescence can be clearly seen in ACN, BuOH, and DeOH when excited at 520 nm. In order to analyze quantitatively the dependence of the excited-state lifetime on solvent properties, TA profiles at three different wavelengths have been analyzed globally with multiexponential functions. The selected time profiles reflect the evolution of the signal at the maximum of the ESA band, at the maximum of the bleaching and close to the maximum of SE band, so that the influence of the shift of the latter is minimized. The three time constants required to satisfactorily reproduce the data are listed in **Table 4.4** and the data together with the best-fit curves are presented in **Figure 4.25.**

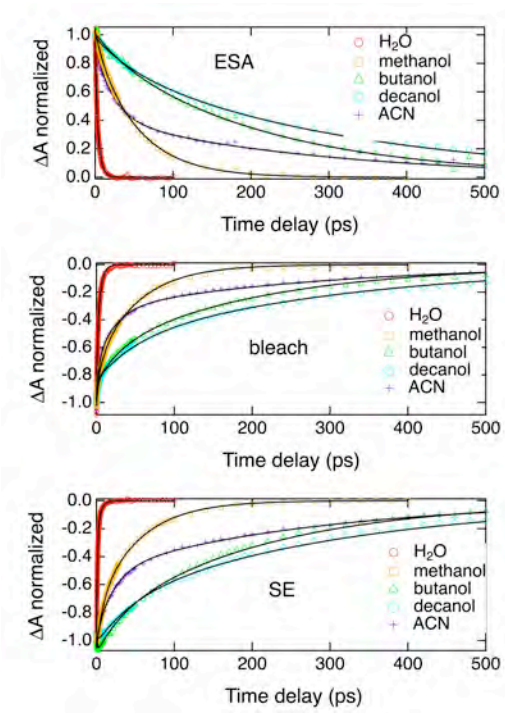

Figure 4.25. Transient absorption profiles at the excited state absorption (ESA) band at 435 nm, bleaching band at 532 nm, and stimulated emission (ES) band at 588 nm, measured with eosin B in various solvents. The solid lines are the best-fits of a three-exponential function.

It is not possible to directly assign these time constants to a population transfer between different species or even to specific processes, like intramolecular vibrational redistribution or solvent relaxation, because the spectral evolution is dominated by nonexponential dynamics resulting from the dynamic Stokes shift. In this situation, the multiexponential analysis of the time profiles should be seen only as a numerical procedure performed to quantitatively describe the rate of the processes following optical excitation. Therefore, all three values have to be analyzed together and considered as a representation of the whole deactivation pathway, which includes vibrational and solvent relaxation and finally the excited-state decay. Only in an approximation, the two shorter time constants may be attributed to vibrational and solvent relaxation, whereas the longest time can be identified with the excited-state lifetime. The latter assignment is also reinforced by comparison with the fluorescence quantum yields (**Table 4.3**). Assuming that $\Phi_{fl} = k_{rad} \cdot \tau_3$ gives a rate constant of radiative deactivation, k_{rad}, ranging between 1 and $2 \cdot 10^8$ s^{-1}, depending on the solvent.

These time constants correlate with neither solvent viscosity nor polarity, but they correlate well with the strength of the solvent as a hydrogen-bond donor measured in both, the Kamlet-Taft, α,[145] and the Catalan-Diaz solvent acidity, SA,[146, 147] scales (**Figure 4.26**).

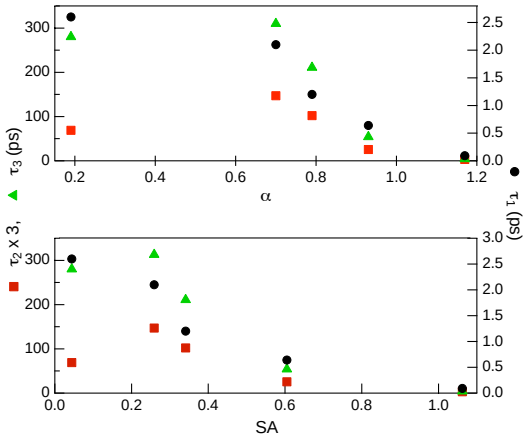

Figure 4.26. Time constants obtained from the analysis of the transient absorption data of EB vs. (A) the Kamlet-Taft, α,[145] and (B) the Catalan-Diaz, SA,[146, 147] parameters of the solvents (τ_2 was multiplied by 3 for a better visualization).

The correlation breaks down only with τ_2 in ACN. However, one has to remember that, in this case, the neutral form of EB might contribute to the TA signals. Besides this, the time profiles recorded in water and alcohols have a significant nonexponential component due to the dynamic Stokes shift of the SE band, whereas

this effect is much weaker in ACN. The correlation between the time constants obtained from the TA data and both the α and SA parameters points to a key role of the hydrogen bonds in the excited-state deactivation.

The strong shortening of the excited-state lifetime of EB in protic solvents points to the occurrence of hydrogen-bond assisted nonradiatiave deactivation.[136, 148-154] The nitro groups of EB that are good hydrogen-bond acceptors enable this process.[140-142, 155, 156] In order to further confirm this hypothesis, TA measurements were carried out in perdeuterated water. As expected for the hydrogen-bond assisted deactivation mechanism, the dynamics in D_2O was slower than in H_2O (**Figure 4.27**) by approximately a factor 1.5 (**Table 4.4**).

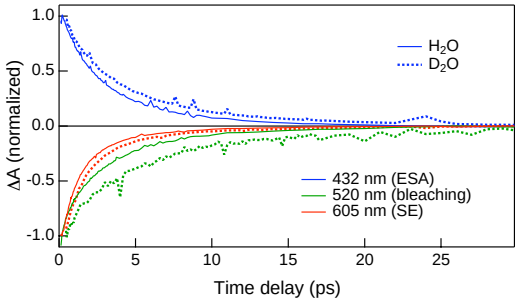

Figure 4.27. Transient absorption profiles measured with EB in H_2O and D_2O in the spectral regions of excited-state absorption (ESA), bleaching and stimulated emission (SE).

The following picture for the excited-state deactivation of EB in water and alcohols is proposed: the strength of the hydrogen bonds between the nitro groups and hydroxyl groups of the solvent increases upon optical excitation due to the charge transfer character of the transition and the rise of electron density on the nitro substituents; this in turn leads to an increase of the coupling with the solvent, enhancing the nonradiative deactivation. The exact mechanism of the hydrogen-bond assisted nonradiative deactivation is not totally understood. It could be thought in terms of an excited-state intermolecular proton transfer with the solvent molecules, followed by back proton transfer to the ground state. The absence of an intermediate in the TA spectra could be due to an incomplete proton transfer or to a back transfer that is much faster than the forward transfer. Therefore, the excited-state lifetime of EB can be considered as a measure of the hydrogen-bonding properties of the environment. A scale of hydrogen-bond strength, analogical to the SA scale, could be based on either the fluorescence quantum yield or the excited-state lifetime of EB. Other xanthene dyes, namely rose Bengal (RB) and fluorescein, have already been demonstrated as probes for hydrogen bonds with the solvent.[157, 158] In both dyes, hydrogen bonding

with the solvent molecules results in a stabilization of the electronic states. This stabilization energy, whose magnitude depends on the nature of the excited state, leads to a change of the energy gap between these states, affecting the $S_1 \rightarrow T_1$ intersystem crossing rate constant of RB,[157] and leading to a strong solvatochromism of the absorption band of fluorescein.[158] Therefore, either the fluorescence lifetime of RB or the absorption band maximum of fluorescein can be used as a scale of the hydrogen bond ability of the solvent. EB differs considerably from the above dyes when applied as a hydrogen bonds probe. Its absorption spectrum depends weakly on the environment and only its excited-state lifetime changes with the solvent. Furthermore, its triplet state is not populated during the deactivation. Finally, the excited-state lifetime of EB (4.4 ps in water and 280 ps in ACN) is much shorter than that of RB (120 ps in water and 2.4 ns in ACN) and is also more sensitive to the hydrogen bond ability of the solvent, the ACN/water lifetime ratio being equal to 60 for EB and 20 for RB.

All of these features make EB particularly suitable for studying hydrogen bonds at interfaces by TR-SSHG. In this technique, the population dynamics of various states of the probe dye is observed and the absence of triplet state population in the deactivation pathway of EB makes the interpretation of the data easier and more reliable. In turn, the weak influence of the solvent on the absorption spectrum of EB eliminates the changes of intensity of the generated second harmonic light, which strongly depends on resonances with electronic transitions of the dye. Furthermore, the time scale of the excited-state lifetimes matches very well the standard specifications of TR-SSHG setups, which can readily reach subpicosecond temporal resolution.

The further results demonstrate how EB can be applied as hydrogen bond probe in interfacial experiments.[159]

Figure 4.28 shows polarization dependent (PD)-SSHG traces measured with various bulk concentrations of EB at the dodecane/water interface. For these measurements, either the s- or p-polarization components of the SH signal were detected and the circularly polarized pump beam was either blocked or open. In the latter case, the time delay between the excitation and probe pulses was set to ~1 ps. It can be clearly seen that the shape of the PD-SSHG signal strongly depends upon the dye concentration; at high concentrations, the maximum intensity of the p-SH signal is

reached with the s-probe (**Figure 4.28A**), whereas at low concentrations, it is obtained with the p-probe (**Figure 4.28C**). At intermediate concentrations, two maxima can be seen (**Figure 4.28B**), and the dependence of the SH intensity on the polarization angle gradually changes its character with an increasing concentration. This indicates that the relative magnitude of the three non-vanishing elements ($\chi^{(2)}_{xxz}$, $\chi^{(2)}_{zxx}$ and $\chi^{(2)}_{zzz}$) of the effective second-order nonlinear susceptibility tensor, $\vec{\chi}^{(2)}$, depends upon the EB concentration, because the SH intensity is given by[160, 161]

$$I_p = B\left|(a_2\chi^{(2)}_{xxz} + a_3\chi^{(2)}_{zxx} + a_4\chi^{(2)}_{zzz})\cos^2\gamma + a_5\chi^{(2)}_{zxx}\sin^2\gamma\right|^2 I^2(\omega) \qquad (4.1)$$

$$I_s = B\left|(a_1\chi^{(2)}_{xxz}\sin^2 2\gamma\right|^2 I^2(\omega) \qquad (4.2)$$

where I_p and I_s are the intensities of the p- and s-SH signal components, respectively, B and a_i are coefficients dependent on the angle of incidence and properties of the media constituting the interface, $I(\omega)$ is the incident light intensity, and γ is the angle between the direction of the probe beam polarization and the plane of incidence, so that $\gamma = 0$ for p-probe.

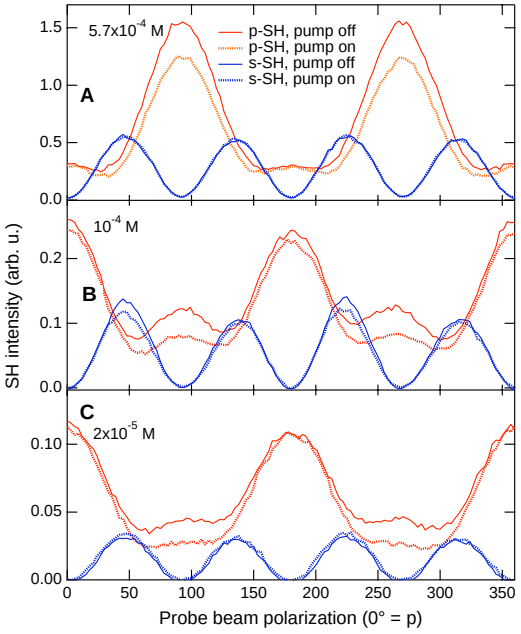

Figure 4.28. Dependence of the second harmonic intensity on the polarization of the probe beam measured with EB at the dodecane/water interface, without and with the pump beam at a small positive time delay, at different bulk EB concentrations (**A:** $5.7\cdot10^{-4}$ M; **B:** 10^{-4} M; and **C:** $2\cdot10^{-5}$ M).

The above-described effect can be attributed to the formation of EB aggregates at the interface. Xanthene dyes are generally prone to aggregation,[162] and it has been shown

that organic molecules at air/water or alkane/water interfaces tend to strongly aggregate, with the probability increasing with the bulk concentration of the dye.[23, 115, 116, 118] The concentration dependence of the PD-SSHG traces indicates that either the interfacial orientation of EB changes upon aggregation or the shape of the hyperpolarizability tensor, $\alpha^{(2)}$, of the aggregate and the monomer differs substantially. At a given concentration, both forms contribute to the SH signal and the relative contribution of aggregates increases with the dye concentration, thus changing the effective nonlinear susceptibility tensor.

A displacement of the equilibrium between the various oxidation states of EB because of pH changes could also be proposed, because this dye can exist in four different forms in aqueous solutions: double anion (**Figure 4.17**), single anion, neutral, and colorless lactone forms.[130] It has been already shown that, at a bulk pH above 6, practically only one form, the double anion, is present (**Figure 4.18**). To ensure that this conclusion can also be drawn for the alkane/water interfaces, it was checked that the PD-SSHG traces had the same shape at pH values ranging from 6 to 9. Because all of the data were recorded at a pH of ~8, the hypothesis that the changes of the PD-SSHG curves with the EB concentration result from a variation of the oxidation state can be ruled out.

The results of the PD-SSHG measurements with various dye concentrations are consistent with previous experiments carried out at the air/water interface with [EB] = $3 \cdot 10^{-5}$ M, where the intensity of the p-SH signal with s-probe was very small at pH > 6 and increased significantly at lower pH.[130] This observation was interpreted as a negligible contribution of the doubly anionic form of EB to the SSHG resonance enhancement. Nevertheless, this conclusion seems questionable, because in the experiments described here, the SH signal is clearly enhanced by EB in its double anion form. Our PD-SSHG measurements indicate that it is rather the orientation of EB at the interface that makes the p-SH signal with s-probe very weak at low bulk concentrations.

Figure 4.28 also reveals that optical excitation leads to a decrease of the p-SH intensity, with this change being the largest with s-probe and being almost absent with p-probe. On the other hand, the s-SH intensity is practically unaffected by optical excitation, independently of the polarization of the probe beam. This implies that the $\chi^{(2)}_{xxz}$ element of the effective second-order susceptibility tensor of the system does not

change upon excitation of EB, whereas $\chi^{(2)}_{zxx}$ and $\chi^{(2)}_{zzz}$ change in such a way that $\Delta[a_3\chi^{(2)}_{zxx} + a_4\chi^{(2)}_{zzz}] \approx 0$ (Eq. 4.1). Such a behavior of the $\chi^{(2)}_{ijk}$ tensor elements upon optical excitation has previously been observed with EB at the air/water interface[108] and was interpreted in terms of purely rotational dynamics of the molecules in the saturation regime, where population dynamics cannot be seen. In the present case, however, the experimental conditions are different and the change of the SH intensity because of optical excitation cannot be attributed to orientational effects only. First, the wavelengths of the fundamental and SH beams are relatively remote from any electronic resonances, whereas in the experiments described in ref,[108] the probe beam was resonant with the $S_1 \leftarrow S_0$ transition. Second, the energies of both pump and probe pulses used here are orders of magnitude lower, preventing saturation of the electronic transitions. This difference is clearly visible in the TR-SSHG data; the time profiles of the SH intensity presented in ref[108] are independent of the EB concentration, whereas a strong acceleration of the dynamics with an increasing concentration is observed here. This is illustrated in **Figure 4.29**, which depicts p-polarized TR-SSHG profiles measured with s-probe and with circularly polarized pump pulses.

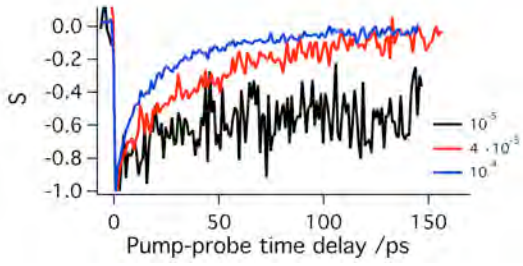

Figure 4.29. TR-SSHG profiles (p-SH and s-probe) measured at 400 nm, upon excitation at 515 nm, with various EB concentrations at the dodecane/water interface.

This concentration dependence again points to a significant role of aggregates at the interface. At the same time, it indicates that the decay of the TR-SSHG signal should be mainly attributed to population relaxation and not to orientational relaxation, even though it has been shown that the latter could, in some cases, contribute to more than 80% of the decay.[89] Nevertheless, if orientational relaxation were responsible for the observed TR-SSHG decays, the dynamics would slow down at higher dye concentrations, because the reorientational motion of aggregates should be slower as a result of its larger hydrodynamic volume compared to that of the monomers. This is obviously not the case here, and the observed dependence of the TR-SSHG decay time on the dye concentration can be well-accounted for in terms of electronic

relaxation of aggregates and monomers, because excited xanthene aggregates have been shown to undergo very efficient non-radiative deactivation.[121, 163] Aggregates may also reduce the excited-state lifetime of monomers through excitation energy-transfer quenching. However, it is difficult to determine whether the latter process is really operative at the interface. Because both monomers and aggregates probably contribute to the resonant enhancement of the SH intensity, the overall TR-SSHG signal decay should be faster at higher concentrations of aggregates, even if the latter do not quench the excited monomers.

There is still an additional effect that can be associated with interfacial aggregation; PD-SSHG and TR-SSHG curves recorded at the dodecane/water interface change slowly but significantly with time. For instance, the PD-SSHG traces measured with a fresh $2 \cdot 10^{-5}$ M EB sample have only maxima with p-probe. Several hours after sample preparation, small local maxima appear with s-probe, and 1 day later, these maxima predominate (**Figure 4.30A**). This variation of the PD-SSHG traces is accompanied by changes in the TR-SSHG dynamics; the decays become faster with the time elapsed after sample preparation (**Figure 4.30B**).

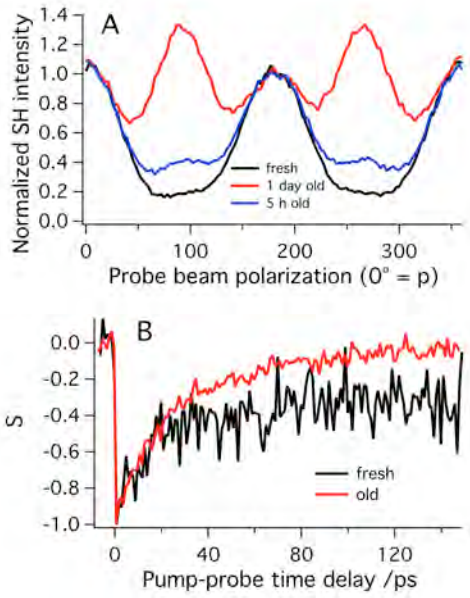

Figure 4.30. (A) Dependence of the p-SH intensity on the polarization of the probe beam measured at the dodecane/water interface with fresh, 5 h, and 1-day-old samples ([EB] = $2 \cdot 10^{-5}$ M) and (B) TR-SSHG profiles measured with fresh and 1-day-old samples (measured at 400 nm, upon excitation at 515 nm).

A similar effect is also observed at higher EB concentrations. At 10^{-4} M, the global maxima of the p-polarized PD-SSHG curves (**Figure 4.28B**) disappear entirely after 24 h and the PD-SSHG traces recorded with a 1-day-old sample look like those measured with a fresh and more concentrated EB sample (**Figure 4.28A**). In this case, however, the shortening of the decay time is much less pronounced but can still be

seen. In general, sample aging has the same effect on the measured SSHG data as an increase of the EB concentration. This leads us to conclude that, in both cases, the changes stem from an increasing concentration of aggregates at the interface, that aggregation at low dye concentration is very slow, and thus, that the equilibrium between aggregates and monomers needs several hours to be fully established at the interface. Because of this strong tendency of EB to aggregate at the dodecane/water interface, only TR-SSHG profiles recorded with fresh samples at low concentrations can be compared to the data measured in bulk solutions, where monomers are almost exclusively present. These conditions are very unfavorable for the interfacial measurements, because the SH signal has to be detected with s-probe, i.e., at a minimum of the PD-SSHG curves. Consequently, the intensity of the detected signal is very low (**Figure 4.28C**), and the noise of the TR-SSHG profiles is high (**Figure 4.29**).

In addition to the studies of EB at the dodecane/water interface, measurements at the decanol/water interface were also carried out. Decanol is weakly miscible with water, and the solubility of EB in this solvent is rather low. This, together with the high viscosity of decanol, slows down the diffusion of EB from the aqueous to decanol phases and makes such experiments possible. The replacement of an alkane by a long-chain alcohol has a strong impact on the observed SSHG signals. First, the SH intensity is much lower than with dodecane/water, so that measurements were practically impossible at EB concentrations below $5 \cdot 10^{-4}$ M. Despite this, the PD-SSHG traces at higher EB concentrations with decanol look similar to those with dodecane at low concentrations (**Figure 4.31A**).

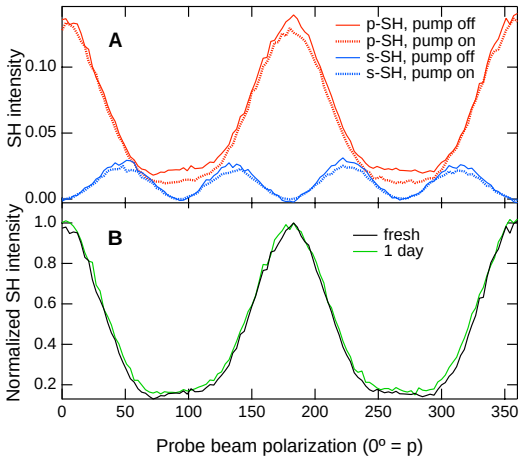

Figure 4.31. (A) Dependence of the second harmonic intensity on the polarization of the probe beam measured with EB ($5.7 \cdot 10^{-4}$ M) at the decanol/water interface, with and without the pump beam at a small positive delay, and (B) dependence of the p-SH intensity on the polarization of the probe beam at the decanol/water interface recorded with fresh and 1-day-old samples.

Second, in contrast to the dodecane/water interface, the decanol/water samples do not exhibit any influence of aging (**Figure 4.31B**). These differences indicate that EB does not aggregate easily at the decanol/water interface. This most likely stems from the higher water solubility of decanol compared to dodecane that should result in a more diffuse nature of the decanol/water interface compared to the dodecane/water interface. With decanol, the EB molecules diffusing from the aqueous phase toward the interface do not encounter the alkane barrier, where they are insoluble, but rather a region where water and decanol coexist. Most likely, EB is better solvated in this diffuse interfacial layer than at the "sharp" dodecane interface, and consequently, aggregation is much less favorable.

Figure 4.32 depicts a comparison of TR-SSHG profiles measured at both dodecane/water and decanol/water interfaces with transient absorption profiles recorded in bulk water and decanol at a wavelength reflecting the ground-state recovery of EB.[138] It is clear that, even with the significant contribution of aggregates at high EB concentrations, the decays measured at interfaces are all much slower than in bulk water.

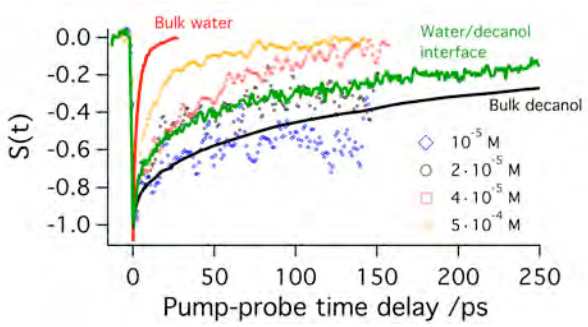

Figure 4.32. Comparison of time profiles recorded by TA with bulk water and decanol solutions of EB (solid lines) and TR-SSHG measured at 400 nm, upon excitation at 515 nm, at the dodecane/water interface at various EB concentrations (markers) and at the decanol/water interface (green line; [EB] = $5.7 \cdot 10^{-4}$ M).

The ultrafast excited-state deactivation of EB in water has been explained in terms of hydrogen-bond-assisted non-radiative deactivation.[138] Because of the charge-transfer character of the $S_1 \leftarrow S_0$ transition, the electron density at the nitro groups increases significantly upon excitation, strengthening the coupling with the surrounding protic solvent molecules. As a consequence, the S_1 lifetime of EB decreases significantly with an increasing hydrogen-bonding ability of the solvent.[138] Therefore, the slow excited-state dynamics measured by TR-SSHG leads us to conclude that EB is much less hydrogen-bonded with interfacial water than with bulk water. This interpretation agrees well with a previous study of EB at air/water interfaces,[108] where the

reorientational dynamics of EB was compared to that of R6G. Whereas the rotational time of EB at the air/water interface was found to be much faster than in bulk water, the opposite trend was reported for R6G.[124] This effect was explained by the authors of ref[108] by a strengthening of the hydrogen-bonding network between interfacial water molecules. Because of this, hydrogen bonding of a solute molecule to interfacial water is much less efficient. As a consequence, EB can rotate more easily at the interface than in bulk water, where it is strongly hydrogen-bonded. On the other hand, the larger rotational time of R6G at the interface was explained by an absence of a hydrogen bond with bulk water and by the more rigid, hydrogen-bonded, interfacial water structure.[108]

Hydration of small nonpolar organic molecules[164] and macromolecules, such as proteins,[165-167] is accompanied by a strengthening of water-water hydrogen bonds as a consequence of the weak water solubility of these solutes. Early vibrational SSFG studies of nonpolar liquid/water interfaces seemed to indicate an absence of hydrogen-bond strengthening at macroscopic interfaces, such as CCl_4/water or hexane/water, because the interfacial infrared spectra were lacking the features of strongly hydrogen-bonded water.[43, 168] Later, this conclusion has been contradicted by molecular dynamics simulations that revealed the existence of a large population of strongly hydrogen-bonded water molecules at the interface, in addition to monomer-like water molecules. Their orientation, however, parallel to the interfacial plane, makes these bonds undetectable by vibrational SSFG.[44, 169]

The ability of interfacial water to act as a strong hydrogen-bond donor has been confirmed by SSHG studies of *N*-methyl-*p*-methoxyaniline (NMMA) at the CCl_4/water interface.[170] The SSHG spectra of NMMA, whose electronic absorption spectrum is sensitive to the hydrogen-bonding properties of the environment, were typical for strong hydrogen bonds with water.

The results of our TR-SSHG studies with EB at alkane/water interfaces are rather surprising in view of the above experiments, revealing that a significant fraction of interfacial water molecules can be a donor of strong hydrogen bonds. At least two hypotheses can be proposed: (1) Hydrogen bonding of EB with interfacial water could be inhibited by the location of the nitrosubstituents, which are directly involved in the non-radiative deactivation of EB, in the nonpolar phase, even though this seems improbable considering the polar and anionic nature of the xanthene moiety. Still, if the hydrogen-bond-accepting strength of the carboxylic group prevails over the

affinity of the xanthene moiety for the polar phase, the molecules can be oriented in such a way that the nitro groups have limited contact with interfacial water; (2) EB might still be hydrogen-bonded with the interfacial water molecules, but the hydrogen-bond-assisted deactivation pathway might be inoperative at the interface. Although this nonradiative process has been reported with many different chromophores in protic solvents,[136, 149-151, 154, 171] its exact mechanism is still not totally understood. This process could be viewed as an excited-state intermolecular proton transfer with the solvent molecules, followed by back proton transfer to the ground state. Possibly the interfacial environment is such that this process is no longer efficient.

Unfortunately, our results do not provide any evidence in favor or against one of these hypotheses. Moreover, our PD-SSHG data do not provide easily accessible information on the orientation of EB molecules at the interfaces. This is due to the probe wavelength that does not coincide with an electronic transition of this dye. Because of this, no assumption on the components of the hyperpolarizability tensor can be performed. Previous measurements with EB at the air/water interface with a probe wavelength close to the maximum of the $S_1 \leftarrow S_0$ absorption band revealed that the angle between the z-axis of EB and the surface normal is about 25-30°.[108] Further studies are needed to determine the orientation of EB molecules at liquid/liquid interfaces. This could give insight into the mechanism behind the long excited-state lifetime of this dye at interfaces. The TR-SSHG profiles, *s(t)*, shown in **Figure 4.32**, can be analyzed with a biexponential function convolved with the instrument response function *f(t)* (Eq. 4.3), where τ_1 and τ_2 are associated with the initial decay and the constant amplitude, A_0, is related to the long-lived excited-state population.

$$s(t) = f(t) \otimes (A_0 + A_1 e^{-t/\tau_1} + A_2 e^{-t/\tau_2}) \qquad (4.3)$$

An unequivocal assignment of τ_1 and τ_2 is not possible, because the initial decay can result from various processes: (1) fast radiationless deactivation of excited EB aggregates, (2) excitation energy hopping, and/or (3) hydrogen-bond-assisted deactivation of a small population of EB molecules that are able to bind with water. The assignment of τ_1 and τ_2 is even more complicated because three decay constants are required to describe the excited-state dynamics of EB in bulk water solution.

Therefore, only the amplitude of the long-lived component, A_0, can be interpreted, but its associated time constant cannot be determined because of the limited temporal window of the experiment.

The magnitude of A_0 (with $A_0 + A_1 + A_2 = 1$) can be used to estimate the minimum fraction of EB molecules belonging to the long-lived population. Assuming that the initial decay is entirely due to hydrogen-bond-assisted deactivation, A_0 is equal to the long-lived fraction of the total number of adsorbed EB molecules. This fraction is even higher if processes 1 and/or 2 also contribute to the initial decay.

In fact, it can be shown that the initial decay partially results from processes 1 and 2. First, the plot of A_0 versus [EB] (**Figure 4.33A**) exhibits a steep decrease at low concentrations. This means that the limit at which only monomers are present at the interface is not reached at the lowest concentration used, because otherwise A_0 would be independent of the bulk EB concentration for small [EB]. Therefore, even at the lowest EB concentration used in the experiments, [EB] = 10^{-5} M, the aggregates are still present at the interface and contribute to the fast decay. Second, the TR-SSHG profiles measured with linearly polarized pump pulses are different, with light polarized parallel and perpendicular to the plane of incidence of the probe pulses, as illustrated in **Figure 4.33B** with [EB] = 10^{-4} M. This means that depolarization phenomena could to a certain extent contribute to the measured signal decays.[89] However, this polarization dependence takes place on too short a time scale (~10-20 ps) to be attributed to the reorientational motion of a molecule of the size of EB. For example, the reorientation time of a molecule of similar size in a polar but nonprotic solvent of the same viscosity as water is on the order of 140 ps.[172]

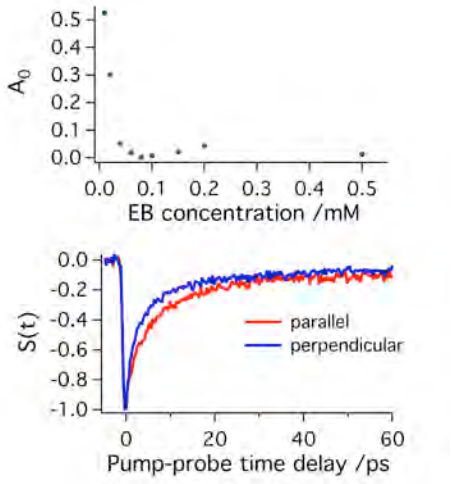

Figure 4.33. (A) EB concentration dependence of the long-lived component of the TR-SSHG profiles measured at the dodecane/water interface and (B) TR-SSHG profiles measured with EB at 400 nm, upon excitation at 515 nm, at the dodecane/water interface with pump pulses linearly polarized parallel and perpendicular to the plane of incidence of the probe pulses.

The interfacial EB concentration is not known, but considering that aggregation takes place, it can be expected to be substantially larger than the bulk concentration. Therefore, the pump polarization dependence of the TR-SSHG decay most likely originates from excitation energy hopping between interfacial EB molecules. In summary, the fraction of EB molecules adsorbed at the dodecane/water interface that are not affected by the mechanism of hydrogen-bond-assisted excited-state deactivation substantially exceeds a lower limit of 50% at [EB] = 10^{-5} M (**Figure 4.33A**). The decay of the TR-SSHG signal at the decanol/water interface is faster than in bulk decanol and resembles that recorded at the dodecane/water interface with [EB] = $2 \cdot 10^{-5}$ M. It is, however, difficult to determine whether this is due to a higher contribution of aggregates at the larger EB concentration used in this case ($5.7 \cdot 10^{-4}$ M) or rather a result from an intrinsic difference between the nonpolar liquid/water and polar liquid/water interfaces. Interfacial decanol molecules can be expected to be oriented with their hydroxyl groups toward the aqueous phase and to make hydrogen bonds with water. Further studies of interfaces between long-chain alcohols and water are needed before more definitive conclusions can be drawn.

Summary. This investigation showed that, although structurally very similar, EB and EY have substantially different photophysics and excited-state dynamics. This difference stems from the charge-transfer character of the S_1 state of EB introduced by the presence of two nitro groups instead of bromine atoms. The increase of electronic density on these groups upon optical excitation is accompanied by a strengthening of hydrogen bonds in protic solvents. This is at the origin of the hydrogen-bond assisted nonradiative deactivation of the excited state of EB, which decays within a few picoseconds in water and a few tens of picoseconds in methanol.
As S_1 state of EB undergoes hydrogen-bond-assisted non-radiative deactivation, it can be used as a dynamic probe for investigating hydrogen bonding at alkane/water and long-chain alcohol/water interfaces. Its application is complicated by the formation of interfacial aggregates that also leads to a shortening of the TR-SSHG decay, although this effect can be minimized when working at low concentrations where TR-SSHG signal is dominated by EB monomers. In such conditions, the TR-SSHG signal at the dodecane/water interface is dominated by a slow, >1 ns, decaying component, whereas the S_1 lifetime of EB in bulk water is on the order of a few picoseconds. This huge difference points to the existence of a large population of EB molecules, which

are not hydrogen-bonded to the solvent or, at least, do not undergo hydrogen-bond-assisted non-radiative deactivation. Such effect may arise from a specific orientation of EB molecules at the interface, which prevents contact between the hydrogen-bond-accepting nitro groups and water, or from the mechanism of the hydrogen-bond-assisted deactivation itself that is no longer operative at the interface.

The above findings may also be summarized in a different way: the S_1 state of EB that is nonfluorescent in aqueous solutions becomes long-lived and, thus, fluorescent once EB is adsorbed at a liquid/water interface. This opens a possibility to study interfaces by fluorescence techniques if the ratio of adsorption to bulk molecules is sufficiently large to make the bulk background fluorescence negligible. Because of the ultrashort excited-state lifetime of EB in water, this condition should be possible to satisfy in systems such as emulsions, protein solutions, nanoparticles dispersed in water, or colonies of living cells, provided that the results from the alkane/water interfaces studied here are general and transferable to other systems of similar nature. One could think of using EB to measure the total surface of nanoparticles dispersed in water by detecting the fluorescence of the sample and relating its intensity to the total area of their interface with water. Preliminary experiments have shown that the fluorescence intensity of EB in aqueous solution increases upon adsorption on micelles formed after the addition of a surfactant to the solution. Further studies are required to test the applicability of EB and other molecules deactivated in a hydrogen-bond-assisted process as fluorescent probes of interfacial properties, but if they appear to be positive, this may become a powerful technique applicable to various fields of surface chemistry and biology.

4.2.2. Salt effect

The conventional understanding of experimental findings obtained by surface tension and surface electric potential measurements has changed over the last two decades as a result of new investigations of the interfacial structure of aqueous electrolyte solutions. Previous experiments, based on a macroscopic approach, have revealed that ions exhibit a monotonically increasing concentration toward the bulk, leaving the outermost liquid layer essentially depleted of ions.[173-175] More recent studies, carried out with surface-sensitive techniques such as SSHG and SSFG lead to a more complicated picture:[176-180] small nonpolarizable hard anions are repelled from the aqueous surface in agreement with the traditional picture based on continuum solvent

models (i.e., behave “classically”), whereas polarizable soft anions exhibit a nonmonotonic interfacial distribution being enhanced at the outermost surface layer and depleted in the subsurface, where cations, in turn, are enhanced.

As has been shown in a recent study carried out by measurements of the stationary SSHG intensity, anions adsorbed at the interface attract organic cations by Coulomb interactions and lead to a significantly higher organic dye adsorption at air/liquid interface.[181] The excess negative charge density at the interface increases with the square root of the bulk anions concentration. The leading role of electrostatic forces in the mechanism of enhanced adsorption of an organic dye, malachite green (MG), has been confirmed by a very good agreement of the proposed model with the experimental data.[114, 182, 183]

Studies on ions at interfaces frequently involve various thiocyanate salts. Numerous papers by Viswanath et al.[184-186] are devoted to the SSFG investigation of thiocyanates affecting the interfacial water structure and the lipid chain ordering. It has been demonstrated that the concentration of thiocyanate anions at the interface is higher compared to the bulk and, at the same time, the structure of interfacial water is significantly modified.[185]

The ranking of the relative influence of ions on a wide variety of processes in water, ranging from colloidal assembly to protein folding, is called Hofmeister series.[187] The thiocyanate anion is classified in the Hofmeister series as a salting-in agent,[187] i.e., its salts enhance the solubility of proteins in aqueous solutions and reduce the number of macromolecules adsorbed at the surrounding aqueous surface.[184-186] On the contrary, addition of NaSCN to aqueous solutions of MG has been found to provoke a huge enhancement of the SSHG efficiency at air/water and alkane/water interfaces revealing a rise of the number of dye molecules adsorbed at an interface. TR-SSHG experiments with MG at the air/water interface carried out by Punzi et al.[116] show that the enhancement of SH intensity by addition of NaSCN to the bulk phase is accompanied by a remarkable slow down of the excited-state dynamics of MG. It has been proposed that the increase of the SH intensity upon addition of salt is not only due to an enhanced adsorption of the solute molecules at the interface but also due to the formation of MG aggregates.

Combined experimental and theoretical studies on thiocyanide adsorption at the air/water[91-93, 188, 189] interface reveal a simple Langmuir behavior of the SCN^- surface

concentration with respect to the bulk, contrary to the adsorption of organic ions, where the interaction between adsorbed ions has to be taken into account when correctly describing the relation between surface and bulk concentrations.[189]

This section focuses on demonstrating the salting-out effect, i.e., the increase of the solute concentration at the surface upon addition of various inorganic sodium salts into aqueous solutions of MG.[118] TR-SSHG is used here to monitor the relative concentration of MG aggregate adsorbed at the interface as a function of bulk dye and salt concentrations. A model proposing a simplified quantitative description of the interaction between the adsorption of inorganic (salts) and organic ions (MG) is also presented.

It has been shown in **Section 4.1.1** that the TR-SSHG profiles of MG can be both single- and biexponential depending on the MG concentration: the faster component is attributed to the deactivation of excited monomeric MG molecules, whereas the longer component is attributed to the deactivation of excited aggregates.[115, 116] Thus, the recorded SSHG kinetics presented here could be fitted by the sum of two exponential functions convolved with a Gaussian instrument response function *f(t)*, where A_1 and A_2 are decay amplitudes corresponding to the deactivation of monomers and aggregates, respectively, and A_0 accounts for a weak long-lived decay component also observed in the data (Eq. 4.3). The origin of this component is unclear but its contribution is so small, less than 10% in most cases, that it will be neglected in further discussion. Thus, when analyzing several time profiles simultaneously, for example, profiles recorded with different salt concentrations, both short and long decay times τ_1 and τ_2 can be kept constant. In this sense, the relative magnitude of A_2 on the salt concentration of the lower phase appears to be of interest, since it indicates the formation of dye aggregates.

First, a series of measurements with two different alkanes, the more viscous tetradecane and the less viscous octane, was carried out. For these experiments, four different salts, NaCl, NaSCN, NaBr, and Na_2SO_4, were chosen and compared. The concentration of MG was 1.5×10^{-4} M. The time profiles recorded at various concentrations of the same salt were analyzed simultaneously, i.e., all amplitudes A_i in Eq. 4.3 were set free, whereas the decay times τ_1 and τ_2 were kept constant for the different sets of data. The SSHG time profiles of MG obtained with various concentrations of NaCl at the tetradecane/water interface as well as the relative

amplitudes of the fast and slow decay components with the four salts are shown in **Figure 4.34**.

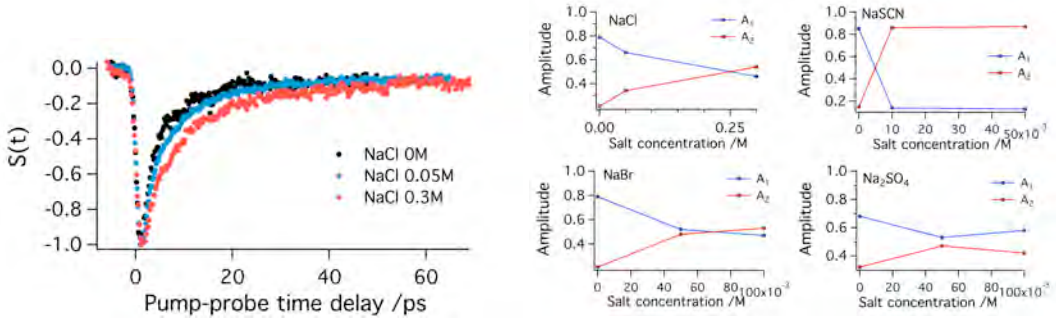

Figure 4.34. Left: TR-SSHG profiles of MG at the tetradecane/water interface measured at 400 nm without and with addition of different concentrations of NaCl; **Right**: dependences of the amplitudes on the salt concentration with NaCl, NaSCN, NaBr, and Na_2SO_4 (the connecting lines in panels b-e are to guide the eyes only).

Figure 4.34 reveals a clear slowdown of the ground-state recovery of MG upon addition of NaCl and therefore a clear rise of A_2 with the salt concentration. As already mentioned, this amplitude is attributed to the formation of dye aggregates at the interface. Interestingly, the rise of this amplitude seems to saturate with further increase of the salt concentration. The same analysis was done for analogous sets of interfacial systems but with octane as the upper phase and qualitatively similar dependencies were obtained (**Figure 4.35**).

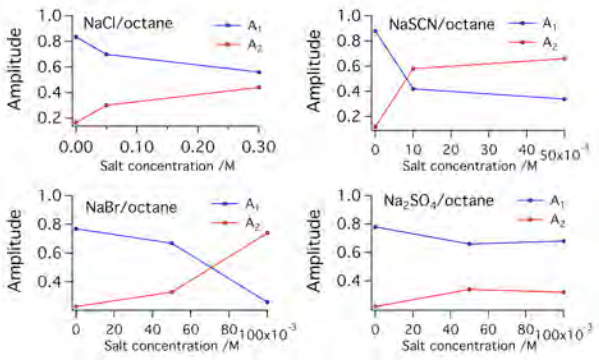

Figure 4.35. Dependences of the amplitudes on the salt concentration obtained with NaCl, NaSCN, NaBr, Na_2SO_4, respectively, with MG in octane/water systems. The connecting lines in panel are to guide the eyes only.

The obtained decay times are summarized in **Table 4.5**.

Interfacial system	τ_1	τ_2
octane/water+NaCl	2.2	12
octane/water+NaSCN	2.6	17
octane/water+NaBr	2.4	8.4
octane/water+Na_2SO_4	2.0	9.4
tetradecane/water+NaCl	1.9	11
tetradecane/water+NaSCN	2.5	19
tetradecane/water+NaBr	2.5	12
tetradecane/water+Na_2SO_4	1.7	8.8

Table 4.5. Decay times obtained from the biexponential analysis of the time profiles measured with MG at different interfaces.

All the systems under study exhibit similar behavior: the shorter decay time is equal to approximately 2 ps, whereas the longer one is typically around 10 ps. The amplitude of the slower component increases with increasing salt concentration but the rise seems to saturate at a certain salt concentration. The various salts differ by the concentration at which saturation is reached and the maximum magnitude of A_2. The difference in the amplitudes behavior when varying alkanes is not very pronounced, allowing flexibility in choosing alkanes for more detailed investigations of the salt effect. However, the observed salt effect depends substantially on the nature of salt anions. From our data, the salt effect increases in the following order: $SO_4^- < Cl^- < Br^- < SCN^-$.

For further studies, only two salts were selected: NaSCN as the salt that exhibits the strongest effect, i.e., saturation of A_2 is reached at very low salt concentration and A_2 reaches a high value, and NaCl, for which the salt effect is less pronounced. These studies were carried out at the dodecane/water interface with a MG concentration of 10^{-5} M, i.e., 15 times lower than in the preliminary experiments in order to reduce formation of aggregates in pure water solution. As in the previous data analysis, the global fit was employed. Since the two associated time constants are attributed to monomeric and aggregated forms of the same dye, their values should not depend on a particular salt added to the bulk solution. Therefore, all time profiles recorded with both NaSCN and NaCl were analyzed simultaneously and the time constants have been kept equal for all decays. The dependences of the decay amplitudes A_1 and A_2 on the salt concentration are shown in **Figure 4.36 left**. The short and long decay time constants were found to be 2.1 ps and 13 ps, respectively. These values and the dependence of the amplitudes on the salt concentration are very similar to those observed in the preliminary measurements at higher MG concentration.

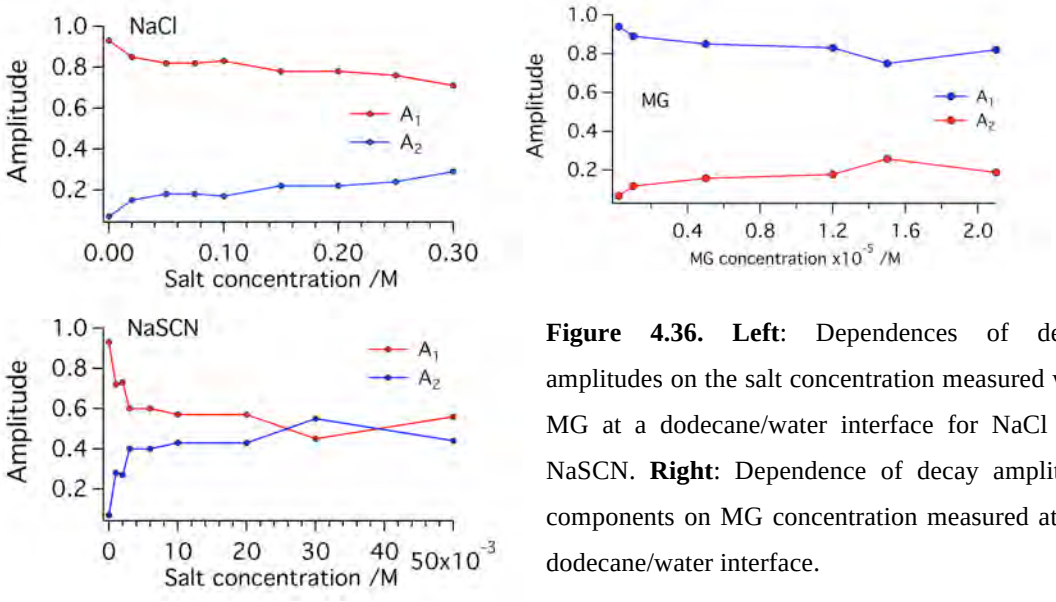

Figure 4.36. Left: Dependences of decay amplitudes on the salt concentration measured with MG at a dodecane/water interface for NaCl and NaSCN. **Right**: Dependence of decay amplitude components on MG concentration measured at the dodecane/water interface.

The results at liquid/liquid interfaces can be compared with those obtained with the air/liquid system studied previously: in those experiments, the influence of the addition of salts on the stationary SH intensity as well as TR-SSHG profiles were investigated. The SH intensity was found to rise with increasing salt concentration and to saturate at high concentrations. This resembles the behavior of the decay amplitude A_2 (**Figure 4.36 left**), which reflects the formation of MG aggregates at the interface. The dependence obtained in ref[116] has been interpreted as follows: the increase of the SH intensity upon addition of salt is not only due to an enhanced adsorption of the MG molecules at the air/liquid interface but also due to the formation of aggregates. Comparing the results at air/liquid and liquid/liquid interfaces, one can conclude that the increase of salt concentration enhances MG aggregation at both types of interfaces and, hence, the SH intensity. The so-called salting out effect takes place: the presence of salt anions leads to an increase of the number of MG molecules at the surface and, hence, increases the probability of the aggregate formation.

The gain of the amplitude A_2 with increasing salt concentration can be compared to the increase of A_2 with increasing dye concentration. Such dependence is presented in **Figure 4.36 right**: it can be seen that in this case as well, the contribution of the decay component attributed to the deactivation of aggregates increases with the bulk concentration of the dye and that finally a saturation is reached. The saturation value of A_2 is, however, much lower in pure water solution than in the system containing

salts. One can conclude that exhibiting the gain of A_2 with the bulk concentration, both graphs, in fact, reflect the increasing number of MG molecules at the interface: in the first case (**Figure 4.36 left**), it is provoked by the rising number of salt anions in the bulk, whereas in the second case (**Figure 4.36 right**) it is done by the rise of the dye concentration. This once again demonstrates that the addition of anions stimulates to a different extent the migration of MG cations toward the interface favoring thus aggregation. The difference observed between NaCl and NaSCN reflects the effect of the salt anion.

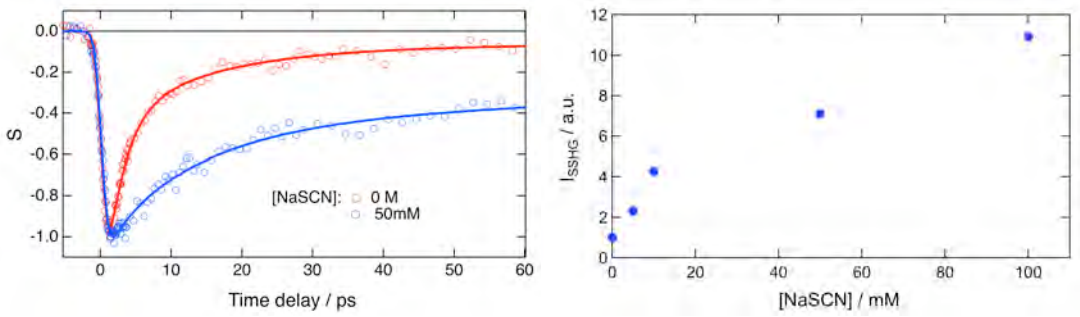

Figure 4.37. **Left**: TR-SSHG profiles measured at 420 nm with MG ($1.5x10^{-4}$ M) at the dodecane/water interface with and without NaSCN. **Right**: dependence of the relative stationary SSHG intensity of MG on the NaSCN concentration.

The salt effect on the TR-SSHG profiles is the same at all wavelengths except at 500 nm (**Figure 4.37**).

At 500 nm, addition of NaSCN has the same influence on the TR-SSHG profile as the increase of the concentration of MG, i.e. the amplitude of the positive component decreases with increasing salt concentration and totally vanishes at 50 mM (**Figure 4.38**). However, the time constants associated with slow and fast components are not significantly affected. As a consequence, this effect can be ascribed to an increased population of MG aggregates and to a parallel decrease of MG monomers at the interface.

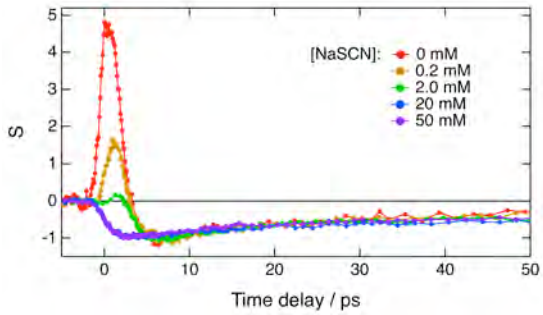

Figure 4.38. TR-SSHG signal profiles measured at 500 nm with MG ($1.5x10^{-4}$ M) at the dodecane/water interface with different bulk concentration of NaSCN.

At least two aggregation mechanisms are possible: the addition of salt increases the amount of MG cations being adsorbed at the interface and MG aggregation occurs directly at the interface; or, MG aggregation occurs already in the bulk and then the migration of these aggregates toward the interface takes place. To find out which of these mechanisms prevails, the UV-VIS absorption spectra of MG without and with the addition of salts (NaCl and NaSCN) were measured (**Figure 4.39**).

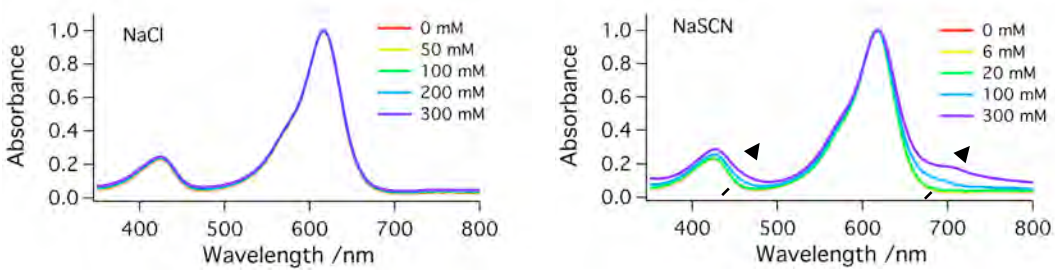

Figure 4.39. Normalized UV-VIS absorption spectra of MG at 10^{-5} M in water with various concentrations of salts: NaCl and NaSCN. The arrows illustrate the spectral broadening.

Comparing normalized spectra of MG with NaCl and NaSCN, one can see that addition of NaSCN leads to increasing absorption on both sides of the MG absorption bands. These features can be attributed to the aggregation of MG.[116] Moreover we can conclude that the aggregates are formed by MG cations, because the spectral changes accompanying aggregation are relatively small: if the aggregates were created by the neutral (carbinol) form of MG, the spectral changes would be much more pronounced because the carbinol form does not absorb in the visible range.[110] The effect of the addition of thiocyanide anions to organic dye solutions has already been reported by Barnes[190] and Punzi et al.:[116] both have proposed strong aggregation and precipitation of the dyes upon addition of NaSCN. With NaCl this effect is much weaker as the MG spectra do not demonstrate any significant changes when varying the salt concentration up to 300 mM. At the moment there is no complete theory of ion-solute

interactions, which could explain why NaSCN stimulates MG aggregation so efficiently compared to NaCl. Thiocyanates increase solubility of proteins in water solutions and are known to be salting-in agents in clear opposition to their behavior observed in our experiments. Some works indicate that specific dispersion interactions should be included in the theory in order to explain the salting in effect of thiocyanates on proteins.[191] Moreover, the high propensity of SCN^- anions to protein/water interface should be responsible for the increasing solubility of proteins upon addition of thiocyanates.[11] It has been proposed that this effect is related to the weak hydration of this anion as measured by neutron diffraction.[192] The weaker free energy of hydration of SCN^- compared to Cl^- could explain the higher concentration of SCN^- at the interface. Furthermore, because SCN^- is poorly hydrated, anions present in the bulk solution may interact with the MG cations and reduce their solubility and hence enhance the aggregation of MG. Consequently, the following hypothesis about the influence of salts on aggregation can be proposed: addition of NaCl does not lead to significant aggregation in the bulk, but instead increases the number of MG cations adsorbed at the interface, so that the formation of MG aggregates occurs mainly at the interface. On the other hand, addition of NaSCN increases the amount of aggregates being formed already in the bulk with a further migration toward the interface.

The same conclusion about the aggregation mechanism also can be drawn when trying to analyze the measured decay amplitude A_2. The authors of ref[189] suggest the Frumkin-Fowler-Guggenheim (FFG) model to reproduce the dependence of the concentration of interfacial molecules on the bulk concentration. This model is a variant of the Langmuir model, which, in turn, assumes the partition of the system into bulk and surface regions and postulates a chemical equilibrium for the exchange of solvent and solute molecules between two regions. Extending the Langmuir model, the FFG model accounts for the interaction between the solute molecules at the surface. This model results in the following relationship between the bulk concentration C and the fractional surface coverage $\theta = N_s / N_s^{\max}$, where N_s is the number of solute molecules at the interface and $N_s^{\max}$ the maximum possible number of molecules at the surface:

$$\frac{\theta}{1-\theta}\exp(-g\theta) = K'C \qquad (4.4)$$

where g is an interaction parameter (Eq. 4.4 with $g = 0$ yields the regular Langmuir model) and K' is a modified equilibrium constant or a modified Langmuir constant. This model has been used to describe the adsorption of organic ions, such as tetrabutylammonium iodide, at air/liquid interfaces and it has been shown to be in a significantly better agreement with the experimental data than the regular Langmuir model.[189] On the other hand, for small inorganic ions, the regular Langmuir model has been shown to give a satisfactory agreement with the experiment.[188] In the latter case, the fractional coverage of ions at the surface of a water solution can be expressed as

$$\theta = \frac{C}{C + 55.5M\exp(\frac{\Delta G_{abs}}{RT})} \qquad (4.5)$$

where ΔG_{abs} is the Gibbs free energy of solute adsorption to the interface, and RT is the product of the gas constant and temperature. The free energy of adsorption of SCN^- at the air/water interface has been found to be $\Delta G_{abs} = (-6.7 \pm 1.1)$ kJ/mol.[188] With this value, the dependence of the surface concentration of the ions on the bulk salt concentration, which has been shown to increase with a square root of the bulk concentration of anions,[181] is practically linear at low concentrations (**Figure 4.40**).

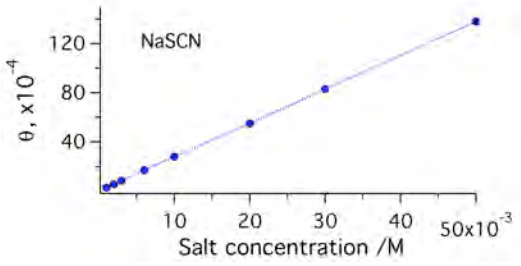

Figure 4.40. Dependence of the fractional surface coverage of SCN^- at an air/water interface on the bulk salt concentration calculated from Eq. 4.6.

Although this result has been obtained for air/water interface and for SCN^- only, it is safe to assume that at the low salt concentrations used in the present study, this linear dependence remains valid for liquid/liquid interfaces as well as for Cl^-.

Further, it will be assumed that the presence of salt anions at the interface increases the equilibrium constant K' for the adsorption of the dye and that this increase is

proportional to the surface concentration of the anions. Therefore, K' in a system where the salt concentration is equal to C_{salt} can be expressed as

$$K'(C_{salt}) = K'_0 + \kappa \cdot C_{salt} \tag{4.6}$$

where K'_0 is the equilibrium constant for dye adsorption in pure water solution and κ is a proportionality coefficient.

Assuming a linear relation between θ and A_2, $\theta = \alpha \cdot A_2$ and substituting K' in Eq. 4.4 by Eq. 4.6, one can obtain a relationship between the slow decay amplitude and the bulk salt concentration:

$$\frac{\alpha A_2}{1-\alpha A_2}\exp(-g\alpha A_2) = (K'_0 + \kappa C_{salt})C \tag{4.7}$$

Since it is impossible to find an algebraic solution of Eq. 4.5 for A_2, the fit has been performed with the inverted dependence $C_{salt}(A_2)$:

$$C_{salt}(A_2) = \frac{1}{\kappa}\left[\frac{\alpha A_2}{C(1-\alpha A_2)}\exp(-g\alpha A_2) - K'_0\right] \tag{4.8}$$

The best-fit curve with NaCl obtained with K'_0 = 0.18 L/mol and κ = 8 L^2/mol^2 is presented in **Figure 4.41**. The good fit of Eq. 4.8 to the data indicates that the simple linear relations between K' and C_{salt}, and also between θ and A_2, assumed when deriving this equation, are a sufficiently good approximation.

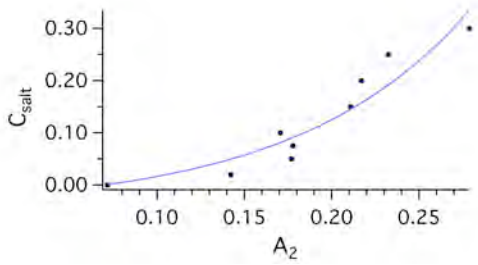

Figure 4.41. Best fit of the modified FFG model (Eq. 4.8) to the experimental data obtained with NaCl.

Figure 4.41 points to a possible saturation at larger NaCl concentrations. This is expected, since the increase of salt concentration provokes a continuous attraction of MG cations to the interface, which should finally lead to the occupation of all the interfacial sites. It has to be noted that the FFG model presumes the formation of aggregates at the interface only and does not take into account the mechanism of the bulk aggregation, which, as has been discussed earlier, is most probably provoked by NaSCN addition. Therefore, Eq. 4.8 is not expected to fit the data measured with NaSCN, and, indeed, it turns out to be impossible to obtain an acceptable agreement of this model with the NaSCN data.

The above analysis interpreted in terms of the results obtained with thiocyanate anions at air/water interfaces[91-93, 188, 189] leads to the following description of the salting-out phenomenon. The primary effect upon addition of sodium salt to a solution of a dye such as MG is the dissociation of salt and the migration of the anions toward the surface. The presence of these anions at the interface shifts the equilibrium between bulk and surface populations of dye cations in favor of the latter and the number of adsorbed dye molecules increases, tending to maintain a chemical equilibrium for the new conditions. The increase of the surface dye concentration leads to aggregation observed as an increase of the SH intensity and a slowing down of the excited-state deactivation of MG in the TR-SSHG experiments. This picture, valid for salts exhibiting moderate salting-out effect, changes for thiocyanate salts which have much more dramatic influence on the aggregation at interfaces. Addition of SCN^- to MG solution leads to efficient aggregate formation in the bulk due to a significant reduction of solubility. The positively charged aggregates are attracted toward the surface in a similar manner as monomeric cations and migrate to the interface causing a fast saturation of adsorption.

There is also a Hofmeister series for cations according to their salting-in properties,[193] which should also reflect their interfacial affinity. It is generally assumed that small non-polarisable hard cations, such as Na^+ and K^+, are repelled from the surface,[11, 92, 193] even though there has been no systematic study on this matter. On the other hand, cations located at the other side of the Hofmeister series, such as guadinium cation, GuH^+, are expected to exhibit the highest interfacial affinity.[193] Guanidinium chloride is also known to be one of the most effective protein denaturants.[194]

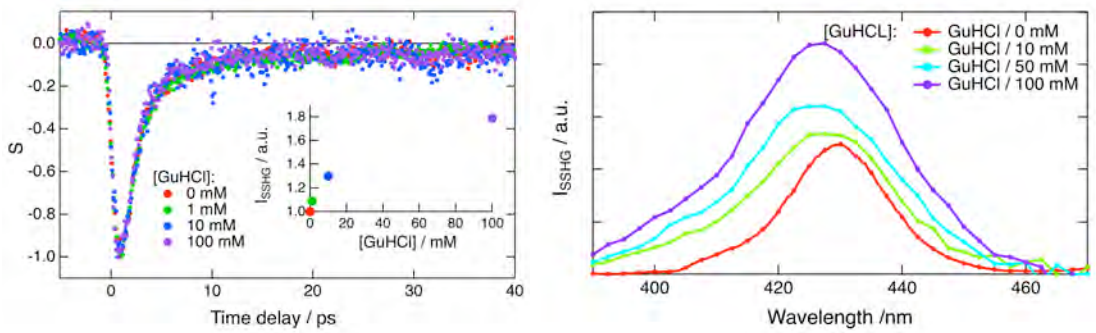

Figure 4.42. Left: TR-SSHG signal profiles measured at 400 nm with MG ($1.5x10^{-4}$ M) and various concentrations of GuHCl at the dodecane/water interface. Inset: dependence of the relative stationary SSHG intensity at 430 nm on the GuHCl concentration. **Right**: stationary SSHG spectra measured with MG ($1.5x10^{-4}$ M) at the dodecane/water interface with different bulk concentration of GuHCl.

Addition of GuHCl to the aqueous phase leads to an increase of the stationary SSHG signal intensity by a factor of less than 2, but does not affect the TR-SSHG profile (**Figure 4.42**). These two results seem contradictory as, on one hand, the first points to an increase of the interfacial concentration of MG and, on the other hand, the second indicates that aggregation is not enhanced. If GuH^+ were accumulating at the interface, a depletion of the interfacial MG concentration would be expected, due to the electrostatic repulsion between both cationic species. Recent molecular dynamics simulations of GuH^+ at the air/water interface indicate that, despite being on the salting-in side of the Hofmeister series of cations, GuH^+ is rather depleted from the interfacial region.[195] This finding also agrees with surface tension measurements.[193] On the other hand, an anisotropic orientation of GuH^+, with the molecular plane parallel to the interface, was found in these simulations.[195] Such a low interfacial affinity of GuH^+ can explain the negligible effect of GuHCl on the TR-SSHG profiles. However, it cannot account for the observed increase of stationary SSHG signal. It should be noted that this increase of intensity is much smaller than that found with SCN^-.[116, 118] Addition of NaCl has been found to also favour adsorption of MG at the interface but to a much small extent than NaSCN.[116, 118] Therefore, the increase of the SSHG signal could be due to the interfacial Cl^- population. However, with this rather modest salt concentration, the effect is too small to significantly affect the population of aggregates. Additionally, the orientational anisotropy of GuH^+ found from molecular dynamics simulations could increase the orientational

anisotropy of the MG dyes at the interfaces, and could therefore lead to an enhancement of the SSHG intensity.

Summary. This study showed that the amount of aggregation of MG, measured by TR-SSHG, is a powerful probe of the relative interfacial affinity of anions. The effect on the formation of aggregates caused by various anions was compared and the studied anions could be sequenced as $SO_4^- < Cl^- < Br^- < SCN^-$, which means that SCN^- has the highest affinity to the interface. In case of NaCl, the effect of salt addition is attributed to the linear increase of the equilibrium constant between surface and bulk dye population with the concentration of salt. In case of NaSCN, the addition of salt results in a strong reduction of dye solubility and in the formation of aggregates in the bulk solution already. The aggregates migrating toward the interface occupy the majority of the available adsorption sites and their excited-state dynamics predominates the observed time dependence of the SSHG signal. The guanidinium cation was found to be repelled from the interface, as also concluded from previous surface tension measurements and molecular dynamics simulations.[193, 195]

4.2.3. Controlling the population of adsorbates at liquid interfaces

It has been shown in the previous section that the population of an organic molecule could be controlled by the addition of salts by the example of MG and salts with different interfacial affinities (see **Section 4.2.2**): the addition of salt with a high surface affinity of its anion led to the electrostatic attraction of the positively charged dye molecules toward the interface and provoked the formation of dye aggregates.

The present section reports on a comparison of the effect of the addition of salts and charged surfactants on the excited-state dynamics of MG at the dodecane/water interface. By definition, surfactants have a strong affinity for interfaces, with their charged head confined to the upper part of the aqueous surface and their long hydrophobic alkyl chains lying in the lipophylic phase.[196, 197] This leads to a charging of the interface, similarly to that which should occur for ions, like SCN^-, that are thought to have a preferential affinity for interfaces. Therefore, if the enhanced aggregation of MG upon addition of salting-in anions indeed arises from electrostatic interaction, the same effect should be observed with a negatively charge surfactant.

The present investigation reveals that this is actually the case. Further results obtained with a positively charged surfactant and with the dianionic dye EB will also be presented. It has been shown (**Sections 4.1.1** and **4.2.2**) the contribution of MG monomers and MG aggregates was only inferred from their different ground-state recovery dynamics. Here, both species are also spectrally distinguished using a TR-SSHG setup with a tunable probe wavelength.

Figure 4.43 shows TR-SSHG profiles as well as the stationary SSHG intensity with different concentrations of the anionic surfactant SDS.

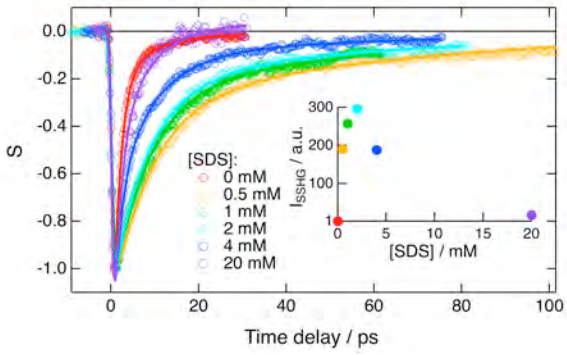

Figure 4.43. TR-SSHG profiles measured at 400 nm, upon excitation at 618 nm, with MG (10^{-5} M) and various concentrations of SDS at the dodecane/water interface. Inset: dependence of the stationary SSHG intensity at the band maximum on the SDS concentration.

Small concentrations of SDS lead to a strong increase of the SSHG intensity, the maximum of which is reached at approximately 2 mM. Further addition of SDS up to a concentration exceeding the critical micellar concentration (CMC), which is around 8 mM,[198] causes a decrease of the SSHG intensity down to about the same value as that without surfactant. The TR-SSHG profiles are also affected by the presence of SDS. A strong slowing down of the signal recovery dynamics at 400 nm is observed with a small amount of SDS. At 500 nm, the positive feature due to MG monomer in the S_1 state has totally vanished at 0.1 mM SDS (**Figure 4.44**).

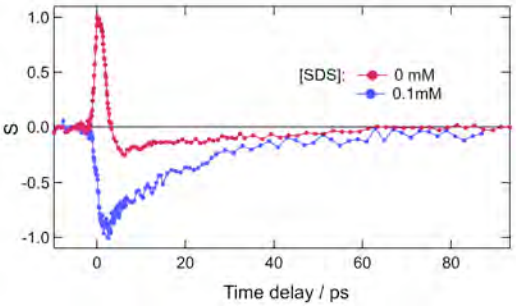

Figure 4.44. TR-SSHG profiles measured at 500 nm, upon excitation at 618 nm, with MG ($1.5 \cdot 10^{-4}$ M) at the dodecane/water interface with and without SDS.

In **Figure 4.43** the TR-SSHG profiles remain essentially the same up to about 2 mM SDS. At higher SDS concentrations, the signal recovery dynamics become faster and, at 20 mM SDS, it is almost as fast as without surfactant. Multiexponential global analysis of the TR-SSHG profiles at different SDS concentrations required not less than three exponential functions with 1.7, 10 and 62 ps. The relative amplitude of the fast component amounts to 0.94 in the absence of SDS, drops to essentially zero at 0.5 and 1 mM SDS, and increases again up to 0.7 at the highest concentration. The amplitude of the two slower components shows the opposite trend with that of the 10 ps component remaining larger than that of the 62 ps component. Whereas the fast component can be assigned to MG monomers, the two slowest are ascribed to MG aggregates. The fact three exponentials were required here is most probably due to the superior signal-to-noise ratio of the profiles measured with small SDS concentrations and to the high relative amplitude of the slow components. In the other cases, the amplitude of the slow recovery is too small to make three-exponential analysis relevant.

The initial rise of the SSHG intensity with SDS concentration can be attributed to an increase of the number of MG molecules contributing to the signal. It can have two origins: (1) An enhanced adsorption of MG at the interface favored by electrostatic interactions between the negatively charged interface and the cationic dyes; (2) The existence of an orientational anisotropy of the MG molecules not only at the interface but also deeper in the aqueous phase because of the static electric field, $\vec{\Phi}(0)$, associated with the charged surfactants at the interface. In such case, the SSHG signal originates from both the second- and third-order nonlinear polarizations:[199]

$$\begin{aligned}\vec{P}_{SSHG}(2\omega) &= \vec{P}^{(2)}(2\omega) + \vec{P}^{(3)}(2\omega) \\ &= \varepsilon_0 \vec{\vec{\chi}}^{(2)}(2\omega,\omega,\omega)\vec{E}(\omega)\vec{E}(\omega) + \varepsilon_0 \vec{\vec{\chi}}^{(3)}(2\omega,\omega,\omega,0)\vec{E}(\omega)\vec{E}(\omega)\vec{\Phi}(0)\end{aligned} \qquad (4.9)$$

where $\vec{\vec{\chi}}^{(3)}$ is the third-order nonlinear electric susceptibility tensor, and $\vec{E}(\omega)$ is the electric field oscillating at the probe frequency ω.

Because of this static field, the SSHG signal can also originate from partially oriented MG dyes located in the bulk region close to the interface. If the increased SSHG intensity observed upon small additions of SDS were due to this effect, the TR-SSHG profiles should mostly reflect the excited-state dynamics of MG in bulk water. In such

case, the profiles would be totally different than those measured here. Indeed, at 10^{-5} M, MG is only present as a monomer in bulk water and its excited-state lifetime amounts to about 600 fs.[115, 200] The absence of the fast TR-SSHG component at small SDS concentration indicates that the SSHG signal is entirely due to MG aggregates and that the contribution from the third-order nonlinear polarization is not significant here.

At 4 mM and higher SDS concentrations, the stationary SSHG intensity decreases and the TR-SSHG dynamics accelerates. Considering that a SDS monolayer at the air/water interface is achieved at approximately 6 mM,[201] these observed changes of the SSHG signal occur when the interface is almost entirely covered by SDS. Indeed, Eisenthal and co-workers showed that, in the presence of a surface-active dye, the saturation of the interfacial SDS concentration occurs substantially below 6 mM.[202] Richmond and co-workers have measured a decrease of the SSFG intensity associated with several SDS vibrations at the air/water interface upon increasing SDS concentration above approximately 2 mM, and tentatively ascribed it to an increase of the alkyl chain disorder brought about by micelle formation.[201] It is difficult to account for the effects observed here with MG in terms of chain disorder. We rather propose that these effects are due to the superior affinity of SDS for the interface compared to MG. At small SDS concentrations, the surface coverage is low and the negative charge of the interface favors adsorption and hence aggregation of MG. Increasing SDS concentration augments the coverage of the interface and, despite the electrostatic interaction, inhibits adsorption of MG. This leads to a decrease of MG population, hence of the stationary SSHG intensity, and to a smaller population of aggregates, thus to a faster recovery of the TR-SSHG profile.

Similar stationary SSHG and TR-SSHG measurements have been performed with the cationic surfactant CTAB. At 0.1 mM CTAB, the SSHG intensity decreases to a level close to the limit of detection. This result can be very well explained in terms of the electrostatic repulsion between the positively charged CTAB surfactant and the cationic MG molecules. Since CTAB exhibits even bigger interfacial affinity than SDS,[203, 204] its addition results in a positive charging of the interface and to the repulsion of the cationic MG dyes from the interface.

Finally, the above experiments were repeated with the EB dianion instead of MG. The stationary SSHG spectrum of EB at the water/dodecane interface peaks around 425 nm (**Figure 4.45**) and most probably originates from a $S_2 \leftarrow S_0$ two-photon resonance.

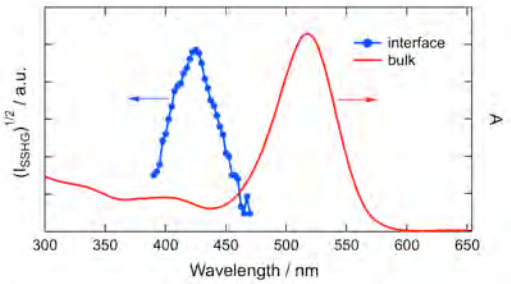

Figure 4.45. Stationary SSHG spectrum of EB at the dodecane/water interface and electronic absorption spectrum of EB in water.

Upon addition of CTAB, the stationary SSHG intensity increases up to a surfactant concentration of approximately 0.1 mM and then decreases down to reach a value close to that without CTAB at concentrations exceeding the CMC of 0.9 mM (**Figure 4.46 inset**).[205] Upon excitation of EB at 515 nm, the TR-SSHG intensity decreases, due to a depletion of the ground-state population, and recovers its original value after about 60 ps (**Figure 4.46**).

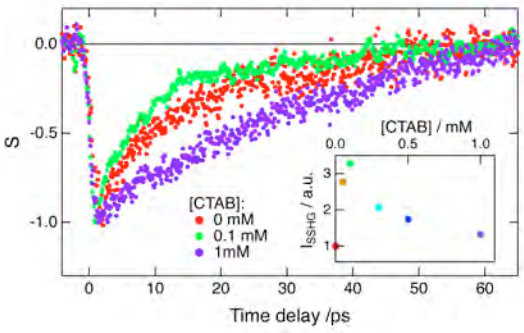

Figure 4.46. TR-SSHG profiles measured at 400 nm, upon excitation at 515 nm, with EB (10^{-4} M) and different concentrations of CTAB at the dodecane/water interface. Inset: dependence of the stationary SSHG intensity at the band maximum on the CTAB concentration.

Upon addition of CTAB, the ground-state recovery accelerates up to 0.1 mM and slows down at higher concentrations. Above 1 mM, the dynamics becomes even slower than without surfactant. It has been shown that the excited-state dynamics of EB at alkane/water interface revealed a substantial acceleration of the ground-state recovery upon increasing the bulk concentration of EB (**Section 4.2.1**). This effect was ascribed to the increasing contribution of EB aggregates, known to have a short excited-state lifetime,[162] to the SSHG signal. Therefore, the acceleration of the TR-SSHG dynamics upon addition of 0.1 mM CTAB and the subsequent slowing down can be ascribed to a higher, respectively a lower, interfacial population of EB. This

behavior is very similar to that observed with MG upon addition of SDS and can be interpreted likewise, i.e. an enhancement of interfacial dye population at small surfactant concentration favored by electrostatic interactions, followed by a depletion of the dyes from the interface due to its coverage by the surfactant.

Finally, addition of SDS had the same effect on the SSHG signal of EB than that of CTAB with MG, as expected. Indeed, the SSHG signal intensity decreases dramatically even at very small SDS concentrations and, above 0.1 mM SDS, no SSHG signal can be detected. Here again, the large interfacial affinity of SDS leads to a negative charging of the interface and the dianionic EB molecules are thus repelled.

Summary. This investigation shows that adding small amounts of ionic surfactants can control the interfacial population of charged dyes. Adsorption of the dye is enhanced when using oppositely charged surfactants, whereas depletion of dye occurs when adding a surfactant with the same charge. However, independently of the relative charges of dye and surfactant, a large interfacial coverage by the surfactant substantially decreases the dye population, due to the smaller affinity of the latter for the interface. Such effects are only expected with dyes like those used here, which have a good solubility in water and are not highly surface active.

This investigation gives a firm ground to the previous explanation for the effect of salts on the interfacial dynamics of MG (**Section 4.2.2**). The presence of a salting-in anion like SCN^- in the aqueous phase has the same effect as that of SDS, which, being a surfactant, has a strong interfacial affinity. It can be thus concluded that the enhanced aggregation of MG upon addition of SCN^- indeed originates from the affinity of this anion for the interface, and thus to its higher concentration in the interfacial region relative to the bulk solution.

4.3. Towards photoinduced electron transfer at liquid interfaces

All of the above-mentioned investigations concern intramolecular processes that cannot really be considered to be chemical reactions. Electron transfer (ET) can be regarded as the simplest chemical reaction, where the smallest chemically relevant particle is displaced from one molecule, the donor, to another, the acceptor.[206] There are several reasons for investigating ET at liquid/liquid interfaces. For example, a

dynamic probe could be based on photoinduced ET because the rate constant of an ET process depends strongly on environmental parameters such as the polarity, dielectric relaxation, and viscosity.[207] For more practical applications, bimolecular photoinduced ET at liquid interfaces between two reactants confined in different phases offers an interesting perspective for efficient charge separation, which is a crucial factor in solar energy conversion.[4] Eisenthal and co-workers have already demonstrated TR-SSHG measurements of photoinduced ET at a liquid interface.[208] In this case, ET took place from an aniline derivative that constituted the organic phase to excited coumarin located in the aqueous phase.

In our current investigations of bimolecular photoinduced ET, however, the donor is not a pure solvent but is dissolved in one of the phases. Some preliminary results will be shown here to demonstrate the potential of exploring the ET at liquid interface.[76]

One system under study was the EB/1,4-diazabicyclo(2.2.2)octane (DABCO) pair, where DABCO acts as an electron donor. TA measurements in acetonitrile revealed that the ET quenching of EB in the S_1 state by DABCO is diffusion-controlled and that the charge recombination (CR) of the ensuing radical pair is even faster. Such measurements were not performed in bulk water because of the very short S_1 lifetime of EB because of H-bond-assisted nonradiative deactivation.

Figure 4.47 shows TR-SSHG profiles recorded upon excitation of EB with different concentrations of DABCO at the dodecane/water interface. In this case, both reactants are in the aqueous phase. The fast recovery dynamics of the signal without DABCO is due to the presence of aggregates at the relatively high EB concentration (10^{-4} M) used to ensure a sufficient signal-to-noise ratio. Interestingly, this recovery slows down with increasing DABCO concentration. At the moment, no definitive explanation can be singled out to account for this slowing down of the GSR dynamics of EB in the presence of DABCO. However, if ET between EB and DABCO occurs at the interface, as expected from bulk measurements, a second pathway for the recovery of the EB ground state is open (**Figure 4.47 left**).

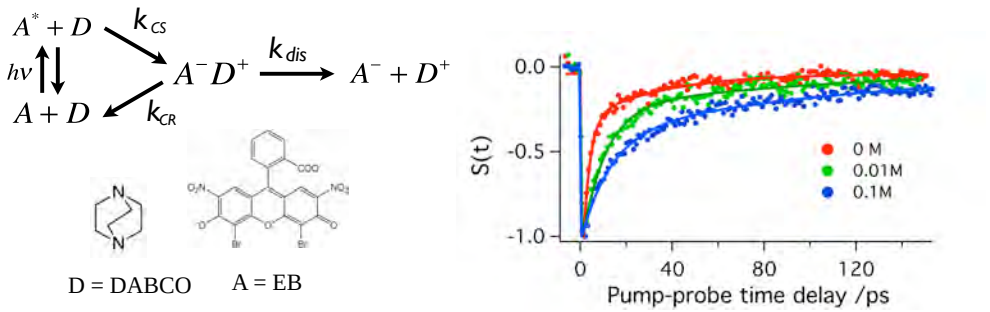

Figure 4.47. Left: Simplified scheme of a photoinduced ET reaction. **Right**: TR-SSHG profiles at 400 nm measured upon excitation of EB at the dodecane/water interface at 515 nm with different concentrations of DABCO.

This additional channel depends on the dynamics of both the ET quenching itself and the CR of the resulting radical pair. These are two consecutive processes, and the slowest determines the GSR dynamics. In the present case, the rate determining process cannot be the ET quenching because its dynamics becomes faster with increasing quencher concentration. Consequently, the rate-determining step should be the recombination of the radical pair. The contribution of this slower GSR pathway depends only on the quenching efficiency of EB and should thus increase upon addition of DABCO, as observed here. However, a decrease in the aggregation upon addition of DABCO as the origin of the slowing down of the GSR cannot be totally excluded, and additional measurements are still required to substantiate the ET hypothesis.

Figure 4.48 demonstrates another example of photoinduced ET at the liquid interface between R6G and *N*,*N*-Dimethylaniline (DMA). In this case, R6G is dissolved in the aqueous phase, whereas DMA – in the upper organic phase. One can see that the addition of a DMA, which acts as a donor, significantly accelerates the excited-state dynamics of R6G measured with the $\chi^{(2)}_{zxx}$ tensor element (the measurements with $\chi^{(2)}_{xxz}$ are in progress), independently of the probing wavelength. It means that in this case the ET through the interface is the rate determining process (Eq. 4.10).

$$-\frac{d[ES]}{dt} = (k_{CS}[DMA] + k_{IC})[ES] \qquad (4.10)$$

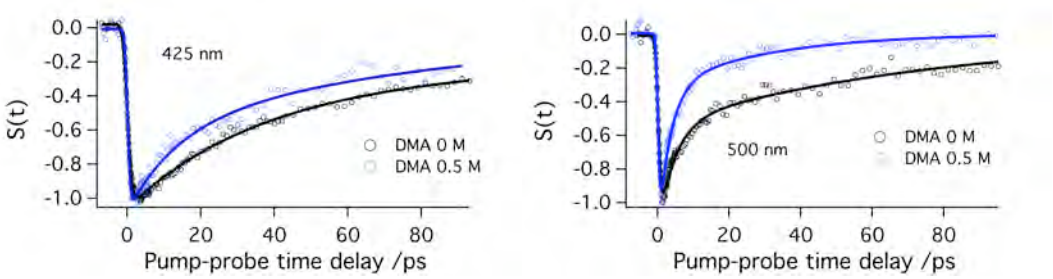

Figure 4.48. TR-SSHG profiles of R6G (10^{-3} M) measured at 425 nm (**left**) and 500 nm (**right**), with the $\chi^{(2)}_{zxx}$ tensor element, upon excitation at 530 nm, at the dodecane/water interface, with and without DMA.

Summary. These preliminary results showed the potential of TR-SSHG for investigating the photoinduced ET at and through liquid interfaces. As the investigations of the dynamics of truly photochemical reactions at the liquid interface still remain extremely scarce, more of an experimental effort remains to be done to make a breakthrough in this tempting direction.

5. CONCLUDING REMARKS AND OUTLOOK

Aqueous surfaces and interfaces are omnipresent and play an important role in many natural and technological processes. The anisotropic and heterogeneous interfacial region is typically only a few molecular diameters thick. While many established techniques exist for characterizing solid surfaces with atomic resolution, the situation is different for liquid aqueous interfaces. Primarily due to surface disorder, capillary waves, and volatility of liquid water, the knowledge about the detailed molecular structure of these interfaces has been rudimentary until recently. This has changed, however, within the last decade thanks to modern spectroscopic techniques. The goal of this thesis was to get a deeper insight into the photophysics and photochemistry of aqueous interfaces.

The emphasis was strongly on the results obtained using the state-of-the-art spectroscopic technique for investigating liquid interfaces – (time-resolved) surface second harmonic generation ((TR)-SSHG). In particular, this thesis focuses on experimental development of the TR-SSHG technique in our group, applied to the characterization of ultrafast photoinduced processes at liquid/liquid interfaces. The original work included the results on the excited-state dynamics and spectroscopic signatures of interfacial molecular probes, characterization of environmental properties in interfacial systems and potentials of investigating photoinduced electron transfer at liquid/liquid interfaces.

It was shown that TR-SSHG is a powerful tool for investigating the photophysics of organic dyes at liquid interfaces. For instance, it was found that the ultrafast excited-state dynamics of malachite green (MG) involved the rotation of not only aniline groups but also the phenyl ring. The MG excited-state dynamics was found to be affected by the presence of aggregates: the fast and slow components in the dynamics were assigned to the ground-state recovery of monomers and aggregates, respectively.

It was shown that the population of MG in particular and of charged dyes in general at the interface could be controlled by the addition of small amounts of ionic surfactants: the dye adsorption was enhanced when using oppositely charged surfactants, whereas depletion of dye occurred when adding a surfactant with the same charge, which was explained in terms of electrostatic interactions. However, independently of the relative charges of dye and surfactant, a large interfacial coverage by the surfactant

was found to decrease the dye population, due to the smaller affinity of the latter for the interface.

It was found that the number of MG aggregates is a powerful probe of the interfacial affinity of salt anions. The effect on the formation of aggregates caused by various anions was compared and the studied anions were sequenced as $SO_4^- < Cl^- < Br^- < SCN^-$, which means that SCN^- has the highest affinity to the interface.

The study on the effect of salts demonstrated the use so-called “dynamic probe” approach, where the dynamic probe is a molecule whose photophysics depends on the properties of the environment, e.g. the excited-state dynamics of MG was dependent on the salt concentration. The same approach was used to study the phenomenon of hydrogen bonding at the interface. In this case, another organic dye, Eosin B (EB) was used as a dynamic probe. The bulk investigations showed that the excited state of EB undergoes ultrafast hydrogen-bond-assisted non-radiative deactivation due to the charge-transfer character of the excited state introduced by the presence of two nitro groups: the increase of electronic density on these groups upon excitation is accompanied by a strengthening of hydrogen bonds in protic solvents. However, at the interface, the ultrafast deactivation of EB, was found to remarkably slow down, which pointed to the existence of a large population of EB molecules at the interface, which are not hydrogen-bonded to water or, at least, do not undergo hydrogen-bond-assisted non-radiative deactivation. Such effect might be explained by a specific orientation of EB molecules at the interface, which prevents contact between the hydrogen-bond-accepting nitro groups and water, or from the mechanism of the hydrogen-bond-assisted deactivation itself that is no longer operative at the interface.

The photophysics of one more organic dye, rhodamine 6G (R6G), was studied both in bulk water and at the aqueous interface. Its excited-state dynamics was found to consist of the contributions from the monomers and aggregates. The decrease of R6G monomer lifetime upon increasing its concentration was ascribed to self-quenching through Förster-type energy transfer from monomers to aggregates. At the interface, by probing different second-order nonlinear susceptibility tensor elements, a contribution of different species into the excited-state dynamics of R6G could be distinguished.

Finally, a few preliminary results showed the potential of TR-SSHG for investigating

the photoinduced ET at and through liquid interfaces. As the investigations of the dynamics of truly photochemical reactions at the liquid interface still remain extremely scarce, more of an experimental effort remains to be done to make a breakthrough in this tempting direction.

All these examples demonstrated that liquid/liquid interfaces represent a challenging and exciting playground for both spectroscopists and photochemists. At the moment, our knowledge concerning the dynamics of photoinduced processes at these interfaces is still poor, and efforts in several directions are required. For example, the current choice of molecules for sensing specific properties of liquid interfaces is not sufficient, and clearly more interfacial probes are needed. Although very powerful, TR-SSHG spectroscopy in its present state suffers from several limitations. Some of them, such as the uncertainty concerning the thickness of the interfacial region that contributes to the signal, cannot be readily eliminated. However, there is much room for improvement. For example, our effort to perform TR-SSHG at different wavelengths greatly facilitated the interpretation and allowed more complicated processes to be investigated. Broadband probing and detection as recently demonstrated for electronic TR-SSFG at the air/water interface should also be considered.[48]

In all of the above-presented results, homodyne detection of the SSHG signal was performed, the signal intensity being proportional to $\left|\chi^{(2)}\right|^2$. The response from molecules probed resonantly has both real and imaginary parts, whereas the response from the solvents, which is nonresonant, is only real. If this nonresonant response is negligibly small, the change of signal intensity in a time-resolved experiment is directly proportional to the square of the population change. This is, however, no longer the case if the nonresonant contribution differs from zero as it interferes with the real part of the resonant response and distorts the time profile of the signal intensity. One solution to this is heterodyne detection, where the SSHG signal is mixed with an optical field of the same frequency and in-phase with the field generated from the imaginary part of the susceptibility. The advantages are an amplification of the resonant signal and a linear relationship between signal intensity and population changes. This detection has already been demonstrated for stationary vibrational and electronic SSFG but not for TR-SSFG.[45, 86]

A further development of these techniques could be 2D-SSHG, analogous to the setup

recently reported for vibrational SSFG.[209] This would be an extremely powerful method for investigating solvation dynamics and the interaction between probe molecules at interfaces.

In addition to these spectroscopic developments, further effort should also be made on the theoretical side. Until now, the data interpretation has been mostly performed on a qualitative basis in the limit of a two-level system. At the moment, our understanding of the exact relationship between a transient absorption spectrum measured in a bulk experiment and the expected TR-SSHG spectra is very limited. Such knowledge is needed to avoid misinterpretation. The recent theoretical treatment of orientational diffusion at the interface performed by Fayer and co-workers clearly demonstrates the pitfall of too simplistic a data analysis.[210]

Molecular dynamics simulations represent also a powerful additional tool to improve our understanding of liquid interfaces and to help the interpretation of experimental data. Some effort, which gave new insight into the structure and dynamics of interfaces, has already been done.[11, 44, 211, 212] However, less information is available so far about the dynamic properties of solute molecules adsorbed at a liquid interface.

Theoretical development requires reliable experimental data, and clearly important concerted efforts in all of these directions are still required before our knowledge on the dynamics of photoinduced processes at liquid interfaces can reach a level similar to the one that can nowadays be attained in bulk solution.

6. APPENDICES

6.1. Supporting information for Section 4.1.1

Samples. MG oxalate was purchased from *Fluka* and BG was obtained from *Waldeck*, Division Chroma. For the preparation of the water+glycerol mixtures, deionized water, and an 86-88 wt % aqueous solution of glycerol (p.a.) from *Acros Organics* were used. The dynamic viscosity of the mixtures was calculated according to the empirical formula given by Shankar and Kumar. The concentration of the dye in the water+glycerol solutions in both transient absorption and SSHG experiments was equal to 10^{-5} M and $2 \cdot 10^{-5}$ M for MG and BG, respectively. At these concentrations no aggregates should be formed in bulk solution, which was confirmed by monitoring the stationary absorption spectra of the samples. The absorption spectra of the solutions corresponded to the spectra of the monocationic forms of the dyes, independently of the composition of the water+glycerol mixtures. No decomposition of the samples in time has been observed. The following liquids were used as the upper layer for SSHG samples: *n*-hexane (Fluka, p. a.), *n*-heptane (*Acros Organics*, 99%+), octane (*Aldrich*, 98%), decane (*Fluka*, purum), dodecane (*Acros Organics*, 99%), tetradecane (*Acros Organics*, 99%), pentadecane (*Aldrich*, 98%), and paraffin oil (*Fluka*, for IR spectroscopy). All compounds were used as supplied.

6.2. Supporting information for Section 4.1.2

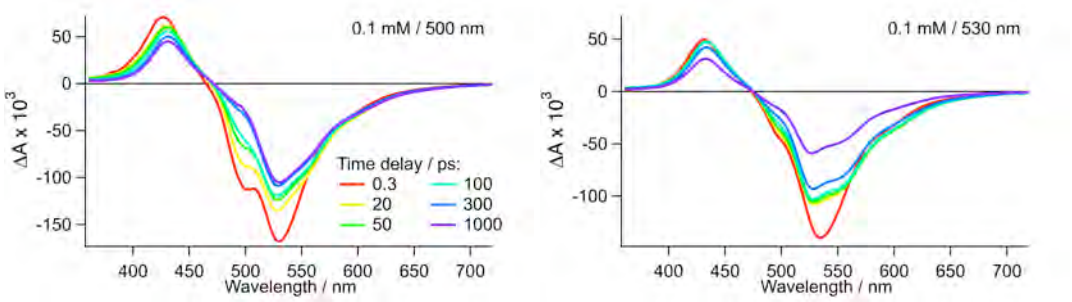

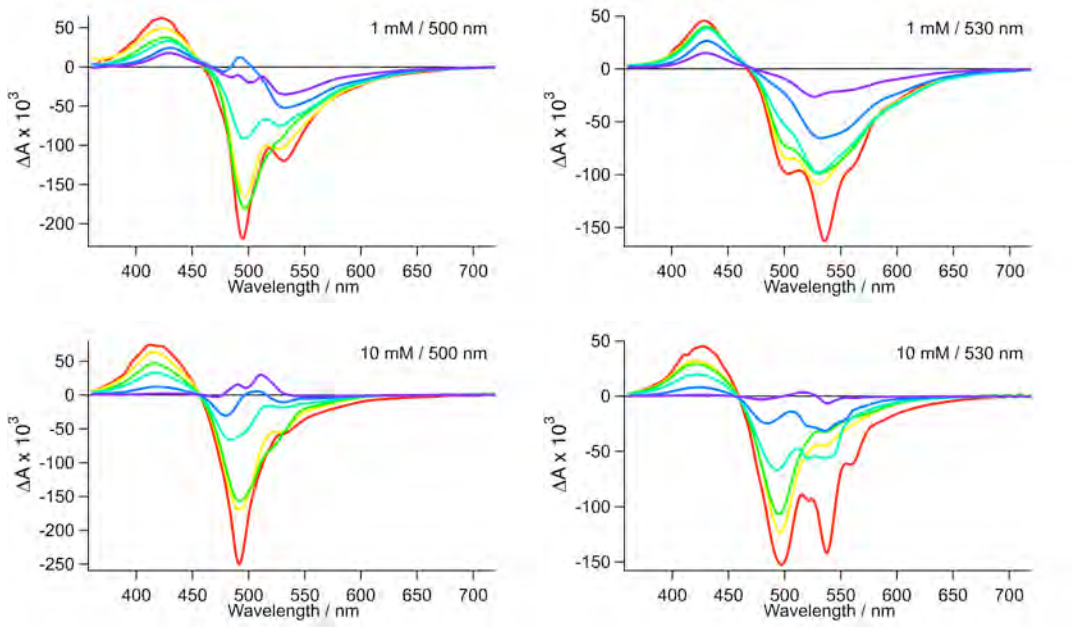

Figure 6.1. Original TA spectra of R6G in bulk water recorded upon excitation at 530 nm and 500 nm, at concentrations 0.1 mM, 1 mM and 10 mM. For better visualization, each data set shows 6 spectra at different time delays. The spectra are color-coded according to their time delay, from red (300 fs) to purple (1.0 ns).

Samples. The aqueous solutions of R6G chloride (*Acros Organics*, 99%) were prepared at bulk concentrations 0.1 mM, 1 mM and 10 mM for both TA and TR-SSHG experiments by dissolving the dye in deionized water. In all TRSSHG experiments, the upper organic phase was dodecane (*Acros Organics*, 99%). All compounds were used without further purification. The pH of the samples was between 4 and 8 depending on the concentration. The steady-state absorption and fluorescence spectra and the fluorescence lifetime of R6G were found to be insensitive to the change of pH in this range. Also, the pH was ensured to remain unchanged before and after the measurements.

Cells. For the TR-SSHG experiments, the interface between dodecane and R6G aqueous solution was prepared into a 4x4x4 cm3 optical glass cell. For the stationary and transient absorption experiments, quartz cells with a thickness of 1 mm, 10 μm and 1 μm were respectively used for the R6G concentrations 0.1 mM, 1 mM and 10 mM. For stationary fluorescence experiments the samples were held in a 10 mm quartz cell.

6.3. Supporting information for Section 4.2.1

Samples. Eosin B (EB, disodium salt, *Sigma-Aldrich*) and eosin Y (EY, disodium salt, *Acros Organics*) were used without further purification. The organic solvents: methanol (MeOH, *Acros Organics*, p.a.), 1-butanol (BuOH, *Merck*, p.a.), 1-decanol (DeOH, *Acros Organics*, 99%), and acetonitrile (ACN, *ROTH*, *ROTIDRY*, > 99.9%, <10 ppm H_2O) were used as supplied. Deionized water was used for the aqueous solutions. Their pH was kept around 9-10 by addition of NaOH.

Quantum Chemical Calculations. Ground-state gas-phase geometry optimization was performed at the density functional level of theory (DFT) using the B3LYP functional,[213] and a [3s2p1d] basis set.[214] Electronic vertical excitation energies were computed with time-dependent density functional theory (TD-DFT) using the same functional and basis set.[215] The calculations were carried out using Turbomole version 6.0.[216]

6.4. Supporting information for Section 4.2.2

Samples. Malachite green (MG) oxalate, NaCl, and NaSCN have been purchased from *Fluka*, whereas Na_2SO_4 and NaBr were from *Merck*. All compounds have been used without further purification. MG has been dissolved in deionized water to a concentration specified further for each measurement. The following liquids have been used as the upper layer for SSHG samples: *n*-heptane (*Acros Organics*, 99%+), octane (*Aldrich*, 98%), decane (*Fluka*, purum), dodecane (*Acros Organics*, 99%), tetradecane (*Acros Organics*, 99%), and pentadecane (*Aldrich*, 98%). All compounds have been used as supplied. The pH of all samples has been observed between 2.8 and 3, which ensures MG to be present in monocationic form in the investigated solutions. No significant degradation of the samples has been observed after the measurements. The preparation of the samples as well as all the measurements have been done at room temperature.

6.5. Supporting information for Section 4.2.3

Samples. Malachite green (MG) oxalate and eosin B (EB) disodium were purchased from *Fluka* and *Sigma-Aldrich*, respectively. The salts, sodium thiocyanate (NaSCN) and guanidinium chloride (GuHCl), were from *Fluka* and *AppliChem*, respectively, whereas the surfactants, sodium dodecyl sulfate (SDS) and cetyltrimethylammonium bromide (CTAB), were from *AppliChem* and *Acros Organics*, respectively. The aqueous solutions were prepared by dissolving the dyes and salts or surfactants at concentrations specified further for each experiment in deionized water and were poured into a 4x4x4 cm3 optical glass cell. In all measurements, the pH of the aqueous solutions remained between 5 and 7, a range where MG and EB are in the monocationic and dianionic form, respectively. In all experiments, the upper organic phase was dodecane (*Acros Organics*, 99%). All compounds were used without further purification.

7. RÉSUMÉ DE LA THÈSE EN FRANÇAIS

Les surfaces aqueuses et interfaces sont omniprésentes et jouent un rôle important dans de nombreux processus naturels et technologiques. La région anisotropique et hétérogène que constitue l'interface a typiquement une épaisseur du diamètre de quelques molécules seulement. Bien que de nombreuses techniques permettant de caractériser les surfaces solides avec une résolution atomique existent, la situation est différente en ce qui concerne les interfaces aqueuses liquides. La connaissance de ces interfaces était rudimentaire jusqu'à tout récemment, principalement à cause du désordre et des ondes capillaires de la surface ainsi que de la volatilité de l'eau sous forme liquide. Ceci a cependant changé au cours de la dernière décennie grâce aux techniques spectroscopiques modernes. Le but de cette thèse était d'approfondir les connaissances de la photophysique et de la photochimie des interfaces aqueuses.

L'accent a été mis sur les résultats obtenus grâce à une technique spectroscopique de pointe destinée à l'étude des interfaces liquides – la génération de seconde harmonique à la surface (en temps résolu) (GSHS-(TR)). En particulier, cette thèse met en avant les récents développements expérimentaux de la GSHS-TR dans notre groupe, appliquée à la caractérisation de processus photoinduits ultrarapides aux interfaces liquide/liquide. La tâche initiale consistait en l'étude de la dynamique de l'état excité et de la signature spectroscopique de sondes interfaciales, la caractérisation des propriétés environnementales de systèmes interfaciaux et la potentialité de l'étude du transfert d'électron photoinduit aux interfaces liquide/liquide. Il a été démontré que la GSHS-TR est un puissant outil pour étudier la photophysique de colorants organiques aux interfaces liquides. Par exemple, il a été découvert que la dynamique ultra rapide de l'état excité du vert de malachite (VM) implique non seulement la rotation des groupements aniline, mais également du phényl. La dynamique de l'état excité du VM s'est avérée être affectée par la présence d'agrégats: les composantes rapides et lentes de la dynamique ont respectivement été attribuées au retour à l'état fondamental des monomères et des agrégats. Il a été démontré que la population de VM à l'interface, et plus généralement de colorants chargés, pouvait être contrôlée par l'addition de petites quantités de surfactants ioniques: l'adsorption de molécules de colorant à l'interface augmente en présence d'un surfactant de charge opposée, alors qu'elle diminue avec un surfactant de charge similaire, ce qui a été expliqué en termes d'interactions électrostatiques. Toutefois, indépendamment de la

charge relative du colorant et du surfactant, une importante couverture interfaciale par le surfactant mène à une diminution de la population de colorant du fait de la moindre affinité de ce dernier pour l'interface.

Il a été établi que la quantité d'agrégats de VM est un puissant outil pour mesurer l'affinité des anions de divers sels pour l'interface. La comparaison de l'effet qu'ont différents anions sur la formation d'agrégats a permis de les classer selon leur affinité pour l'interface: $SO_4^- < Cl^- < Br^- < SCN^-$; SCN^- ayant la plus grande affinité pour l'interface.

L'étude sur l'effet des sels a montré l'utilisation de l'approche dite de "sonde dynamique", où la sonde dynamique est une molécule dont la photophysique dépend des propriétés de l'environnement, par exemple la dynamique de l'état excité du VM dépend de la concentration de sel. Cette même approche a été utilisée afin d'étudier le phénomène de liaison hydrogène à l'interface. Dans le cas présent, un autre colorant organique, l'éosine B (EB), a été utilisé comme sonde dynamique. L'investigation de la phase condensée (bulk) a révélé que, grâce à l'assistance de liaisons hydrogène, l'état excité de l'EB est désactivé ultra rapidement de manière non radiative à cause du caractère transfert de charge de l'état excité qui est dû à la présence de deux groupements nitro: l'accroissement de la densité électronique localisée sur ces groupes après excitation est accompagnée par un renforcement des liaisons hydrogène dans les solvants protiques. Néanmoins, à l'interface, la désactivation de l'EB est remarquablement ralentie, ce qui indique la présence d'une importante population de molécules d'EB ne possédant pas de liaisons hydrogène avec l'eau ou, du moins, ne subissant pas de désactivation non radiative assistée par liaisons hydrogène. Un tel effet pourrait s'expliquer par une orientation spécifique des molécules d'EB à l'interface qui empêcherait le contact entre les groupes nitro, accepteurs de liaisons hydrogène, et l'eau, ou par le mécanisme de désactivation assisté par liaisons hydrogène lui-même qui ne serait plus efficient à l'interface.

La photophysique d'un dernier colorant, la rhodamine 6G (R6G), a été étudiée en phase condensée (bulk) ainsi qu'à l'interface aqueuse. Deux contributions associées aux monomères et aux agrégats participent à la dynamique de l'état excité. Le déclin de la durée de vie du monomère lors de l'augmentation de la concentration de R6G a été attribué à l'auto-extinction par transfert d'énergie de type Förster des monomères aux agrégats. A l'interface, des mesures effectuées en résonance avec différents

éléments du tenseur de susceptibilité non linéaire du second ordre ont permis de révéler les contributions des différentes espèces à la dynamique de l'état excité de la R6G.

Finalement, quelques résultats préliminaires illustrent le potentiel de la GSHS-TR pour l'étude du transfert d'électron photoinduit à travers et aux interfaces liquides. Etant donné que les études concernant la dynamique de réelles réactions photochimiques aux interfaces liquides sont encore extrêmement rares, un conséquent effort expérimental reste à accomplir afin de réaliser un progrès dans cette attirante direction.

8. PUBLICATIONS

1. **M. Fedoseeva**, P. Fita, A. Punzi, E. Vauthey, *Salt Effect on the Formation of Dye Aggregates at Liquid/Liquid Interfaces Studied by Time Resolved Surface Second Harmonic Generation,* J. Phys. Chem. C. 114, 13774-13781, 2010
2. P. Fita, **M. Fedoseeva**, E. Vauthey, *Ultrafast Excited-State Dynamics of Eosin B: A Potential Probe of the Hydrogen-Bonding Properties of the Environment*, Journal of Physical Chemistry A, 115 (12), 2465-2470, 2011
3. P. Fita, **M. Fedoseeva**, E. Vauthey, *Hydrogen-Bond-Assisted Excited-State Deactivation at Liquid/Water Interfaces,* Langmuir, 27, 4645-4652, 2011
4. **M. Fedoseeva**, J. Grilj, O. Kel, M. Koch, R. Letrun, V. Markovic, I. Petkova, S. Richert, A. Rosspeintner, P. Sherin, D. Villamaina, B. Lang and E. Vauthey, *Photoinduced electron transfer reactions: from the elucidation of old problems towards the exploration of interfaces*, Chimia, 65, 350-352, 2011
5. S. Richert, **M. Fedoseeva** and E. Vauthey, *Ultrafast Photoinduced Dynamics at Air/Liquid and Liquid/Liquid Interfaces*, Journal of Physical Chemistry Letters, 3 (12), p1635-1642, 2012
6. **M. Fedoseeva**, S. Richert and E. Vauthey, *Excited-State Dynamics of Organic Dyes at Liquid/Liquid Interfaces*, Langmuir, 28, 11291-11301, 2012
7. **M. Fedoseeva**, P. Fita, and E. Vauthey, *Excited-state dynamics of charged dyes at alkane/water interfaces in the presence of salts and ionic surfactants,* Langmuir, submitted, 2013
8. **M. Fedoseeva**, R. Letrun, and E. Vauthey, *Excited-state dynamics of rhodamine 6G in bulk water and at alkane/water interfaces,* J. Phys. Chem. B, in preparation, 2013

9. BIBLIOGRAPHY

(1) Volkov, A.G., *Liquid interfaces in chemincal, biological, and pharmaceutical applications*. Marcel Dekker: New York, 2001.

(2) Watarai, H.; Teramae, N.; Sawada, T., *Interfacial Nanochemistry*. Kluwer Academics: New York, 2005.

(3) Adamson, A.W., *Physical chemistry of surfaces*. 4th ed.; Willey: New York, 1982.

(4) Fermin, D.J.; Duong, H.D.; Ding, Z.; Brevet, P.F.; Girault, H.H., *Electrochem. Comm.* **1999,** *1*, 29.

(5) Steel, W.H.; Walker, R.A., *Nature* **2003,** *424*, 296.

(6) Tamburello Luca, A.A.; Hebert, P.; Brevet, P.F.; Girault, H.H., *J. Chem. Soc. Faraday Trans.* **1995,** *91*, 1763.

(7) Walker, D.S.; Richmond, G.L., *J. Phys. Chem. C* **2007,** *112*, 201.

(8) Shang, X.; Nguyen, K.; Rao, Y.; Eisenthal, K.B., *J. Phys. Chem. C* **2008,** *112*, 20375.

(9) Nihonyanagi, S.; Ishiyama, T.; Lee, T.; Yamaguchi, S.; Bonn, M.; Morita, A.; Tahara, T., *J. Am. Chem. Soc.* **2011,** *133*, 16875.

(10) Jin, Q.; Bethke, C.M., *Biophys. J.* **2002,** *83*, 1797.

(11) Jungwirth, P.; Tobias, D., *Chem. Rev.* **2006,** *106*, 1259−1281

(12) Garrett, B.C., *Science* **2004,** *303*, 1146.

(13) Vieceli, J.; Ma, O.L.; Tobias, D.J., *J. Phys. Chem. A* **2004,** *108*, 5806.

(14) Vieceli, J.; Roeselová, M.; Potter, N.; Dang, L.X.; Garrett, B.C.; Tobias, D.J., *J. Phys. Chem. B* **2005,** *109*, 15876.

(15) De Serio, M.; Bader, A.N.; Heule, M.; Zenobi, R.; Deckert, V., *Chem. Phys. Lett.* **2003,** *380*, 47.

(16) De Serio, M.; Mohapatra, H.; Zenobi, R.; Deckert, V., *Chem. Phys. Lett.* **2006,** *417*, 452.

(17) Masuhara, H.; Mataga, N.; Tazuke, S.; Murao, T.; Yamazaki, I., *Chem. Phys. Lett.* **1983,** *100*, 415.

(18) Sassaman, J.L.; Wirth, M.J., *Colloids Surf. A* **1994,** *93*, 49.

(19) Ishizaka, S.; Habuchi, S.; Kim, H.-B.; Kitamura, N., *Anal. Chem.* **1999,** *71*, 3382.

(20) Pant, D.; Girault, H.H., *Phys. Chem. Chem. Phys.* **2005,** *7*, 3457.

(21) Yao, H.; Kitagawa, F.; Kitamura, N., *Langmuir* **2000,** *16*, 3454.

(22) Tsukahara, S.; Watarai, H., *Chem. Lett.* **1999,** *28*, 89.

(23) Brodard, P.; Vauthey, E., *Rev. Sci. Instrum.* **2003,** *74*, 725.

(24) Tamai, N.; Asahi, T.; Ito, T., Picosecond dynamics in thin films by transient grating spectroscopy. In *Microchemistry*, Masuhara, H.; Schryver, F.C.D.; Kitamura, N.; Eds. Elsevier: Amsterdam, 1994; pp 241.

(25) Terazima, M.; Kojima, Y.; Hirota, N., *Chem. Phys. Lett.* **1996,** *259*, 451.

(26) Fourkas, J.T.; Fayer, M.D., *Acc. Chem. Res.* **1992,** *25*, 227.

(27) Gumy, J.-C.; Vauthey, E., *J. Phys. Chem.* **1996,** *100*, 8628.

(28) Hogemann, C.; Pauchard, M.; Vauthey, E., *Rev. Sci. Instrum.* **1996,** *67*, 3449.

(29) Brodard, P.; Vauthey, E., *J. Phys. Chem. B* **2005,** *109*, 4668.

(30) Faubel, M. In *Photoelectron Spectroscopy at Liquid Surfaces*, Photoionization & Photodetachment, pp 634.

(31) Faubel, M.; Steiner, B.; Toennies, J.P., *J. Chem. Phys.* **1997,** *106*, 9013.

(32) Winter, B., *Nucl. Instrum. Methods Phys. Res., Sect. A* **2009,** *601*, 139.

(33) Winter, B.; Faubel, M., *Chem. Rev.* **2006,** *106*, 1176.

(34) Seidel, R.; Thürmer, S.; Winter, B., *J. Phys. Chem. Lett.* **2011,** *2*, 633.

(35) Abel, B., *Annu. Rev. Phys. Chem.* **2013,** *64*, 533.

(36) Boyd, R.W., *Nonlinear Optics*. 3rd ed.; Academic Press: Orlando, 2008.

(37) Heinz, T.F.; Chen, C.K.; Ricard, D.; Shen, Y.R., *Phys. Rev. Lett.* **1982,** *48*, 478.

(38) Brevet, P.F., *Surface Second Harmonic Generation*. Presses polytechniques et universitaires romandes: Lausanne, 1997.

(39) Vauthey, E., *Lectures of Virtual European University on Lasers* **2006**.

(40) Yamaguchi, S.; Tahara, T., *J. Phys. Chem. B* **2004,** *108*, 19079.

(41) Richmond, G.L., *Chem. Rev.* **2002,** *102*, 2693−2724

(42) Echevarria, L.; Nieto, P.; Gutiérrez, H.; Mújica, V.; Caetano, M., *J. Phys. Chem. B* **2003,** *107*, 9332.

(43) Scatena, L.F.; Brown, M.G.; Richmond, G.L., *Science* **2001,** *292*, 908.

(44) Moore, F.G.; Richmond, G.L., *Acc. Chem. Res.* **2008,** *41*, 739.

(45) Chen, X.; Hua, W.; Huang, Z.; Allen, H.C., *J. Am. Chem. Soc.* **2010,** *132*, 11336.

(46) Nihonyanagi, S.; Yamaguchi, S.; Tahara, T., *J. Am. Chem. Soc.* **2010,** *132*, 6867.

(47) Eftekhari-Bafrooei, A.; Borguet, E., *J. Am. Chem. Soc.* **2010,** *132*, 3756.

(48) Sekiguchi, K.; Yamaguchi, S.; Tahara, T., *J. Chem. Phys.* **2008,** *128*, 114715.

(49) Shank, C.V.; Yen, R.; Hirlimann, C., *Phys. Rev. Lett.* **1983,** *51*, 900.

(50) Shannon, V.L.; Koos, D.A.; Robinson, J.M.; Richmond, G.L., *Chem. Phys. Lett.* **1987,** *142*, 323.

(51) Sitzmann, E.V.; Eisenthal, K.B., *J. Phys. Chem.* **1988,** *92*, 4579.

(52) Franken, P.A.; Hill, A.E.; Peters, C.W.; Weinreich, G., *Phys. Rev. Lett.* **1961,** *7*, 118.

(53) Terhune, R.W.; Maker, P.D.; Savage, C.M., *Phys. Rev. Lett.* **1962,** *8*, 404.

(54) Brown, F.; Parks, R.E.; Sleeper, A.M., *Phys. Rev. Lett.* **1965,** *14*, 1029.

(55) Wang, C.C., *Phys. Rev.* **1969,** *178*, 1457.

(56) Bloembergen, N.; Pershan, P.S., *Phys. Rev.* **1962,** *128*, 606.

(57) Bloembergen, N.; Chang, R.K.; Jha, S.S.; Lee, C.H., *Phys. Rev.* **1968,** *174*, 813.

(58) Brown, F.; Matsuoka, M., *Phys. Rev.* **1969,** *185*, 985.

(59) Rudnick, J.; Stern, E.A., *Phys. Rev. B* **1971,** *4*, 4274.

(60) Shen, Y.R.; de Martini, F., In *Surf. Pol.*, Agronovich, V.M.; Mills, D.L., Eds. North-Holland: 1982; p 629.

(61) Heinz, T.F. Nonlinear Optics of Surfaces and Interfaces. University of California, Berkley, 1982.

(62) Sipe, J.E.; Stegman, G.I., In *Surf. Pol.*, Agronovich, V.M.; Mills, D.L., Eds. North-Holland: 1982; p 661.

(63) Fukui, M.; Stegman, G.I., In *Electromagnetic Surface Modes*, Boardman, A.D., Ed. John Willey & Sons: 1982; p 725.

(64) Shen, Y.R., *Surf. Sci.* **1994,** *299–300*, 551.

(65) Heinz, T.F.; Reider, G.A., *Tr. Anal. Chem.* **1989,** *8*, 235.

(66) Reider, G.A.; Heinz, T.F., In *Second-Order Nonlinear Optical Effects at Surfaces and Interfaces: Recent Advances*, Halevi, P., Ed. Elsevier: 1995; pp 413.

(67) Corn, R.M., *Anal. Chem.* **1991,** *63*, 285A.

(68) Corn, R.M.; Higgins, D.A., *Chem. Rev.* **1994,** *94*, 107.

(69) Richmond, G.L.; Robinson, J.M.; Shannon, V.L., *Prog. Surf. Sci.* **1988,** *28*, 1.

(70) Akhmanov, S.; Emel'yanov, V.I.i.; Koroteev, N.I.; Seminogov, V., *Phys. Usp.* **1985,** *28*, 1084.

(71) Huang, J.Y.; Shen, Y.R., In *Laser Spectroscopy and Photochemistry on Metal Surfaces, Part 1*, Dai, H.L.; Ho, W., Eds. World Scientific: 1995; pp 5.

(72) Eisenthal, K.B., *Annu. Rev. Phys. Chem.* **1992,** *43*, 627.

(73) Brevet, P.F.; Girault, H.H., In *Liquid-Liquid Interfaces: Theory and Methods*, Volkov, A.G.; Deamer, D.W., Eds. CRC Press: 1996; pp 103.

(74) Eisenthal, K.B., *J. Phys. Chem.* **1996,** *100*, 12997.

(75) Eisenthal, K.B., *Chem. Rev.* **1996,** *96*, 1343.

(76) Fedoseeva, M.; Richert, S.; Vauthey, E., *Langmuir* **2012,** *28*, 11291.

(77) Heinz, T.F.; DiVincenzo, D.P., *Phys. Rev. A* **1990,** *42*, 6249.

(78) Eisenthal, K.B., *Chem. Rev.* **2006,** *106*, 1462.

(79) Guyot-Sionnest, P.; Chen, W.; Shen, Y.R., *Phys. Rev. B* **1986,** *33*, 8254.

(80) Sipe, J.E.; Moss, D.J.; van Driel, H.M., *Phys. Rev. B* **1987,** *35*, 1129.

(81) Hecht, E., *Optics*. Addison-Wesley: 1987.

(82) Mazely, T.L.; Hetherington Iii, W.M., *J. Chem. Phys.* **1987,** *86*, 3640.

(83) Shen, Y.-R., *New York, Wiley-Interscience, 1984, 575 p.* **1984,** *1*.

(84) Hicks, J.M.; Kemnitz, K.; Eisenthal, K.B.; Heinz, T.F., *J. Phys. Chem.* **1986,** *90*, 560.

(85) Kemnitz, K.; Bhattacharyya, K.; Hicks, J.M.; Pinto, G.R.; Eisenthal, K.B., *Chem. Phys. Lett.* **1986,** *131*, 285.

(86) Yamaguchi, S.; Tahara, T., *J. Chem. Phys.* **2008,** *129*, 101102.

(87) Zimdars, D.; Dadap, J.I.; Eisenthal, K.B.; Heinz, T.F., *J. Phys. Chem. B* **1999,** *103*, 3425.

(88) Benderskii, A.V.; Henzie, J.; Basu, S.; Shang, X.; Eisenthal, K.B., *J. Phys. Chem. B* **2004,** *108*, 14017.

(89) Zimdars, D.; Eisenthal, K.B., *J. Phys. Chem. A* **1999,** *103*, 10567.

(90) Fitts, J.P.; Machesky, M.L.; Wesolowski, D.J.; Shang, X.; Kubicki, J.D.; Flynn, G.W.; Heinz, T.F.; Eisenthal, K.B., *Chem. Phys. Lett.* **2005,** *411*, 399.

(91) Petersen, P.B.; Saykally, R.J., *Chem. Phys. Lett.* **2004,** *397*, 51.

(92) Petersen, P.B.; Saykally, R.J., *Annu. Rev. Phys. Chem.* **2006,** *57*, 333.

(93) Petersen, P.B.; Saykally, R.J.; Mucha, M.; Jungwirth, P., *J. Phys. Chem. B* **2005,** *109*, 10915.

(94) Liu, Y.; Dadap, J.I.; Zimdars, D.; Eisenthal, K.B., *J. Phys. Chem. B* **1999,** *103*, 2480.

(95) McArthur, E.A.; Eisenthal, K.B., *J. Am. Chem. Soc.* **2006,** *128*, 1068.

(96) Sitzmann, E.V.; Eisenthal, K.B., *J. Chem. Phys.* **1989,** *90*, 2831.

(97) Richert, S.; Fedoseeva, M.; Vauthey, E., *J. Phys. Rev. Lett.* **2012,** *3*, 1635.

(98) Kubin, R.F.; Fletcher, A.N., *J. Lumin.* **1982,** *27*, 455.

(99) van Stokkum, I.H.M.; Larsen, D.S.; van Grondelle, R., *Biochim. Biophys. Acta* **2004,** *1657*, 82.

(100) Riedle, E.; Beutter, M.; Lochbrunner, S.; Piel, J.; Schenkl, S.; Spörlein, S.; Zinth, W., *App. Phys. B* **2000,** *71*, 457.

(101) Akturk, S.; Gu, X.; Kimmel, M.; Trebino, R., *Opt. Express* **2006,** *14*, 10101.

(102) Yanshole, V.; Sherin, P.; Gritsan, N.P.; Snytnikova, O.A.; Mamatyuk, V.I.; Grilj, J.; Vauthey, E.; Sagdeev, R.Z.; Tsentalovich, Y.P., *Phys. Chem. Chem. Phys.* **2010,** *12*, 9502.

(103) Kovalenko, S.A.; Dobryakov, A.L.; Ernsting, N.P., *Rev. Sci. Instrum.* **2011,** *82*, 063102.

(104) Dobryakov, A.L.; Pérez Lustres, J.L.; Kovalenko, S.A.; Ernsting, N.P., *Chem. Phys.* **2008,** *347*, 127.

(105) Satzger, H.; Zinth, W., *Chem. Phys.* **2003,** *295*, 287.

(106) Morandeira, A.; Engeli, L.; Vauthey, E., *J. Phys. Chem. A* **2002,** *106*, 4833.

(107) Muller, P.A.; Hogemann, C.; Allonas, X.; Jacques, P.; Vauthey, E., *Chem. Phys. Lett.* **2000,** *326*, 321.

(108) Antoine, R.; Tamburello-Luca, A.A.; Hebert, P.; Brevet, P.F.; Girault, H.H., *Chem. Phys. Lett.* **1998,** *288*, 138

(109) Meech, S.R.; Yoshihara, K., *J. Phys. Chem.* **1990,** *94*, 4913.

(110) Shi, X.; Borguet, E.; Tarnovsky, A.N.; Eisenthal, K.B., *Chem. Phys.* **1996,** *205*, 167.

(111) Fedoseeva, M.; Fita, P.; Vauthey, E., *Langmuir* **2013**, *submitted*

(112) Sen, P.; Yamaguchi, S.; Tahara, T., *Faraday Discuss.* **2010,** *145*, 411.

(113) Ippen, E.P.; Shank, C.V.; Bergman, A., *Chem. Phys. Lett.* **1976,** *38*, 611.

(114) Nagasawa, Y.; Ando, Y.; Kataoka, D.; Matsuda, H.; Miyasaka, H.; Okada, T., *J. Phys. Chem. A* **2002,** *106*, 2024.

(115) Fita, P.; Punzi, A.; Vauthey, E., *J. Phys. Chem. C* **2009,** *113*, 20705.

(116) Punzi, A.; Martin-Gassin, G.l.; Grilj, J.; Vauthey, E., *J. Phys. Chem. C* **2009,** *113*, 11822.

(117) Beierlein, F.R.; Krause, A.M.; Jäger, C.M.; Fita, P.; Vauthey, E.; Clark, T., *Langmuir* **2013,** *29*, 11898.

(118) Fedoseeva, M.; Fita, P.; Punzi, A.; Vauthey, E., *J. Phys. Chem. C* **2010,** *114*, 13774.

(119) Moreno-Villoslada, I.; Fuenzalida, J.P.; Tripailaf, G.; Araya-Hermosilla, R.; del C. Pizarro, G.; Marambio, O.G.; Nishide, H., *J. Phys. Chem. B* **2010,** *114*, 11983.

(120) Penzkofer, A.; Leupacher, W., *J. Lumin.* **1987,** *37*, 61.

(121) Penzkofer, A.; Lu, Y., *Chem. Phys.* **1986,** *103*, 399.

(122) Arbeloa, F.L.; Ojeda, P.R.; Arbeloa, I.L., *J. Chem. Soc., Faraday Trans.* **1988,** *84*, 1903.

(123) Chen, Z.; Tang, Y.-J.; Xie, T.-T.; Chen, Y.; Li, Y.-Q., *J. Fluoresc.* **2008,** *18*, 93.

(124) Castro, A.; Sitzmann, E.V.; Zhang, D.; Eisenthal, K.B., *J. Phys. Chem.* **1991,** *95*, 6752.

(125) Berndt, K.; Dürr, H.; Palme, D., *Opt. Comm.* **1982,** *42*, 419.

(126) Makarov, N.S.; Drobizhev, M.; Rebane, A., *Opt. Express* **2008,** *16*, 4029.

(127) Fita, P.; Luzina, E.; Dziembowska, T.; Radzewicz, C.; Grabowska, A., *J. Chem. Phys.* **2006,** *125*, 184508.

(128) Smirl, A.L.; Clark, J.B.; Van Stryland, E.W.; Russell, B.R., *J. Chem. Phys.* **1982,** *77*, 631.

(129) Pigliucci, A.; Duvanel, G.; Daku, L.M.L.; Vauthey, E., *J. Phys. Chem. A* **2007,** *111*, 6135.

(130) Tamburello-Luca, A.A.; Hébert, P.; Antoine, R.; Brevet, P.F.; Girault, H.H., *Langmuir* **1997,** *13*, 4428.

(131) Reindl, S.; Penzkofer, A., *Chem. Phys.* **1996,** *213*, 429.

(132) Berlman, I.B., *Handbook of fluorescence spectra of aromatic molecules*. Academic Press: 1965.

(133) Math, N.N.; Naik, L.R.; Suresh, H.M.; Inamdar, S.R., *J. Lumin.* **2006,** *121*, 475.

(134) Nijegorodov, N.; Mabbs, R., *Spectrochim. Acta A* **2001,** *57*, 1449.

(135) Balzani, V.; Ceroni, P.; Gestermann, S.; Gorka, M.; Kauffmann, C.; Maestri, M.; Vögtle, F., *Chem. Phys. Chem* **2000,** *1*, 224.

(136) Flom, S.R.; Barbara, P.F., *J. Phys. Chem.* **1985,** *89*, 4489.

(137) Wyatt, W.A.; Bright, F.V.; Hieftje, G.M., *Anal. Chem.* **1987,** *59*, 2272.

(138) Fita, P.; Fedoseeva, M.; Vauthey, E., *J. Phys. Chem. A* **2011,** *115*, 2465.

(139) Levillain, P.; Fompeydie, D., *Anal. Chem.* **1985,** *57*, 2561.

(140) Mohammed, O.F.; Vauthey, E., *J. Phys. Chem. A* **2008,** *112*, 3823.

(141) Ungnade, H.E.; Roberts, E.M.; Kissinger, L.W., *J. Phys. Chem.* **1964,** *68*, 3225.

(142) Urbański, T., *Tetrahedron* **1959,** *6*, 1.

(143) Horng, M.L.; Gardecki, J.A.; Papazyan, A.; Maroncelli, M., *J. Phys. Chem.* **1995,** *99*, 17311.

(144) Flom, S.R.; Fendler, J.H., *J. Phys. Chem.* **1988,** *92*, 5908.

(145) Taft, R.W.; Kamlet, M.J., *J. Am. Chem. Soc.* **1976,** *98*, 2886.

(146) Catalán, J.; Díaz, C., *Liebigs Annalen* **1997,** *1997*, 1941.

(147) Catalán, J.; Díaz, C., *Eur. J. Org. Chem.* **1999,** *1999*, 885.

(148) Banerji, N.; Fürstenberg, A.; Bhosale, S.; Sisson, A.L.; Sakai, N.; Matile, S.; Vauthey, E., *J. Phys. Chem. B* **2008,** *112*, 8912.

(149) Cser, A.; Nagy, K.; Biczók, L., *Chem. Phys. Lett.* **2002,** *360*, 473.

(150) Furstenberg, A.; Vauthey, E., *Photochem. Photobiol. Sci.* **2005,** *4*, 260.

(151) Inoue, H.; Hida, M.; Nakashima, N.; Yoshihara, K., *J. Phys. Chem.* **1982,** *86*, 3184.

(152) Nishiya, T.; Yamauchi, S.; Hirota, N.; Baba, M.; Hanazaki, I., *J. Phys. Chem.* **1986,** *90*, 5730.

(153) Petkova, I.; Dobrikov, G.; Banerji, N.; Duvanel, G.; Perez, R.; Dimitrov, V.; Nikolov, P.; Vauthey, E., *J. Phys. Chem. A* **2009,** *114*, 10.

(154) Yatsuhashi, T.; Inoue, H., *J. Phys. Chem. A* **1997,** *101*, 8166.

(155) Granzhan, V.A.; Semenenko, S.V.; Zaitsev, P.M., *J. Appl. Spectr.* **1968,** *9*, 929.

(156) Su, Y.S.; Hong, H.-K., *Spectrochim. Acta A* **1968,** *24*, 1461.

(157) Cramer, L.E.; Spears, K.G., *J. Am. Chem. Soc.* **1978,** *100*, 221.

(158) Klonis, N.; Clayton, A.H.A.; Voss, E.W.; Sawyer, W.H., *Photochem. Photobiol.* **1998,** *67*, 500.

(159) Fita, P.; Fedoseeva, M.; Vauthey, E., *Langmuir* **2011,** *27*, 4645.

(160) Antoine, R.; Bianchi, F.; Brevet, P.F.; Girault, H.H., *J. Chem. Soc., Faraday Trans.* **1997,** *93*, 3833.

(161) Brevet, P.F., *J. Chem. Soc., Faraday Trans.* **1996,** *92*, 4547.

(162) Valdes-Aguilera, O.; Neckers, D.C., *Acc. Chem. Res.* **1989,** *22*, 171.

(163) De, S.; Das, S.; Girigoswami, A., *Spectrochim. Acta A* **2005,** *61*, 1821.

(164) Silverstein, T.P., *J. Chem. Ed.* **1998,** *75*, 723.

(165) Chothia, C.; Janin, J., *Nature* **1975,** *256*, 705.

(166) Robinson, G.W.; Cho, C.H., *Biophys. J.* **1999,** *77*, 3311.

(167) Wiggins, P.M., *Phys. A* **1997,** *238*, 113.

(168) Scatena, L.F.; Richmond, G.L., *J. Phys. Chem. B* **2001,** *105*, 11240.

(169) McFearin, C.L.; Richmond, G.L., *J. Phys. Chem. C* **2009,** *113*, 21162.

(170) Siler, A.R.; Brindza, M.R.; Walker, R.A., *Anal. Bioanal. Chem.* **2009,** *395*, 1063.

(171) Sherin, P.S.; Grilj, J.; Kopylova, L.V.; Yanshole, V.V.; Tsentalovich, Y.P.; Vauthey, E., *J. Phys. Chem. B* **2010,** *114*, 11909.

(172) Vauthey, E., *Chem. Phys. Lett.* **1993,** *216*, 530.

(173) Adamson, A.W.; Gast, A.P., *Physical chemistry of surfaces*. Wiley: 1997.

(174) Durand-Vidal, S.; Simonin, J.P.; Turq, P., *Electrolytes at Interfaces*. Springer: 2001.

(175) Fawcett, D.W.R., *Liquids, Solutions, and Interfaces : From Classical Macroscopic Descriptions to Modern Microscopic Details*. Oxford University Press, USA: 2004.

(176) Ghosal, S.; Hemminger, J.C.; Bluhm, H.; Mun, B.S.; Hebenstreit, E.L.D.; Ketteler, G.; Ogletree, D.F.; Requejo, F.G.; Salmeron, M., *Science* **2005,** *307*, 563.

(177) Liu, D.; Ma, G.; Levering, L.M.; Allen, H.C., *J. Phys. Chem. B* **2004,** *108*, 2252.

(178) Rao, Y.; Subir, M.; McArthur, E.A.; Turro, N.J.; Eisenthal, K.B., *Chem. Phys. Lett.* **2009,** *477*, 241.

(179) Raymond, E.A.; Richmond, G.L., *J. Phys. Chem. B* **2004,** *108*, 5051.

(180) Weber, R.; Winter, B.; Schmidt, P.M.; Widdra, W.; Hertel, I.V.; Dittmar, M.; Faubel, M., *J. Phys. Chem. B* **2004,** *108*, 4729.

(181) Song, J.; Kim, M.W., *J. Phys. Chem. B* **2010,** *114*, 3236.

(182) Duxbury, D.F., *Chem. Rev.* **1993,** *93*, 381.

(183) Nagasawa, Y.; Ando, Y.; Okada, T., *Chem. Phys. Lett.* **1999,** *312*, 161.

(184) Viswanath, P.; Aroti, A.; Motschmann, H.; Leontidis, E., *J. Phys. Chem. B* **2009,** *113*, 14816.

(185) Viswanath, P.; Motschmann, H., *J. Phys. Chem. C* **2007,** *111*, 4484.

(186) Viswanath, P.; Motschmann, H., *J. Phys. Chem. C* **2008,** *112*, 2099.

(187) Zhang, Y.; Cremer, P.S., *Curr. Opin. Chem. Biol.* **2006,** *10*, 658.

(188) Onorato, R.M.; Otten, D.E.; Saykally, R.J., *Proc. Natl. Acad. Sci.* **2009,** *106*, 15176.

(189) Petersen, P.B.; Saykally, R.J., *J. Phys. Chem. B* **2006,** *110*, 14060.

(190) Barnes, A.R., *JSDC* **1996,** *112*, 49.

(191) Boström, M.; Williams, D.R.; Ninham, B.W., *Biophys. J.* **2003,** *85*, 686.

(192) Mason, P.E.; Neilson, G.W.; Dempsey, C.E.; Barnes, A.C.; Cruickshank, J.M., *Proc. Natl. Acad. Sci.* **2003,** *100*, 4557.

(193) Pegram, L.M.; Record, M.T.J., *J. Phys. Chem. B* **2007,** *111*, 5411.

(194) Smith, J.S.; Scholtz, J.M., *Biochem.* **1996,** *35*, 7292.

(195) Wernersson, E.; Heyda, J.; Vazdar, M.; Lund, M.; Mason, P.E.; Jungwirth, P., *J. Phys. Chem. B* **2011,** *115*, 12521.

(196) Beaman, D.K.; Robertson, E.J.; Richmond, G.L., *J. Phys. Chem. C* **2011,** *115*, 12508.

(197) Nguyen, K.T.; Shang, X.; Eisenthal, K.B., *J. Phys. Chem. B* **2006,** *110*, 19788.

(198) Gragson, D.E.; McCarty, B.M.; Richmond, G.L., *J. Phys. Chem.* **1996,** *100*, 14272.

(199) Zhao, X.; Ong, S.; Wang, H.; Eisenthal, K.B., *Chem. Phys. Lett.* **1993,** *214*, 203.

(200) Martin, M.M.; Plaza, P.; Meyer, Y.H., *J. Phys. Chem.* **1991,** *95*, 9310.

(201) Gragson, D.E.; McCarty, B.M.; Richmond, G.L., *J. Am. Chem. Soc.* **1997,** *119*, 6144.

(202) Benderskii, A.V.; Eisenthal, K.B., *J. Phys. Chem. A* **2001,** *106*, 7482.

(203) Edler, K.J.; Wasbrough, M.J.; Holdaway, J.A.; O'Driscoll, B.M., *Langmuir* **2009,** *25*, 4047.

(204) Tah, B.; Pal, P.; Mahato, M.; Talapatra, G.B., *J. Phys. Chem. B* **2011,** *115*, 8493.

(205) Chattopadhyay, A.; London, E., *Anal. Biochem.* **1984,** *139*, 408.

(206) Barbara, P.F.; Meyer, T.J.; Ratner, M.A., *J. Phys. Chem.* **1996,** *100*, 13148.

(207) Vauthey, E., *J. Photochem. Photobiol. A.* **2006,** *179*, 1.

(208) McArthur, E.A.; Eisenthal, K.B., *J. Am. Chem. Soc.* **2006,** *128*, 1068.

(209) Zhang, Z.; Piatkowski, L.; Bakker, H.J.; Bonn, M., *Nat. Chem.* **2011,** *3*, 888.

(210) Gengeliczki, Z.; Rosenfeld, D.E.; Fayer, M.D., *J. Chem. Phys.* **2010,** *132*, 244703.

(211) Benjamin, I., *Annu. Rev. Phys. Chem.* **1997,** *48*, 407.

(212) Brown, M.G.; Walker, D.S.; Raymond, E.A.; Richmond, G.L., *J. Phys. Chem. B* **2002,** *107*, 237.

(213) Perdew, J.P., *Phys. Rev. B* **1986,** *33*, 8822.

(214) Schafer, A.; Horn, H.; Ahlrichs, R., *J. Chem. Phys.* **1992,** *97*, 2571.

(215) Bauernschmitt, R.; Ahlrichs, R., *Chem. Phys. Lett.* **1996,** *256*, 454.

(216) Ahlrichs, R.; Bär, M.; Häser, M.; Horn, H.; Kölmel, C., *Chem. Phys. Lett.* **1989,** *162*, 165.